

Master's Thesis

P-correlations with other inorganic elements in ash fractions of sewage sludge co-cumbusted and co-gasified with biogenic residues

presented by

Clara Loibersbeck

submitted to

Vienna University of Technology, Institute of Chemical, Environmental & Bioscience Engineering,

Supervisors

Univ.Prof.i.R. Dipl.-Ing. Dr.techn.Hofbauer Hermann,

Dipl.- Ing. Dr.tech Matthias Kuba

Vienna, February 03, 2022

Declaration of academic honesty

I certify that the master thesis at hand is to the best of my knowledge and belief the result of my own investigations and is composed by myself unless stated otherwise in the text. All content derived from the work of others has been specifically acknowledged. Furthermore, I confirm that I have not submitted this master thesis either nationally or internationally in any form.

Acknowledgement

I would like to thank the following people for helping with this research project: My supervisor Matthias Kuba, who guided me so positively, for his willingness to impart his knowledge and for helping me to structure the thesis. My colleagues Juraj Priscak and Miriam Huber for their time and help with the procedures. I would particularly like to thank Thomas Hannl for conducting some of the analysis at Lulea University of Technology, Sweden and for providing me with all the necessary material for analysis.

Abstract

Because of regulations and suggestions by the European Parliament in the European strategy for critical raw materials 2021/2011 phosphorus recovery has gained importance in industrial applications. It was determined that there is no substitute material available to compensate the need of P. The European Union is to a high degree dependent on phosphorus which was already named in the second list of critical resources 2014. A better life cycle plan and recycling measurements are requested for the future. In order to counteract to the negative phosphorus balance in agriculture, technologies for P recovery and recycled P-material are investigated. Thermochemical treatment of sewage waste seems promising for receiving bio-available phosphorus with a low heavy metal content. The formation of different P-compounds depends on the operating conditions and the feed used. Co-combustion of sewage sludge with sunflower husk and wheat straw residues enhances the concentration of potassium and the P-K-correlations in general. K-phosphates seem promising regarding their bioavailability and usage as fertilizer. Especially in the bottom ash fraction positive K-P-correlations were detected for co-combustion. Under gasification conditions, in reducing atmosphere, the formation of feldspar seem to occur to a higher extent and the K/Ca ratio does not seem as promising as under combustion conditions. It is assumed that the blending of the fuel fractions and the conversion of Fe- and Ca-phosphates to K-phosphates progressed unsatisfactorily.

German Abstract

Im Bericht über eine europäische Strategie für kritische Rohstoffe 2021/2011 werden Richtlinien für die Wiederverwertung von Phosphor festgelegt. Phosphor, als eine essenzielle Ressource kann nicht durch andere Elemente substituiert werden und ist unentbehrlich für pflanzliches Wachstum. Die Europäische Union ist in hohem Maße von diesem Stoff abhängig, weswegen sich Phosphor bereits 2014 in der zweiten Liste der kritischen Rohstoffe wiederfand. Als Alternative zur Gewinnung von Phosphorit wird die Rückgewinnung von Phosphor aus Abfällen und Rückständen untersucht und soll in der industriellen Anwendung forciert werden. Die thermische Behandlung von Klärschlamm bietet hier eine vielversprechende Technologie. In Co-Verbrennung und Co-Gaserzeugung des Klärschlammes mit biologischen Rückständen wie Sonnenblumenschalen und Weizenstroh soll die Bioverfügbarkeit der entstehenden Asche erhöht werden. Aufgrund der leichteren Löslichkeit von Kaliumphosphaten ist die Umwandlung von Ca-Phosphaten zu K-Phosphaten während der thermischen Behandlung anzustreben. Die Co-Verbrennung von Klärschlamm mit biologischen Rückständen mit hohem Kaliumanteil wie Sonnenblumenschalen und Weizenstroh zeigt sich als vielversprechend, da sowohl eine höhere Kaliumkonzentration in den Aschen als auch höhere K-P-Korrelationen detektiert werden können. Die Bodenasche ist hier die aussichtsreichste Fraktion um als Düngemittel wiederverwendet werden zu können. Unter reduzierender Atmosphäre in der Gaserzeugung konnte nicht genug Durchmischung der beiden Brennstoffe festgestellt werden. Das K/Ca-Verhältnis ist hier deutlich geringer als in oxidierender Atmosphäre. Kalium scheint hier eher Verbindungen mit Aluminium und Silizium als Feldspat einzugehen.

Contents

Declaration of academic honesty	ii
Acknowledgements	iii
Abstract	iv
German Abstract	v
Introduction	1
1.1. Importance of phosphorous	4
1.1.1. Phosphorous cycle	5
1.1.2. Accessibility	6
1.1.3. Previous studies concerning co-combustion and co-gasification	8
Implementation of experiments	10
2.1. Fuels	11
2.2. Bubbling fluidized bed	11
2.2.1. Bed material	13
2.2.2. Fluidization	15
2.2.3. Measurement of gas composition	16
2.2.4. Measurement of temperature	17
2.3. Analysis of the ash composition	18
2.3.1. SEM (scanning electron microscope)	18
2.3.2. Light microscopy	20
Experiment parameters	21
3.1. Mass balances	21
3.2. Fuel to fluidization ratio	23
3.3. Temperature and gas composition profiles	23
Results and discussion	27
3.1. Experiment 1	27
3.2. Experiment 2	36
3.3. Experiment 3	45
3.4. Experiment 4	55
3.5. Experiment 5	63
3.6. Experiment 6	72

Conclusion.....	82
List of Figures	84
List of Tables.....	89
Bibliography.....	91

Chapter 1

Introduction

The main goal of both previous and present studies is finding a way for re- and upcycling resources, materials, or elements. Plants require phosphorous (P) to grow. P cannot be substituted by any other element in the periodic table and is therefore vital for food production [1]. Global food production will need to increase by about 70% by 2050 in order to meet the demand according to the International Water Management Institute [2]. This poses a great challenge in acquiring enough phosphorous for food production. The annual global production of phosphate is around 40 million tonnes of P_2O_5 from 140 million tonnes of rock concentrate [3]. Worldwide resources of phosphate rock are more than 300 billion tons, where reserves are around 71 billion tons. The world consumption of P_2O_5 contained in fertilizer and industrial uses was projected to increase from 47 million tons in 2020 to 49 million tons in 2024 [4]. Mineral fertilizers account for around 80%, animal feeds for approximately 5%, industrial uses for about 15%, detergents for 12% and metal treatment for 3% of the total global production of phosphate rock [5]. As for their dominant role in global phosphate consumption, the development of agriculture will play a leading role in the development of future world phosphate production. There are over 30 countries worldwide producing phosphate rock, while the top 12 countries account for almost 95% of the total phosphate production. The three major producing countries are the USA, China, and Morocco. These countries produce about two thirds of the total amount of phosphate [3]. This leads to a dependent relationship between many countries and those previously stated which may also lead to political subordination. In the following tables, supply, demand and balances of phosphate in the world and in Central Europe in particular are portrayed. The potential H_3PO_4 balance worldwide is positive for the year 2020, in Central Europe there is more H_3PO_4 demand than H_3PO_4 available for fertilizer. The difference amounts to -510 thousand tons P_2O_5 in 2020.

Table 1: World phosphate supply, demand and balance in the time frame of 2015-2020 [22] (in thousand tons P₂O₅)

World						
	2015	2016	2017	2018	2019	2020
H₃PO₄ capacity	57 422	58 285	60 955	61 995	63 036	64 677
H₃PO₄ supply capacity	5 684	6 038	6 209	6 528	6 692	6 803
H₃PO₄ industrial demand	41 740	42 356	43 349	44 662	45 670	46 275
H₃PO₄ available for fertilizer	41 151	41 945	43 195	44 120	45 013	45 858
P fertilizer demand	37 635	38 372	39 579	40 469	41 320	42 133
H₃PO₄ fertilizer demand	3 517	3 572	3 615	3 651	3 693	3 725
Non- H₃PO₄ fertilizer demand	3 517	3 572	3 615	3 651	3 693	3 725
Potential H₃PO₄ balance	4 105	3 984	3 769	4 193	4 349	4 142

Table 2: Central Europe phosphate supply, demand and balance in the time frame of 2015-2020 [22]

Central Europe						
	2015	2016	2017	2018	2019	2020
H₃PO₄ capacity	704	704	704	704	704	704
H₃PO₄ supply capacity	350	350	350	350	350	350
H₃PO₄ industrial demand	102	102	103	103	104	104
H₃PO₄ available for fertilizer	248	248	247	247	246	246
P fertilizer demand	746	780	807	835	864	889
H₃PO₄ fertilizer demand	643	663	686	710	735	756
Non- H₃PO₄ fertilizer demand	113	117	121	125	129	133
Potential H₃PO₄ balance	-395	-416	-429	-463	-488	-501

Currently there are reserves, deposits that are exploitable in an economically viable way, and resources that could be accessed with enhanced technology in the future. Neither have an infinite lifespan [6]. Existing rock phosphate reserves could be exhausted in the next 50–100 years [3]. The resources are finite, and it is of interest to find a way to recycle phosphorous and feed it back into the phosphorous cycle. Human waste, defined here as human faeces and urine, is accountable for 13% of the overall P loss in the phosphorous cycle [1]. Hence, studies have been conducted to collect data about recycling phosphorous from sewage waste for fertilizer usage.

Phosphorous recovery is performed mainly by transferring P from the solid phase of the sludge to the liquid phase with acid/alkali treatment [7], with FeCl_3 hyphen to assisted hydrothermal treatment [8], and transformation mechanisms via aerobic and anaerobic with a FeCl_3 dosing membrane bioreactor (MBR) via side stream fermentation [9]. Different species of apatite (i.e. calcium phosphate with quartz, calcite, dolomite, clay and iron oxide as gangue components) are the most prevalent phosphate minerals in the rocks [3]. It is widely gangue that the exploitation of resources and soil around the world can't continue as it is.

As is commonly known, there is an upward trend in the average global temperature. Surface temperature has risen 0.07 °C every 10 years since 1880. Land areas have warmed faster with a 0.10°C average per decade compared to 0.06 °C per decade for ocean temperatures [10]. Up to a point, plants grow faster when the air temperature increases, but extreme heat will increase moisture loss and slow down growth. Change in climate affects the distribution and occurrence of crops. For many plants a chilling period of a certain amount of time is necessary before growth can be resumed in spring. It is possible that some plants native to areas further south with a shorter chilling requirement will resume growth during a warm period in winter and then be damaged when cold weather returns [10].

There is both upside and a downside to fertilizer usage. It maximizes crop yield, but also consumes fossil fuel energy for its production. Furthermore, energy is consumed by applying the fertilizer which leads to further GHG (greenhouse gas) emissions. In Table 3 an overview of the effects of climate change on agriculture is shown. As a rising CO_2 level is generally good for crops as it increases photosynthesis, rising temperatures disturb the established natural biorhythm of crops. Depending on crops and regions, growing seasons could be faster, shorter, or earlier. There is a heat stress risk to be considered. Due to effects on the weather variability, there is severe risk of damaging occurrences such as heat waves, frost, droughts and floods.

Table 3: predicted effects of climate change on agriculture over the next 50 years [11]

Climatic Element	Expected Changes by the 2050s	Confidence in Prediction	Effects on Agriculture
CO ₂	Increase from 360 ppm to 450–600 ppm (2005 levels now at 379 ppm)	Very high	Good for crops: increased photosynthesis; reduced water use
Sea level rise	Rise by 10–15 cm. Increased in south and offset in north by natural subsistence/rebound	Very high	Loss of land, coastal erosion, flooding, salinization of groundwater
Temperature	Rise by 1–2°C. Winters warming more than summers. Increased frequency of heat waves	High	Faster, shorter, earlier growing seasons, range moving north and to higher altitudes, heat stress risk, increased evapotranspiration
Precipitation	Seasonal changes by ±10%	Low	Impacts on drought risk, soil workability, water logging, irrigation supply, transpiration
Storminess	Increased wind speeds, especially in north, more intense rainfall events	Very low	Lodging, soil erosion, reduced infiltration of rainfall
Variability	Increases across most climatic variables. Predictions uncertain	Very low	Changing risk of damaging events (heat waves, frost, droughts floods) which effect crops and timing of farm operations

As human intervention in nature causes change in nature itself, recycling is not only a way to prevent further exploitation but also a way to adapt to the rising demand of certain products due to climate change. Sewage sludge contains organic matter, microelements, and biogenic elements (among others, nitrogen and phosphorous), but also an excessive amount of heavy metals and pathogenic organisms [12]. Therefore, its usage in agriculture seems promising if, not when the heavy metal content can be reduced. It is particularly relevant which extent phosphorous can be regained in a bio-available state. The concentration of copper, cadmium, iron etc. and pathogenic organisms poses problems in sanitary, chemical, and environmental safety standards that prevent recycling in a natural environment.

1.1. Importance of phosphorous

There are 17 nutrients that are essential for plant growth and whose functions cannot be performed by any other nutrient. Phosphorous is one of them and thus required for the optimal growth and reproduction of the plant. It cannot be substituted or obtained from the atmosphere. In agricultural crops the concentration of phosphorous varies from 0.1 % to 0.5 %. It is perceived through the outermost layers of root cells, root tips and through root hairs [6]. Phosphorous cannot be metabolized by the plants in any given configuration. It is taken up mostly as primary orthophosphate (H₂PO₄⁻) and as secondary orthophosphate (HPO₄²⁻) with increasing pH of the soil. It can be stored in the roots or transported to the upper part of the plant to be incorporated into organic compounds, as DNA, RNA, phosphoproteins, phospholipids, enzymes, and energy-rich

An important part of the phosphorous cycle is the transformation of phosphorous via the immobilization and mineralization process. It is possible for inorganic phosphorous, applied as fertilizer, to be incorporated as organic phosphorous forms and therefore to be made accessible for plants. Not all dynamics and processes occurring in nature that concern phosphorous are totally understood yet [6].

1.1.2. Accessibility

Even though phosphorous ranks 11th in order of abundance in the earth's crust, the concentration in rocks is generally small. There are numerous forms of phosphorous present in soil e.g., in discrete calcium phosphate minerals, in adsorbed form associated with surfaces of silicate or in absorbed form in aluminium minerals or iron oxides. It is prevalent as soluble apatite [$\text{Ca}_{10}\text{X}(\text{PO}_4)_6$ where X can be OH^- , Cl^- or CO_3^{2-}] and other soluble calcium phosphates (e.g., $\text{Ca}_8\text{H}(\text{PO}_4)_6 \cdot \text{H}_2\text{O}$). The input of phosphorous to the soil by weathering of Ca minerals can be very low [10].

It is assumed that the weathering rates of phosphorous range from 0.2 to 3.0 kg per ha per year. The total estimated input is 40 Gt per year. This is low compared to the input through fertilizers which amounts to around 210 Gt per year [6]. As seen in Figure 3, the availability of phosphorous for plants depends on whether the adsorption to soil minerals is rather strong or weak. Bonding energies define the grade of adsorption and the more strongly adsorbed phosphorous is, the less available it is for the plants to take in [6].

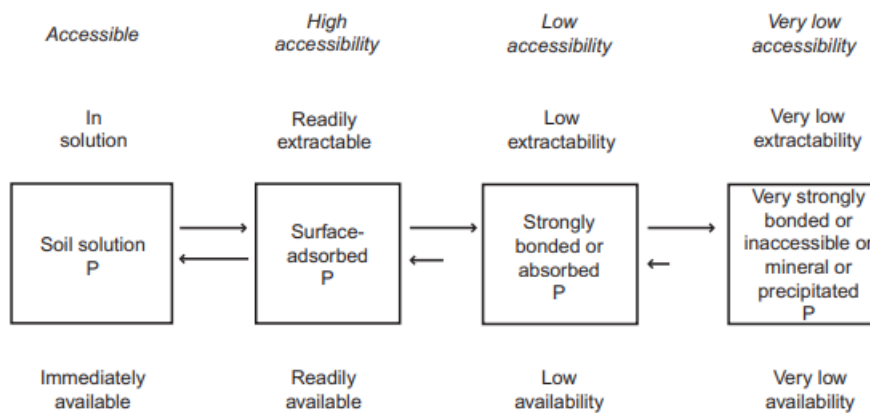


Figure 3: Phosphorous accessibility for plants [6]

The availability of organic phosphorous depends on microbial activity to break down organic matter and thereby release plant-available phosphorous. Thus, conditions in both the soil and the weather are decisive for the availability of organic phosphorous. In warm moist conditions, good physical soil properties and optimum soil pH and nutrient levels, the mineralization of organic phosphorous to inorganic forms is favoured. The inorganic phosphorous can then be bound to iron and aluminium compounds in the soil. The organic phosphate of deceased creatures leads to replenishment of the soil solution with phosphate in inorganic forms by the slow dissolution of these minerals. The solubilities of phosphorous compounds are directly related to the pH of the soil [15].

In Table 4 common phosphorous fertilizers, their sources and some important properties are listed. If fertilizers are manufactured by treating rock with acid, Ca-orthophosphates are gained. The reaction of anhydrous ammonia with phosphoric acid leads to ammonium phosphates. The most commonly used triple superphosphate with 46% P_2O_5 is diammonium phosphate (DAP) [15]. The phosphates derived from combustion or gasification of sewage sludge differ from those common fertilizers in purity and exact configuration.

Table 4: Common phosphorous fertilizers and their sources [15]

Material	Analysis	Comments
Calcium orthophosphates	Manufactured by treating rock phosphate with acid	
Ordinary superphosphate	20% P_2O_5 90% water soluble, 8-10% sulphur	Not used anymore in commercial crop production. Replaced by triple-superphosphate
Triple superphosphate	45% P_2O_5 90% water soluble, no sulphur	Common material used in no-nitrogen blends
Ammonium phosphates	Manufactured by reacting anhydrous ammonia with phosphoric acid	
Monoammonium phosphate map	52% P_2O_5 11% N, 100% water soluble	Very high phosphorous analysis. Excellent material for use in starter fertilizer
Diammonium phosphate dap	46% P_2O_5 10% N, 100% water soluble	Most common phosphorous fertilizer used extensively as the basis for blended fertilizers
Ammonium polyphosphate	Solid: 55% P_2O_5 11% N Liquid: 34% P_2O_5 10% N	Liquid form is very common, N and P fluid fertilizer
Miscellaneous phosphates		
Rock phosphate with very low water solubility	27-45% total phosphorous recommended for soluble P fertilizer	Must be finely ground to be effective. Increase rate 3 to 4 times that

1.1.3. Previous studies concerning co-combustion and co-gasification

The combustion of sewage sludge (SS) has not yet shown the desired output in bio-available phosphates. Therefore, co-combustion and co-gasification of sewage sludge pellets with agricultural residues is performed in order to gain other forms of phosphates. In a thermochemical equilibrium study of ash transformation during the combustion and gasification of sewage sludge mixtures with agricultural residues, the mixing ratio of sewage sludge (SS) with other biological residues is further investigated [16]. The main field of interest is the phosphorous speciation. For this purpose, biological residues as sunflower husk (SH) and wheat straw (WS) were used. Chemical compositions different to the one of sewage sludge give reason to apply those two in particular. Sunflower husk and wheat straw pellets show smaller Fe, Al and Ca concentration, but a greater share of K. The wheat straw fuel has a significantly greater Si share than the sunflower husk fuel and notably more chloride than both other fractions (Table 5, Table 6 and Table 7). As the biological residues are lean in phosphorous, blending of the fractions may lead to the desired outcome of bio-available phosphates. The aim is to gain K-bearing phosphates as they are less stable than e.g. Ca-phosphates or Fe-phosphates [16].

Table 5: fuel composition, sewage sludge

SS	ash	C	H	N	O	K	Na	Ca	Mg	Fe	Al	Si	P	S	Cl
g/kg dry	32.60%	379	52	51	341.6	3.93	2.33	27.1	3.74	53.2	15.1	28.9	29.1	12	0.961

Table 6: fuel composition, sunflower husk

SH	ash	C	H	N	O	K	Na	Ca	Mg	Fe	Al	Si	P	S	Cl
g/kg dry	2.80%	513	63	6.5	401.9	7.46	0.011	3.6	1.75	0.115	0.027	0.32	0.72	1.3	0.34

Table 7: fuel composition, wheat straw

WS	ash	C	H	N	O	K	Na	Ca	Mg	Fe	Al	Si	P	S	Cl
g/kg dry	4.1%	475	58	4.4	438.0	8.25	0.042	2.76	0.7	0.12	0.16	9.25	0.585	0.655	2.03

The elements derived from sewage sludge dominate the characteristics of the fuel for a wide range of the fuel-mixing ratios. If a mixing ratio of 50/50 is used, the fuel does not differ significantly from pure SS and its chemical reaction potential. The ash of a 50/50 mixture of sewage sludge and sunflower husk (SSH) and sewage sludge and wheat straw (SWS) contains about 90 mol% elements

derived from sewage sludge fuel. Therefore, mixing ratios with 15% sewage sludge or lower are used in the experiments that will be further explained in Table 8 [16].

The previous experiments show that with higher shares of agricultural residue in the fuel blend the percentage of K increases. This leads to a depletion of P, Fe, and Al. As the research in the thermochemical equilibrium study of ash transformation during combustion and gasification of sewage sludge mixtures with agricultural residues by Hannl, Sefidari, Kuba, Skoglund and Öhman [16] has shown, most of the analysed mixtures of SSH formed substantial amounts of volatilized K compounds mainly as K_2CO_3 and in hydroxides (KOH) at higher temperatures. The primary goal of the series of experiments is to obtain phosphorous in a chemical structure that is accessible to plants. Certain groups of elements in association with P (Ca/Mg, K(+Ca/Mg), Fe/Al) might facilitate the determination of this plant-available P fractions. K-phosphates are thermodynamically favoured in a P-limited ash environment. The shift from Ca/Mg phosphates and Fe/Al/Si phosphates towards K-phosphates is desired to facilitate the recovery of P. The results of the study are in accordance with previous findings of the possible change of P speciation in sewage sludge ashes by adding alkali-rich additives [17]. P species are dependent on fuel blend, process temperature and gas atmosphere. When applied as fertilizer, an individual group of phosphates shows similar behaviour [18] [19]. For the calculations, equilibrium conditions were assumed and the role of the plant, the soil, and the varying plant availability within one group was neglected in the potential P associations in the fuel blends. For the shift from Ca, Fe and Al phosphates towards K phosphates, kinetic limitations were set aside and the process was regarded as a solid-solid reaction. It is furthermore assumed that $KMgPO_4$ phosphates are the thermochemically favoured form in this system. This would suggest that other stable phosphates that have formed previously e.g., $Ca_3(PO_4)_2$ would disintegrate to make P available for the reaction with excess K. That, however, is not a given considering the stability of the Ca phosphates [16]. In the thermochemical equilibrium study the effects of melt formation on the formation of K phosphates was investigated at higher temperatures. K and P show higher a tendency to be incorporated in the melt than Ca. Partial formation of melt could enhance the formation of K-bearing phosphates [16]. In the experiments conducted in this study, melting behaviour was unwanted and not to be investigated in this context. Due to the melting effects, the combustion and gasification temperature was held constant at 800 °C.

Chapter 2

Implementation of experiments

To investigate the correlations between phosphorous and other elements of the co-combustion and co-gasification of sewage sludge with agricultural residues, six experiments were conducted as shown in Table 8. Dried pellets of 100% sewage sludge (SS), 15% sewage sludge plus 85% sunflower husk (SH) and of 10% sewage sludge plus 90% wheat straw (WS) were used as fuel. The blend SSH15 of 15% SS and 85% SH was used as fuel 2. The blend WSS10 of 10% SS and 90% WS was used as fuel 3. To see the effect of different conditions, combustion and gasification conditions were used for all three kinds of fuel. The first three experiments were conducted in oxidizing atmosphere. The last three were conducted in reducing atmosphere.

Table 8: Six different experiments with three different fuels were conducted

	Experiment 1	Experiment 2	Experiment 3	Experiment 4	Experiment 5	Experiment 6
Fuel	Fuel 1 100% SS	Fuel 2 15% SS, 85% SH	Fuel 3 15% SS, 90% WS	Fuel 1 100% SS	Fuel 2 15% SS, 85% SH	Fuel 3 15% SS, 90% WS
Process conditions	Combustion Excess air	Combustion Excess air	Combustion Excess air	Gasification- Sub- stoichiometric application of air	Gasification- Sub- stoichiometric application of air	Gasification- Sub-stoichiometric application of air

2.1. Fuels

The fuels used were sent from Sweden in the compositions needed as dried pellets (Figure 4). In Table 9 the elemental composition of the fuel blends is displayed.



Figure 4: Fuels used in the experiments: fuel 1 (left), fuel 2 (middle) and fuel 3 (right)

Table 9: Elemental composition of SS (1st), SSH15 (2nd) and WSS10 (3rd)

SS	ash	C	H	N	O	K	Na	Ca	Mg	Fe	Al	Si	P	S	Cl
g/kg dry	32.60%	379	52	51	341.639	3.93	2.33	27.1	3.74	53.2	15.1	28.9	29.1	12	0.961

SSH15	ash	C	H	N	O	K	Na	Ca	Mg	Fe	Al	Si	P	S	Cl
g/kg dry	7.27%	492.9	61.4	13.2	392.8	6.91	0.36	7.13	2.05	8.08	2.29	4.61	4.98	2.91	0.43

WSS10	ash	C	H	N	O	K	Na	Ca	Mg	Fe	Al	Si	P	S	Cl
g/kg dry	7.27%	465.4	57.4	9.06	428.41	7.82	0.27	5.19	1.00	5.43	1.65	11.22	3.44	1.79	1.92

2.2. Bubbling fluidized bed

For the combustion and gasification of the fuels, a bubbling bed reactor is used. This is characterized by the fluidization of particles via fluidization gas. The gas flows from a porous bottom to the top. When the minimum fluidization velocity of the gas is reached, bubbles begin to form, and the articles can no longer be defined as a fixed bed. This state brings advantages to the mixing and to the equal distribution of gas and temperature [20].

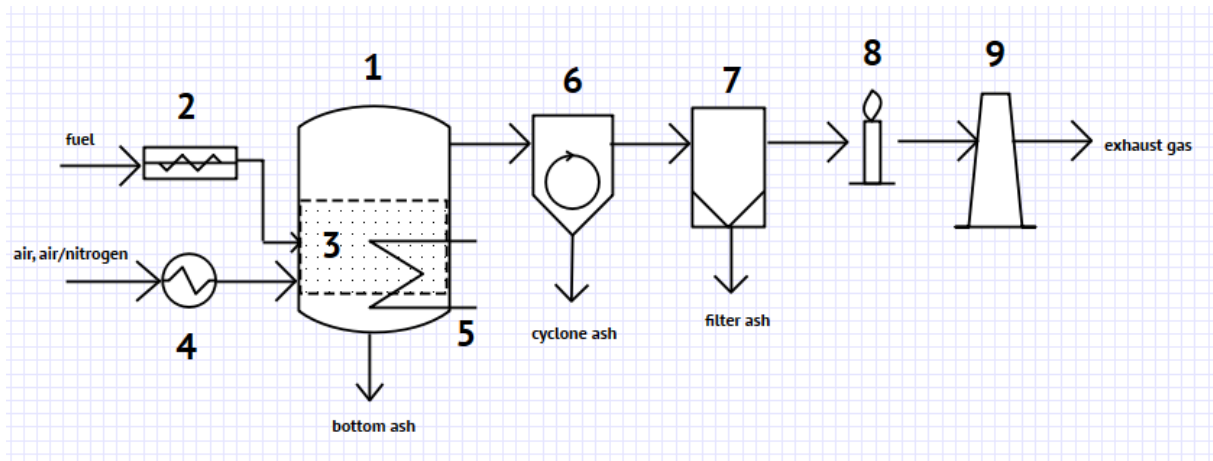


Figure 5: Flow chart of the process

- | | |
|---|------------------------|
| 1...housing of the bubbling bed reactor | 7...quartz wool filter |
| 2...screw conveyor | 8...torch |
| 3... bubbling bed | 9...chimney |
| 4... heat exchanger | |
| 5... coat heat exchanger | |
| 6...cyclone | |

The experiments were conducted in a 5KW bubbling bed fluidized bed reactor at the Technikum of TU Wien shown in Figure 6.



Figure 6: bubbling fluidized bed reactor

The bubbling bed reactor is constructed from stainless steel and has an inner diameter in the fluidised bed section of 13.6 cm and of 30 cm in the freeboard section. The whole reactor is covered with an isolating layer to minimise heat loss. Two bunkers and a conveyor screw supply a steady flow of feed. Only the smaller bunker is used for the experiments conducted. To prevent exhaust gas from flowing back to the bunkers and to maintain an inert atmosphere, the bunkers are flushed with N_2 .



Figure 7: Bunkers and flushing system used during the experiments: small bunker (left), big bunker (middle), N₂ flush of bunkers (right)

The feedstock is carried by a screw conveyor to the bubbling bed. The rotation speed of the screw determines the amount of feed being inserted into the reactor.



Figure 8: The feed flow is regulated by setting the rotation frequency of the screw conveyor (displayed on the left). The screw conveyor can be seen on the right.

The flange at the bottom of the reactor can be taken off to collect the bed material and bottom ash after the experiment. The product gas is led through a cyclone in order to separate out the coarse particles and then to a filter filled with quartz wool. There fine ash particles are separated there from the gas flow. The filtered gas then flows to the torch where it is burned with CH₄ to reduce CO emissions.

2.2.1. Bed material

Two kilograms of quartz sand were used as bed material for each run. The fire-dried silica is of 0.1 – 0.2 mm in average diameter and produced by Quarzwerke. To characterize the bubbling bed and its

conditions, the specifications of the bed material and the fuel must be considered. The average density of the quartz sand used is 2650 kg/m³. Therefore, the difference in density of quartz sand and air is 1098.8 kg/m³.

$$\rho_P - \rho_{gas} = 2650 \frac{kg}{m^3} - 1.2 \frac{kg}{m^3} (bei 20^\circ C) = 2648.8 \frac{kg}{m^3}$$

The bed material would have to be categorized as sand-like, as the average diameter of the particle size of the quartz sand varies between 100 μm and 200 μm (Figure 9). The fuel pellets are bigger than the bed material and cylindrically shaped.

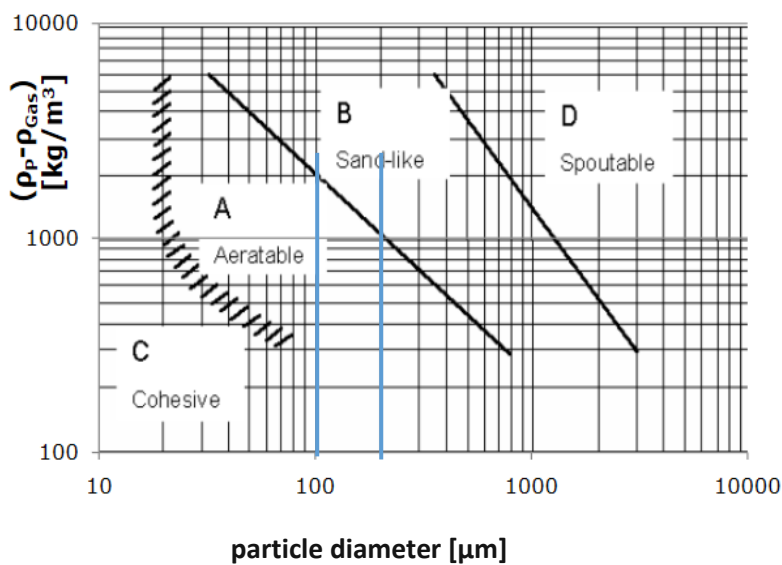


Figure 9: Geldart figure for estimating the behaviour of particles according to their density and size [22]

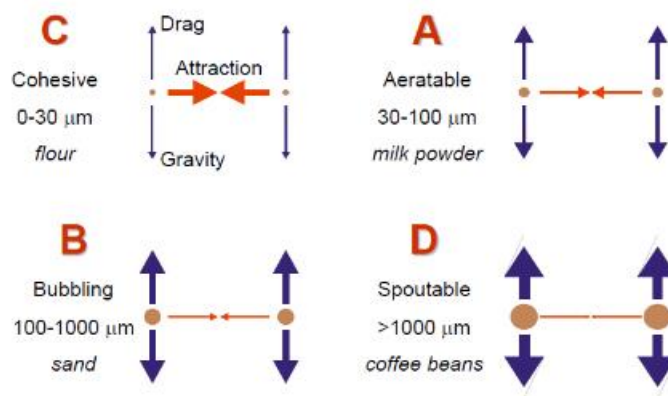


Figure 10: Forces on the particles relevant for classifying after Geldart [20]

Materials of type B after Geldart are bubbling. The cohesive forces in this group are negligible. Immediately after surpassing the loosening velocity, the bed starts to form bubbles that provide good mixing conditions. Group B is the most important for industrial application in fluidized bed reactors [20].

2.2.2. Fluidization

Fluidization is carried out with preheated air in the experiments 1-3 and with air and nitrogen in the experiments 4-6 for providing gasification conditions. Throughout the experiment conditions were adjusted as needed, but an average flow of 6000 l/h was implemented.

Typical values for the air-to-fuel ratio of combustion lie between 1.3 and 2.0, those of gasification between 0.3 and 0.6. This was achieved by setting the fluidization flow of air in a distinct ratio to the mass flow of the fuel. In the appendix the actual values of lambda regarding the whole process are given. They were measure in an interval of approximately 10 seconds. For gasification a much lower lambda value must be acquired. Therefore, air and nitrogen were used for fluidization. As gasification is an endothermic reaction, enough energy must be provided by high temperatures in the heating devices. In the beginning of the experiment energy was provided by combusting some of the fuel. Later on, the air was reduced and the nitrogen level was raised step by step. The steps in which this was applied are also shown in detail in the appendix. When the desired lambda had been reached, the gasification was performed for about 90 minutes. The air to nitrogen ratio was adjusted by two rotameters as shown in Figure 11.

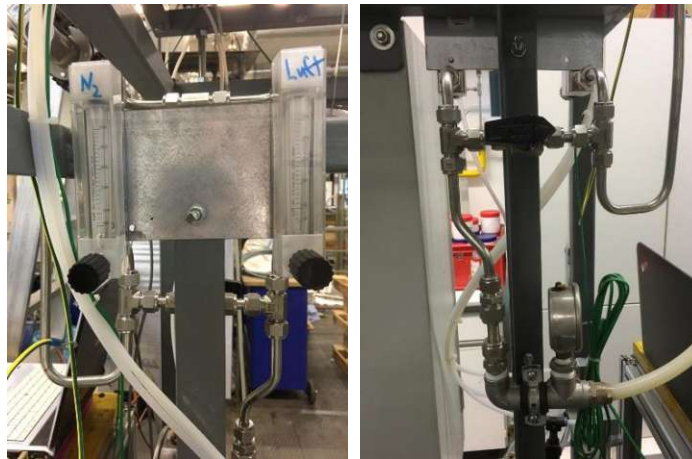


Figure 11: Rotameter (left) and valve (right)

2.2.3. Measurement of gas composition

For the measurement of the gas composition, a fraction of the exhaust gas is pumped to a cooler before the gas is fully combusted in a torch. The gas is cooled down to a temperature of 5°C. Afterwards a fraction of the cooled gas is bypassed to the measuring device where the CO, CO₂, CH₄, H₂ and O₂ levels are continuously measured. Gas composition provides the information about the reactions that take place inside the reactor.

2.2.4. Measurement of temperature

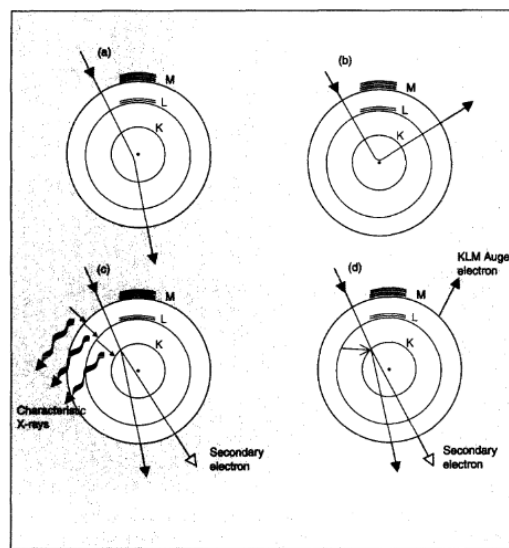
Seven temperature sensors have been installed through the whole reactor. Temperature is measured in the preheater of the fluidization gas and in the heating jacket of the reactor itself. In order to heat up the reactor slowly and evenly, the temperature are increased step-wisely by 30°C in 10 min. This is necessary to avoid overshooting the temperature aimed for. The other five heat sensors are positioned in the reactor itself, three of them in the bubbling bed, one in the splash zone and one in the free board.

At the top and at the bottom of the bubbling bed the pressure is measured in order to determine the pressure drop over the bed. This measurement was faulty during most of the experiments so the results are not reliable. In the first experiment the tube for the exhaust gas was clogged and there was sand in the tubes leading from the reactor to the manometer. This was corrected, but still no improvement in the measurement could be achieved. The results will be attached in the appendix.

2.3. Analysis of the ash composition

2.3.1. SEM (scanning electron microscope)

In the scanning electron microscope electrons are used gain information about the object of interest. The incident electrons ejected from an electron gun typically have energies of 2-40 keV. The electron beam is then demagnified by an electromagnetic condenser in order to scan the specimen surface in a grid by scan coils. In a conventional SEM, signals emerging from the surface of the specimen give information about the composition. If the probe is thicker, electrons are not transmitted through the probe. Particles like electrons, x-rays and photons are scattered or emitted [23]. There are various ways of the electron interacting with another atom. These interactions are shown in Figure 12.



The inner electron shells of atoms are labelled according to standard notation (K, L, M)

Figure 12: The electron can interact with the atom in the following ways: (a) low angle scattering, (b) back or high-angle scattering, (c) emission of a secondary electron and characeristic x-rays, (d) emission of a secondary electron and an Auger electron [23]

SEM can provide information on crystalline structure, chemical composition, topography, and electrical behaviour of the top 1 μm of the specimen. The specimen is penetrated in a teardrop-shaped volume whose dimensions are determined by the energy of the electron beam, the atomic mass of elements in the specimen and the angle at which the electron beam hits the probe [23]. The interaction of electron and specimen is shown in Figure 13.

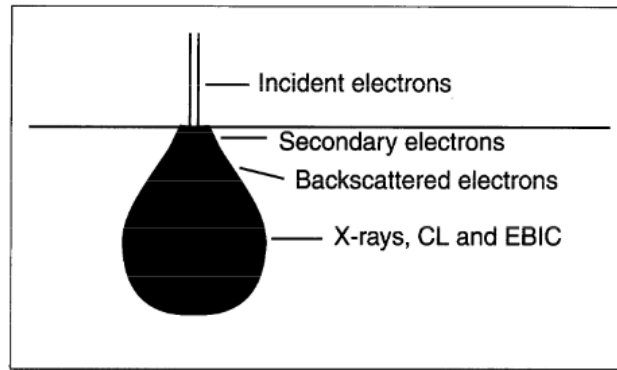


Figure 13: The electron beam interacts with atoms up to a specific specimen depth. Backscattered electrons and x-rays are emitted from these regions [23]

Secondary electrons are those that are knocked out of their orbits by an incident electron. They escape from the specimen with energies below 50 eV. This only happens in a near-surface layer of the material and the signal comes from an area about the size of the electron beam. In case of secondary electrons it is primarily the topographic information that can be collected. Backscattered electrons on the other hand are those incident electrons that come sufficiently close to the nucleus of an atom and are scattered through a large angle and remerge from the surface. They have much higher energies than secondary electrons. The resolution given by them is slightly inferior to the resolution by secondary electrons because secondary electrons are emitted from deeper in the specimen. Therefore, the area from which the signal arises is bigger than the beam diameter. The backscattered electrons provide information about the composition. Elements of higher atomic mass give a brighter contrast [23].

For the analysis of the ash probes, the emission of X-rays gives information about the composition. Incident electrons provide the energy for secondary electrons to jump to other energy levels. When falling back into place they emit X-ray radiation. A spectrum is logged over different eV intensities that would trigger electrons in the shell of certain elements. The size of the peak at that specific intensity provides information about the molar percentage of this element. A sample spectrum is shown in Figure 14.

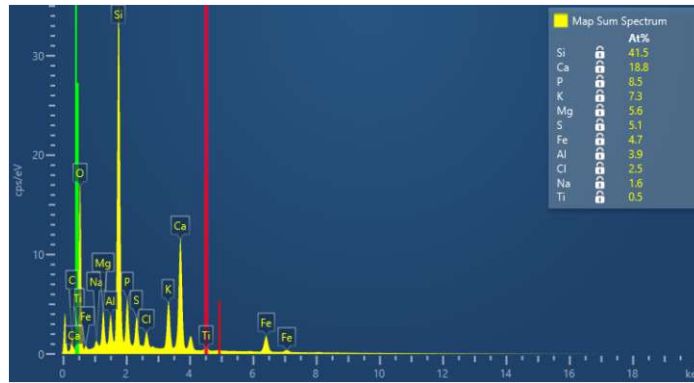


Figure 14: The SEM analysis gives a spectrum of peaks of different heights at intensities characteristic for each element

2.3.2. Light microscopy

In light microscopy the fine detail of an object can be visualized by using a series of glass lenses to create a magnified image of the specimen. Convex objective lenses are used to enlarge the image formed by focussing a beam of light onto or through an object [24].

Chapter 3

Experiment parameters

3.1. Mass balances

For each fuel the mass percentage of ash is given in the fuel composition data sheet. The total ash that is to be collected at the bottom, from both the cyclone and from the filter, is calculated by multiplying the mass fraction of the ash in the fuel with the total mass of fuel combusted.

Equation 1

$$w_{Ash} * (m_{fuel,out} - m_{fuel,in}) = m_{ash_bottom} + m_{ash_cyclone} + m_{ash_filter}$$

In Table 10 the data for calculating the mass balances is given. The ash fractions of the bottom, the cyclone and the filter are given in Table 11. When comparing the calculated ash fraction and the total ash fraction weighted, the mass balance does not add up. The difference in mass amounts to 0.0715 (16.25 %), 0.0517 (43.08 %); 0.0423 (35.25%); 0.2708 (49.24%); 0.0091 (9.1%); and 0.0238 (35.38 %) for the six runs. Thus, it can be assumed that it was not possible to collect some of the ash which subsequently was lost through the chimney. Furthermore, it was not possible to separate the bottom ash from the bed material. Because a sieve of 2mm mesh size was used, the smaller particles are not represented in the mass balance. In run 3, 5 and 6 the bottom ash could not be separated from the bed material at all. Therefore, the bottom ash was estimated to be the difference between the total weight and the bed material inserted primarily to the runs. This poses the risk that the bed material carried out by the exhaust gas leads to misrepresentation of the actual bottom ash mass.

Table 10: Data for calculating the produced ash in total with Equation 1

Mass of fuel feed [kg]	3.60	3.23	2.93	3.52	1.81	2.02
Mass of fuel remaining [kg]	2.25	1.59	1.24	1.83	0.48	0.81
Mass of fuel combusted [kg]	1.35	1.64	1.69	1.69	1.33	1.21
Mass fraction of the ash in the fuel	0.326	0.0727	0.0695	0.326	0.0727	0.0695
m_ash [kg]	0.44	0.12	0.12	0.55	0.10	0.08

Table 11: Weighted ash mass fractions of bottom ash, cyclone ash and filter ash

bottom ash [kg]	0.1946	0.01897	0.032	0.1934	0.022	0.002
cyclone ash [kg]	0.1596	0.0412	0.0376	0.0588	0.04	0.03211
filter ash [kg]	0.0143	0.0081	0.0081	0.027	0.0289	0.0176
ash total [kg]	0.3685	0.0683	0.0777	0.2792	0.0909	0.0517
bottom ash [%]	53%	28%	41%	69%	24%	4%
cyclone ash [%]	43%	60%	48%	21%	44%	62%
filter ash [%]	4%	12%	10%	10%	32%	34%

In Figure 15 the mass percentages of the ash fractions in each experiment are given. These depend greatly on the fuel and on the operation conditions. When only sewage sludge is used, the bottom ash fraction is the largest followed by the cyclone ash fraction. The filter ash mass fraction is small compared to that in experiments 2 and 3. Combustion of fuel of 100% sewage sludge leads to large particles that are primarily found in the bottom ash. Erosion and friction do not seem to produce too many small particles. The results differ for fuel 3 and fuel 2. When sunflower husk is added to sewage sludge smaller particles are formed in combustion, and the mass fraction of the cyclone ash amounts to 60% of the total ash mass (as shown in Table 11). With wheat straw as an additive, a similar though less severe shift to smaller particles can be perceived. This can be traced back to the difference in hardness and erosivity.

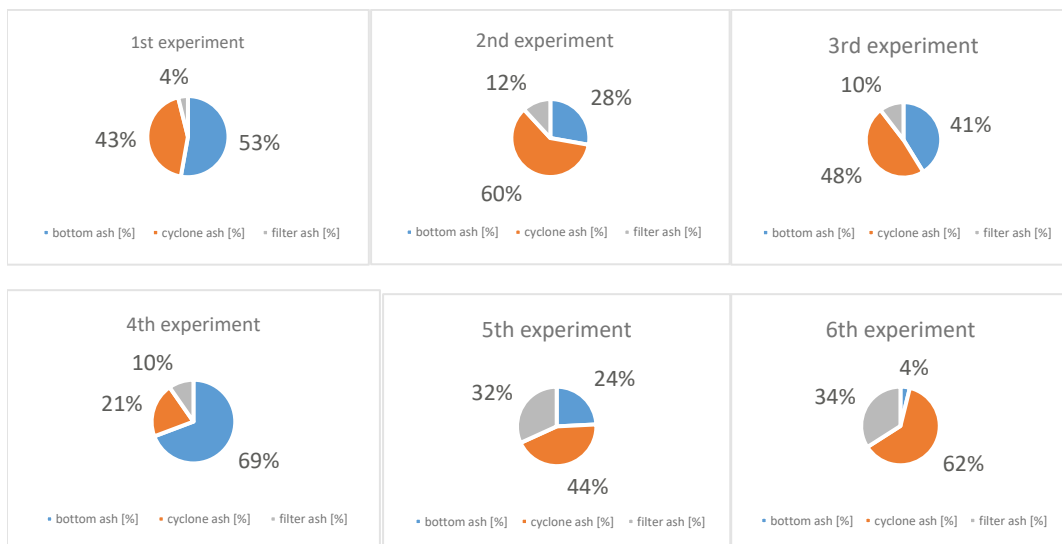


Figure 15: The ash fractions amount to different percentages of the total ash depending on the experiment

Under gasification conditions the ash fraction of the filter ash becomes more dominant for all three fuels. The decisive reasons for the disparity in mass percentages could be the different reactions in a more reductive atmosphere. The total ash mass is less than in the same experiment under oxidising atmosphere. More volatile molecules and fewer solid oxides seem to form.

Table 12: Comparison of the expected ash mass fractions versus the real ash mass fractions

	1 st experiment	2 nd experiment	3 rd experiment	4 th experiment	5 th experiment	6 th experiment
Expected ash mass fraction	32.6 %	7.27 %	6.95 %	32.6 %	7.27 %	6.95 %
Real ash mass fraction	27.3 %	4.16 %	4.60 %	16.52 %	6.83 %	4.27 %

3.2. Fuel to fluidization ratio

In Table 13 the fuel to fluidization ratio is given for all six experiments. In the first three, a λ value of 1.3 was to be achieved. This was not the case for any of the experiments. In experiment 1 more air was used for fluidization because of the clogged exhaust gas tube. For the combustion conditions an oxygen percentage of 12 % in the exhaust gas was the determining parameter. This parameter was kept constant at that value which led to a slightly higher λ value being used. At gasification conditions the aspired λ value of 0.3 was also exceeded to some extent. The determining parameter for the experiments was an oxygen percentage in the exhaust gas of around 0% for stoichiometric gasification.

Table 13: Average lambda values in the experiments 1-6

	1 ST EXP	2 ND EXP	3 RD EXP	4 TH EXP	5 TH EXP	6 TH EXP
λ	5.60	2.15	2.09	0.67	0.55	0.53

3.3. Temperature and gas composition profiles

In Figure 16 the temperature profile of experiment 1 is given. The reactor itself and the fluidization gas are heated externally. It can be observed that the fuel was added when the reactor reached around 500°C. There is a steeper rise in temperature as a result of the combustion reaction which is exothermal. Heating becomes obsolete and the energy for combusting at 800 °C is provided by the oxidisation of the fuel itself. The experiment was run for 5 hours and 13 minutes including the

preheating. 1.35 kg fuel was combusted in 3 hours and 20 minutes. In the first experiment, the tube leading to the chimney was clogged. Therefore, the measurement at the beginning is not representative. Because of the unexpected values in the gas measurement, the fluidization was first increased, and the conveying of fuel was reduced. This was later corrected. Therefore, the temperature profile is not consistent overall.

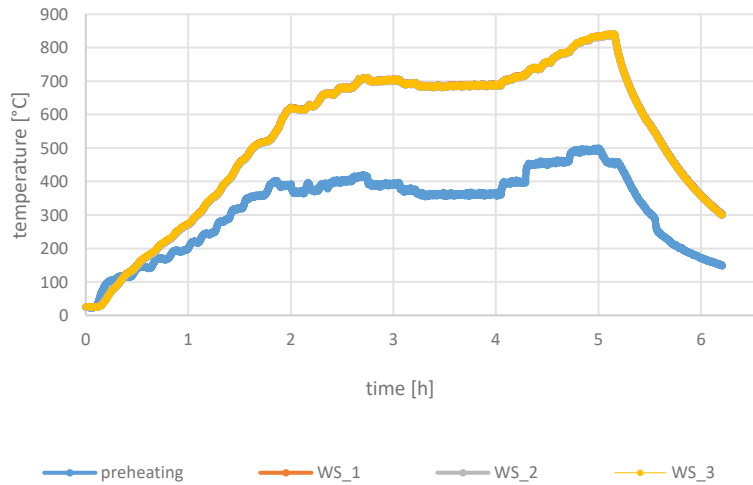


Figure 16: The heating, combustion and cooling down periode of experiment 1 are portrayed in the temperature profile

It was possible to fix the problem four hours after starting the preheating process. The percentage of O₂ decreases and the percentage of CO₂ in the product gas increases as expected for combustion. The values stabilize at around 4 hours 40 running time. The feed was increased again after fixing the problem which led to a rise in temperature as seen in Figure 16. All other measured components in the gas are negligible in their presence. Throughout the experiment it was aimed to keep the percentage of O₂ at 12%. This was achieved at the end of the run as seen in Figure 17.

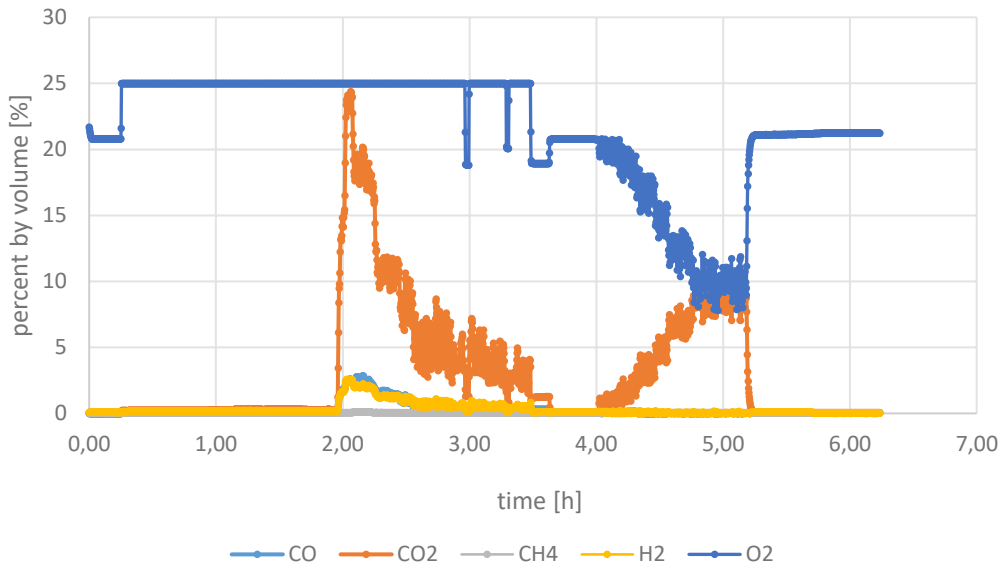


Figure 17: Gas composition profile of experiment 1

The temperature profile of experiment 2 in Figure 18 is representative for all the experiments conducted. The fluidization gas and the reactor are preheated. The temperature is increased by 30 °C every 10 minutes until a temperature of 500 °C is reached. This takes around 1 hour and 40 minutes after which the screw conveyor is set to 20 and later 30 Hertz. The mass flow is estimated from a calibration curve measured for fuel 2 and given in Table 14.

Table 14: The rotation frequency of the screw conveyor is calibrated according to the resulting mass flow of each fuel in a calibration curve

Hz	g/min
20	5.35
30	9.36
40	13.03
50	16.12

The temperature in the reactor rises immediately after feeding the fuel. Within a few minutes of combustion, the temperature could be kept constant at 800°C. It can be seen that the temperature in the splash zone and in the freeboard is significantly lower than in the bubbling bed. After 4 hours the conveying of fuel is stopped, and the heating is turned off. With the fluidization left running, the reactor is cooled down over a period of a few hours.

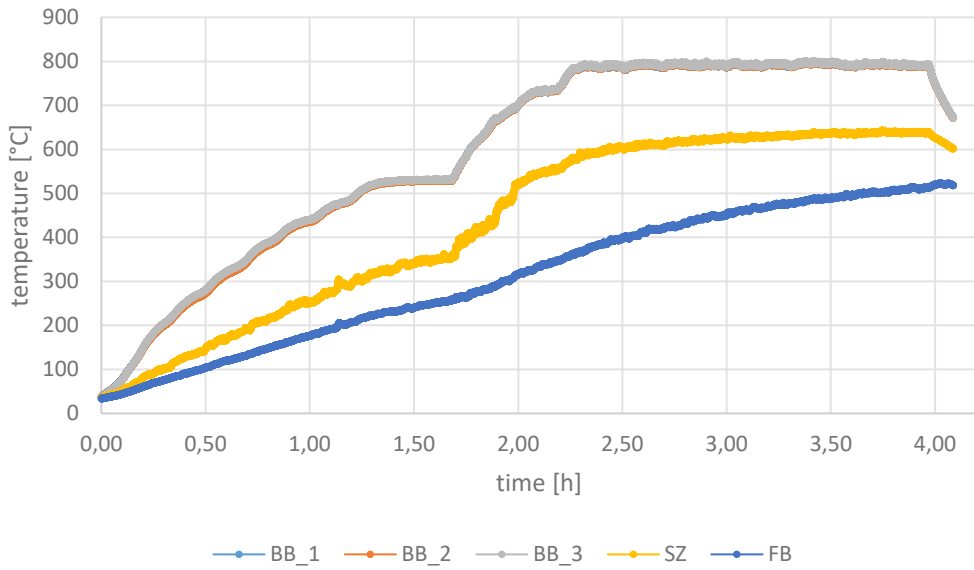


Figure 18: Temperature profile of experiment 2

The gas measurement is coherent with the observation of the temperature measurement. At 1 hour 40 minutes running time the percentage of O_2 drops to around 13 % and the percentage of CO_2 in the product gas rises to around 8 %. The conditions stay constant during combustion. 1.638 kg fuel were combusted in 2 hours 18 minutes. The duration of the combustion or gasification of each experiment varies but amounts to approximately 2 hours. The temperature and gas composition profile of experiments 3-6 are given in appendices I and II.

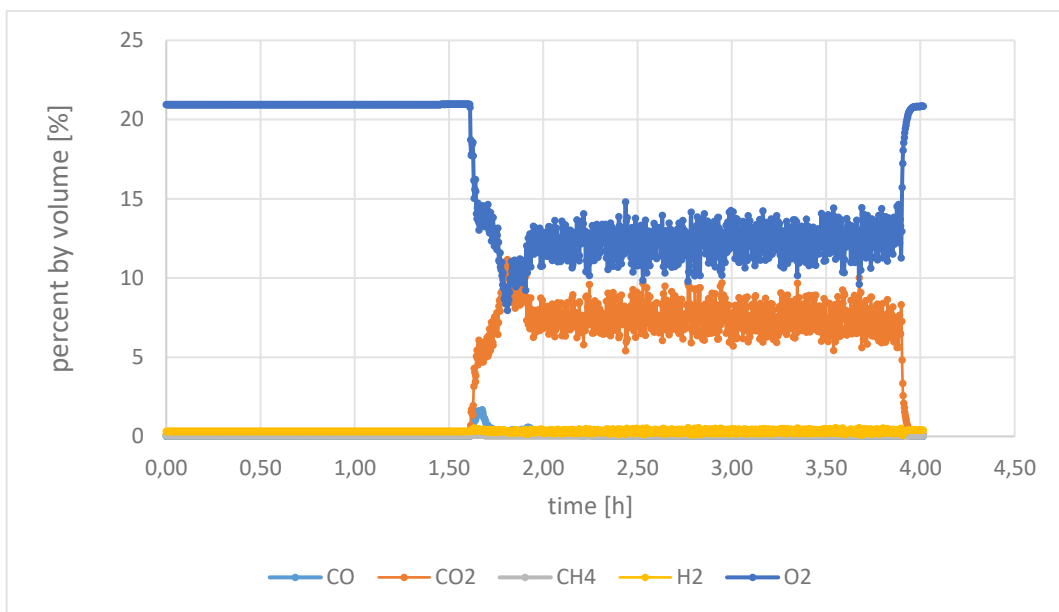


Figure 19: Gas composition of experiment 2

Chapter 3

Results and discussion

3.1. Experiment 1

Bottom ash

Fragmentation of the former cylindrically shaped pellets can be registered in the bottom ash from all experiments. In experiment 1 with only sewage sludge pellets as fuel, the ash particles could be separated from the bed material for the most part. The pellets were mostly fragmented to sizes larger than the bed material. This makes analysing the probes easier because of less dilution of the bed material. The molar percentage of the elements is almost the same as in the fuel except for Cl and S shares which are significantly lower.

Table 15: Molar percentage of elements in the bottom ash of experiment 1

mol%	Na	Mg	Al	Si	P	S	Cl	K	Ca	Ti	Fe
Fuel	2.1	3.1	11.2	20.5	18.7	7.6	0.5	2.0	13.6	1.8	19.0
Bottom ash	2.0	3.2	12.1	17.6	22.2	0.9	0.0	2.0	16.1	2.2	21.8

The mappings in the SEM analysis give a broad overview of the distribution of elements. Low concentration, but equal distribution of Cl, Mg, Na, Ti and S can be perceived. Al, Ca, K, P and Si appear in similar areas of the specimen. Fe seems to be more broadly distributed. Regarding concentration, Fe and P show the greatest molar percentage followed by Si then Ca and Al.

In Figure 20 and Figure 21, the difference between bed material and ash particles becomes evident when looking at the Si concentration. At the bottom of the figure, a bed material particle with high Si concentration can be seen.

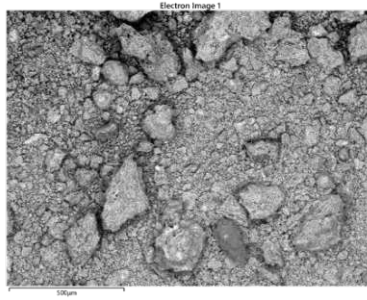


Figure 20: SEM image 1, bottom ash, experiment 1

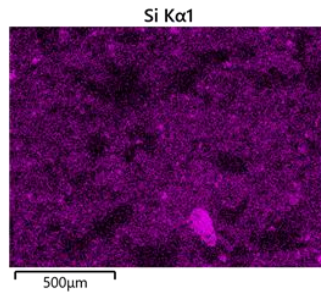


Figure 21: SEM mapping of Si in SEM image 1

In another SEM image the mapping of only a few larger particles was performed. A large percentage of Ca can be seen. It is approximately the same as the Si percentage and more than the Al percentage. At the bright spot in Figure 22, a high concentration of Fe can be seen when taking Figure 23 into account. A few spots of high Si concentration can be registered in Figure 23.

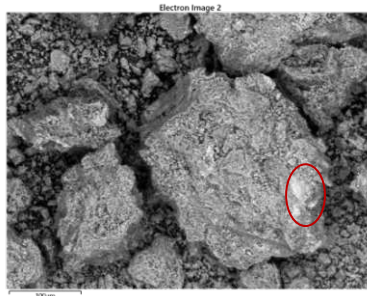


Figure 22: SEM image 2, bottom ash, experiment 1

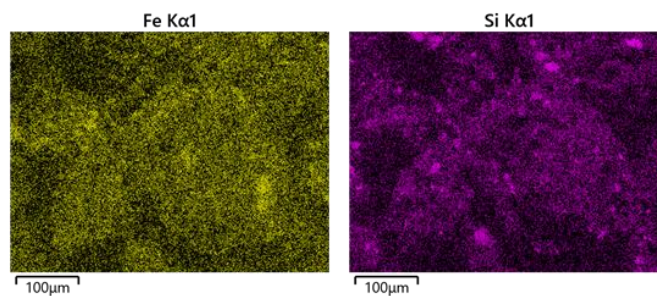


Figure 23: SEM mapping of SEM image 2: Fe (left) and Si (right)

Low concentrations of Cl and S in the bottom ash compared to the concentration in the fuel indicate high volatility of these elements and their molecules. This observation is coherent with expectations based on the literature concerning other forms of combustion. Sulphur tends to form volatile compounds such as H_2S , COS , CS_2 and thiophenic compounds [25]. In a study concerning the volatilisation of trace elements for coal – sewage sludge blends during their combustion, it was determined that the high Cl contents of the sludge can produce a pronounced effect on the volatilisation of some trace elements (Ag, Cd, Cs, Cu, Li, Pb, Rb and Tl). The formation of volatile chlorides is probable [26]. It is expected to find a higher share of S and Cl in the cyclone or filter ash.

As the elements Al, Ca, K, P and Si appear in similar areas of the specimen, it is not possible to gain enough information about the molecules and chemical compounds formed by them. Considering the occurrence and the concentration of Ca, Al and Si, it is estimated that feldspar is formed. Fe correlates positively with P which is the case with the fuel as well as with the bottom ash. This leads to the assumption that Fe does not yet precipitate to a great extent at 800 °C. At a higher temperature, it shows an increased tendency to leave the original constellation and precipitate to the surface. High concentrations of Fe can be observed at the surface as research of single pellets has shown [27].

The bright spot in Figure 22 indicates a high concentration of heavy elements, meaning elements with high molar mass. Taking the mapping of Fe into account, high concentrations of iron can be observed at that spot. This leads to the assumption of precipitation of Fe in this particle and a negative correlation of Fe regarding other elements. This is in correlation with other studies on single pellet combustion [27]. It is assumed that some parts of the bed material are included in the ash particles during the combustion process because of high Si concentration in particular areas of the ash particles. This can be confirmed by the light microscope image of the bottom ash in Figure 24.



Figure 24: bottom ash experiment 1, inclusion of bed material particles

Cyclone ash

An average Si concentration of approximately 50% can be perceived in the SEM image 3 (Figure 25). The mappings of phosphorous and iron show similar spots of high intensity and therefore high concentrations of these elements. The mapping of Ca also correlates with the mapping of P.

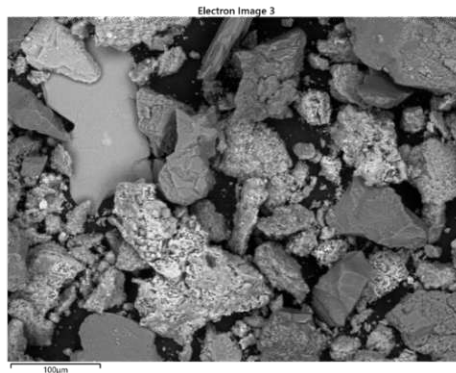


Figure 25: SEM image 3 of cyclone ash, experiment 1

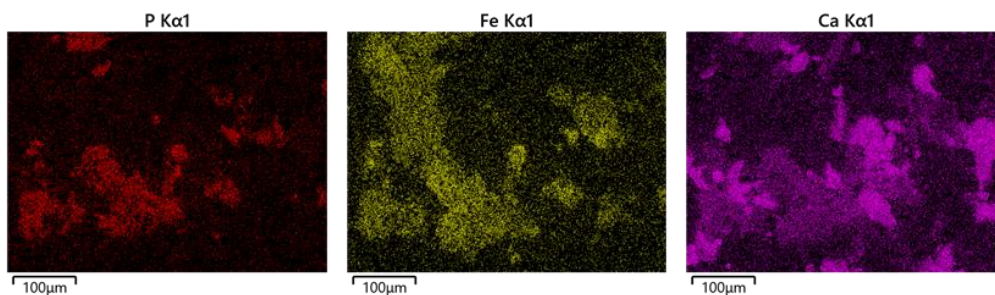


Figure 26: SEM mappings of SEM image 3 (cyclone ash, experiment 1) P(left), Fe (middle) and Ca (right)

The average concentration of Ca in the cyclone ash with 18.8 mol% is high compared to the original composition (13.6 mol%). P and Fe show very low concentration (7 mol% and 8.3 mol%) in comparison to the original composition (18.7 mol% and 19 mol%). There is almost no S and Mg in the cyclone ash and Al concentration is slightly lower (8.4 mol%) than originally (11.2 mol%).

The same effect can be observed in the SEM image 6 (Figure 27). High concentrations of Ca and Fe appear in the same areas as high concentrations of P as seen in Figure 28. Na and K concentrations are very low in those areas (Figure 29).

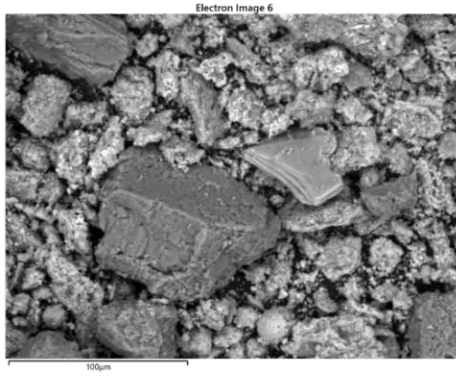


Figure 27: SEM image 6, cyclone ash, experiment 1

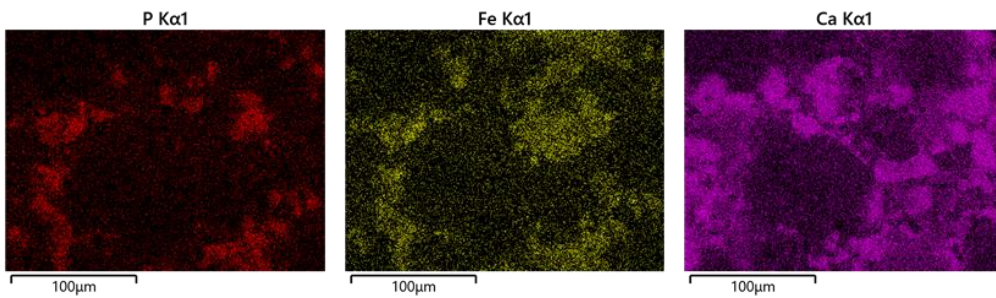


Figure 28: SEM mappings of SEM image 6: P (left), Fe (middle) and Ca (right)

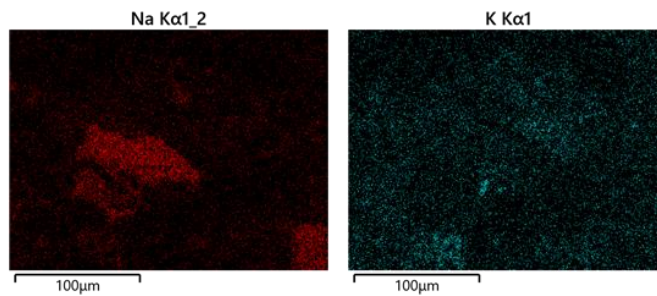


Figure 29: SEM mappings of SEM image 6: Na (left) and K (right)

The Si concentration in the SEM mappings of the cyclone ash is very high at about 50%. The cyclone ash is highly diluted with bed material which can be seen in the light microscope image in Figure 30.



Figure 30: Light microscope image of cyclone ash, experiment 1

This dilution with bed material also becomes evident in the SEM image (Figure 31) when taking the Si and O concentration into account in the mappings. Great intensity of light colours correlates with high concentration.

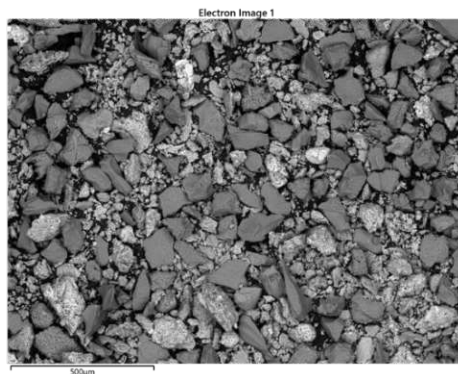


Figure 31: SEM image of cyclone ash, experiment 1

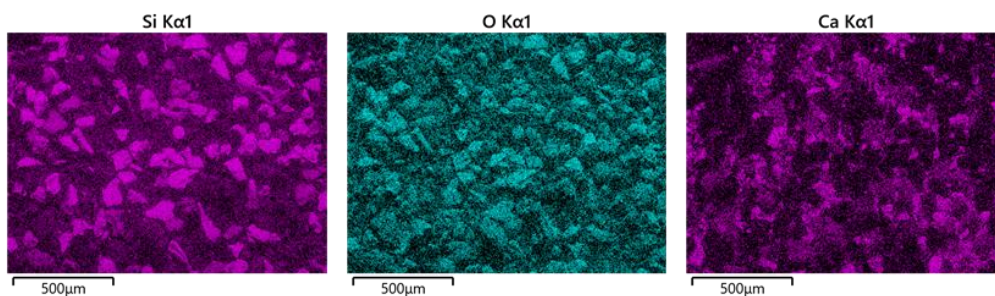


Figure 32: SEM mappings of SEM image 1 (cyclone ash, experiment1) Si (left), O (middle) and Ca (right)

This dilution of the ash occurs because of the fragmentation of ash during the process to a size similar to that of bed material particles. To separate the fractions, a separation by density would have to be performed. Alternatively, the size of bed material particles would have to be altered. This was not carried out but would be evident for further analysis and exact results. The concentration of the elements in the ash and the fuel are not comparable without taking the dilution with bed material into account. Hence lower P and Fe concentrations in the ash do not automatically mean that the elements were lost. It is reasonable to look at the ratios rather than the exact percentages in this case.

When looking at the results in Figure 26 and Figure 28, a correlation between P and the elements Fe and Ca can be observed. It is assumed that P forms compounds with these elements. Ca-P-compounds are considered to be very stable configurations and are poorly accessible for plants [28]. A study by Kalbasi and Karthikeyan demonstrates the negative impact of Al and Fe treated manure on the plant availability if P in the soil [28], [29].

Low concentrations of K in the same areas as P leads to the assumption of fewer K-P-compounds. This was already expected because of the low K share in the fuel. K-P-compounds are less stable than Ca-P-compounds [28]. This facilitates plant availability. In co-combustion with agricultural residues such as sunflower husk and wheat straw, it is sought to achieve the formation of more bio-available compounds as K-phosphates. Almost no Na in the regions of high P concentration gives evidence for the lack of Na bearing phosphates.

Filter ash

SEM mappings of the filter ash show an even distribution of the elements and in the SEM mapping of Si a few spots of high Si concentration were detected (Figure 34). A significant concentration of S and Cl in the filter ash can be seen in Figure 35.

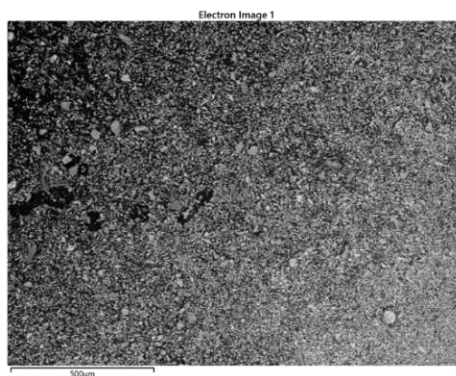


Figure 33: SEM image 1, filter ash, experiment 1

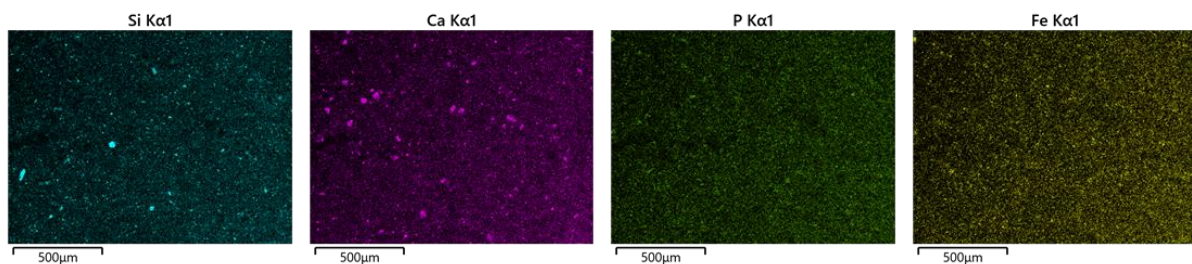


Figure 34: SEM mappings of Figure 33: Si (left), Ca (2nd from left), P (3rd from left) and Fe (right)

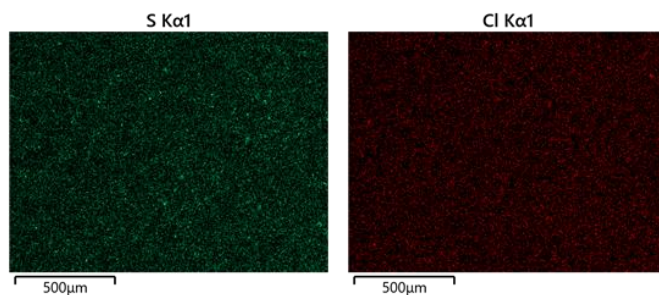


Figure 35: SEM mappings of Figure 33: SEM image 1, filter ash, experiment 1: S (left) and Cl (right)

The images correlate well with the overall molar percentage of the elements in the ash (Table 16). The ratios are similar to the original fuel, except for a highly raised Ca and a slightly raised Na share. Compared to the other ash fractions, a significant amount of S and Cl are found in the filter ash.

Table 16: molar percentage of elements in the filter ash and the fuel

mol%	Na	Mg	Al	Si	P	S	Cl	K	Ca	Ti	Fe
Fuel	2.1	3.1	11.2	20.5	18.7	7.6	0.5	2.0	13.6	1.8	19.0
Filter ash	3.1	3.1	12.4	21.7	16.6	4.3	0.3	2.0	20.2	1.5	15.1

In Figure 37, correlations between Fe and P can be detected more easily than between Ca and P. When focussing on areas of high Ca concentration and high P concentration, they overlap less.

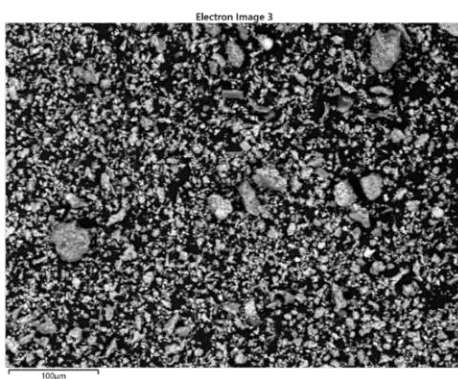


Figure 36: SEM image 3, filter ash, experiment 1

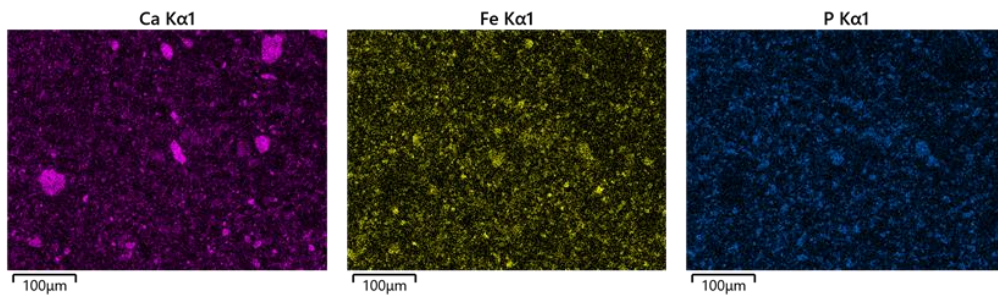


Figure 37: SEM mapping of Figure 36: Ca (left), Fe (middle) and P (right)

Dilution with bed material can also be detected in the filter ash because of spots of high Si and O concentration that don't show concentrations of other elements. It is not as severe as in the cyclone ash which simplifies analysis. As elements are evenly distributed in the ash fragments and concentrations of elements are similar to those in the fuel, it has been concluded that the migration and sedimentation of elements did not take place on a great scale. No sintering or exclusion phenomena can be observed.

The concentrations of S and Cl are significantly higher than in the bottom of the cyclone ash as was expected. This confirms the assumption of Si and Cl forming volatile compounds and solidifying at lower temperatures in the filter.

In the filter ash it is more evident that P is present in configurations with Fe, as it is also in the fuel rather than in case of Ca which would be the more stable configuration. This is not expected when taking thermochemical equilibrium into account. Kinetics play a big role in solid-solid reactions and atom/molecule mobility. In a different study at higher temperatures more mobility was observed and therefore formation of other compounds could be seen [27].

3.2. Experiment 2

Bottom ash

Dilution of the ash fractions with bed material can be perceived in the second experiment in a similar way as in the first experiment (Figure 39). All elements are evenly distributed over the ash fraction (Figure 39 and Figure 40). Estimated from the mappings, P appears in the same spots as Al, Ca and K.

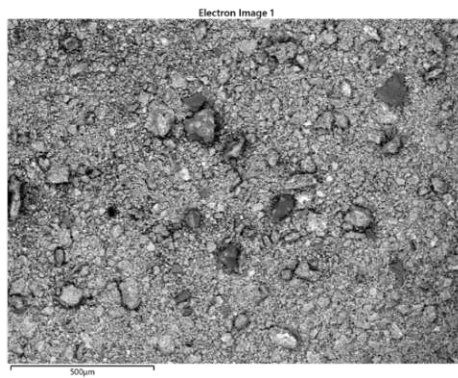


Figure 38: SEM image 1, bottom ash, experiment 2

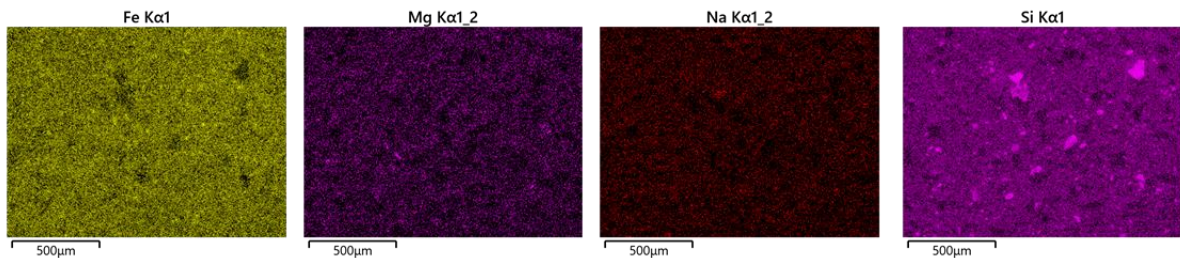


Figure 39: SEM mappings of Figure 38 : Fe (left), Mg (2nd from left), Na (3rd from left) and Si (right)

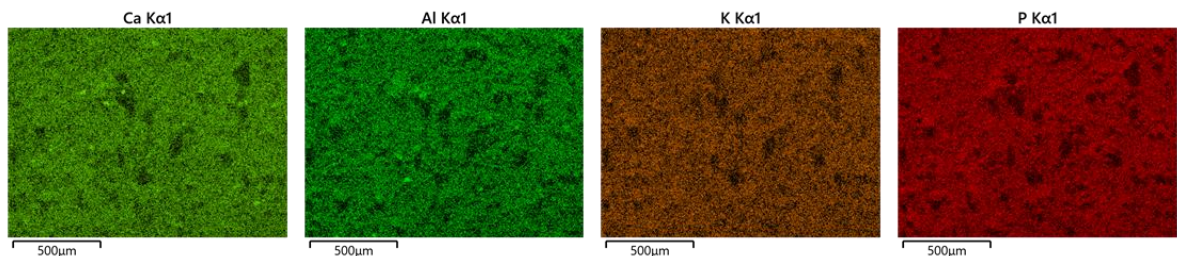


Figure 40: SEM mappings of Figure 38 : Ca (left), Al (2nd from left), K (3rd from left) and P (right)

As shown in Table 17 the concentration of K is higher than in the first experiment with an average of 8.1 mol% (2 mol% in experiment one). Compared to the K concentration of the fuel (15.9 mol%) it is

significantly lower. As well as in experiment 1, Mg and S shares are very low in comparison to the original composition. The molar percentage of Al, Fe and P are higher than in the fuel. The Si concentration is slightly raised.

Table 17: average mol percentage of elements in bottom ash, experiment 2

mol.%	Na	Mg	Al	Si	P	S	Cl	K	Ca	Ti	Fe
Fuel	1.4	7.7	7.3	14.6	14.1	8.0	1.1	15.9	16.0	1.3	12.7
Bottom ash	2.9	3.1	10.6	18.2	20.1	0.6	0.0	8.1	14.8	1.9	19.9

Light spots in the SEM image are represented in the SEM mapping of Fe as spots of high intensity and therefore of high Fe concentration.

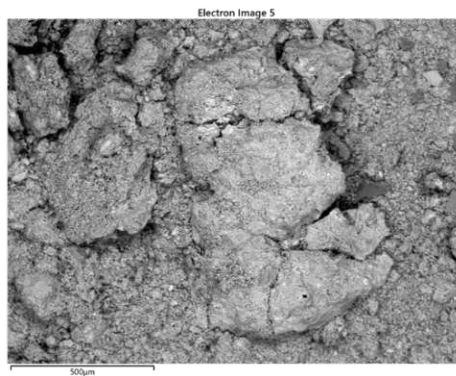


Figure 41: SEM image 5, bottom ash, experiment 2

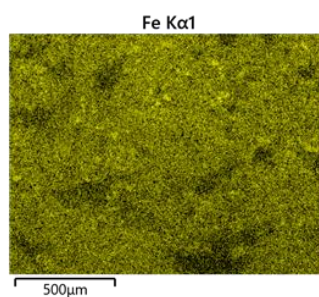


Figure 42: SEM mapping of Figure 41: Fe

Dilution of the bottom ash with quartz particles as bed material leads to highly negative Si-P correlations. Observation in the areas of high P concentration in the mappings support the assumption that few P-Si compounds are formed. In other studies the formation of phospho-silicates in the melt was documented at temperatures around 1200°C – 1400°C [27]. This was not the case at

the operation temperature of these experiments. The even distribution of K over the ash gives reason to assume that interaction between the sewage sludge particles and the sunflower husk particles took place. As blending of the two fractions was to be achieved, these results give a positive indications for future application of co-combustion. The aim to acquire K-bearing (e.g., KMgPO_4 , $\text{CaK}_2\text{P}_2\text{O}_7$ or CaKPO_4) and therefore more bio-accessible compounds seems to have been partly accomplished. In areas of high K concentration Mg and Ca concentration are also raised.

As Fe/Al – phosphates can be formed too, the fate of Fe in the ash is also of interest. In experiment 2 a few areas of precipitated Fe-atoms were detected on the surface. When looking at a particular ash particle light spots can be detected in the SEM image (Figure 41). A correlation between these spots and spots of high intensity in the SEM mapping of Fe gives reason to assume the precipitation on Fe to the surface. This hampers the formation of Fe-phosphates.

Cyclone ash

The SEM image 2 and the light microscope image of the cyclone ash in experiment 2 show a great variety of particles. A lot of particles are of high Si and O concentration (Figure 44).

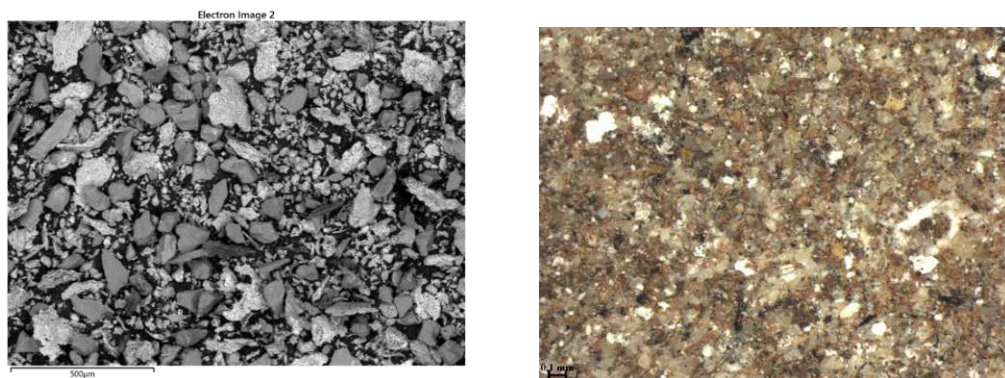


Figure 43: SEM image 2 and light microscope image, cyclone ash, experiment 2

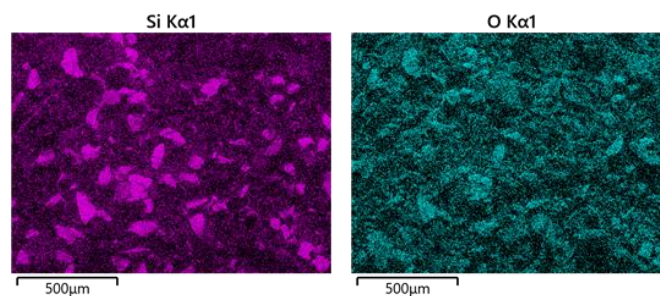


Figure 44: SEM mappings of Figure 43: Si (left) and O (right)

In comparison to experiment 1, the S concentration in the cyclone ash is significantly higher in experiment 2 (1.9 mol% and 4.5 mol%). The circled area in Figure 45 shows high concentration of Ca, P, K, Mg and S. Fe is also present in these areas. In the squared area P concentration is high, correlating predominantly with Ca, K and Fe.

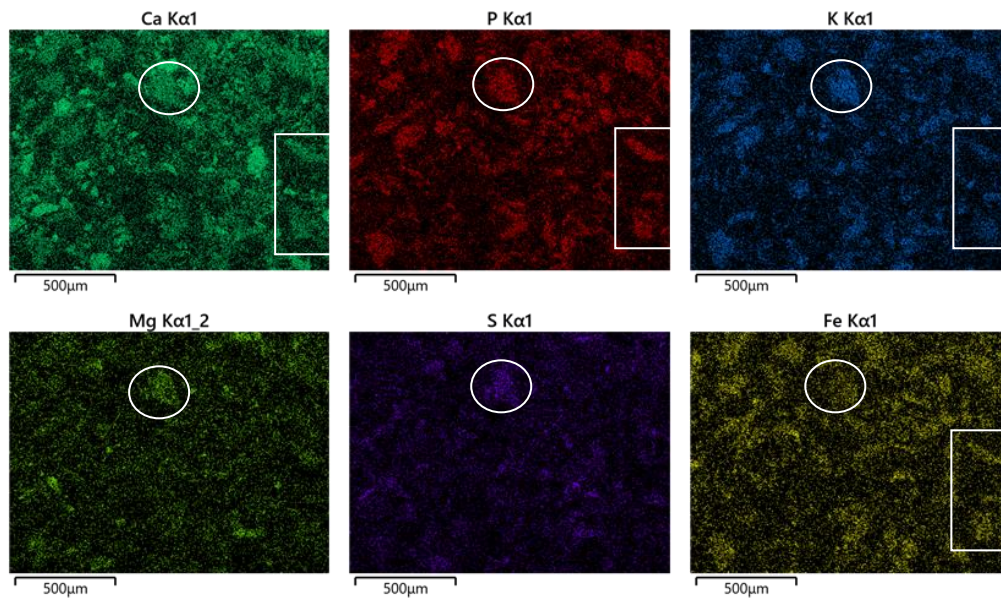


Figure 45: SEM mappings of Figure 43: Ca (above, left), P (above, middle), K (above, right), Mg (below, left), S (below, middle) and Fe (below, right)

Table 18: Average molar percentage of elements in cyclone ash, experiment 2

mol%	Na	Mg	Al	Si	P	S	Cl	K	Ca	Ti	Fe
Fuel	1.4	7.7	7.3	14.6	14.1	8.0	1.1	15.9	16.0	1.3	12.7
Cyclone ash	1.9	5.2	7.5	35.7	9.1	4.5	0.5	6.6	19.6	0.9	8.8

There are many areas of high P concentration correlating with Ca, K and Fe. Mg is rather low with an average concentration of 5.2 mol%. In the SEM image 5 some sulphide is also visible. High Ca and S concentrations can be observed in the same spot (Figure 46). The Fe mapping shows high Fe concentration in the light spots of the SEM image 5.

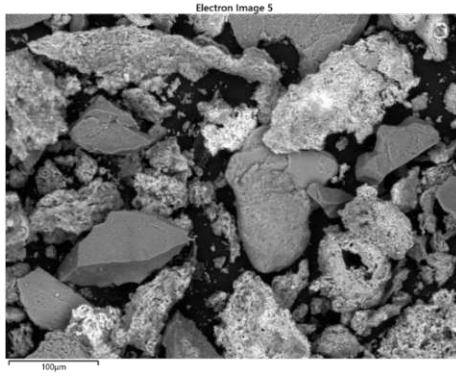


Figure 46: SEM image 5, cyclone ash, experiment 2

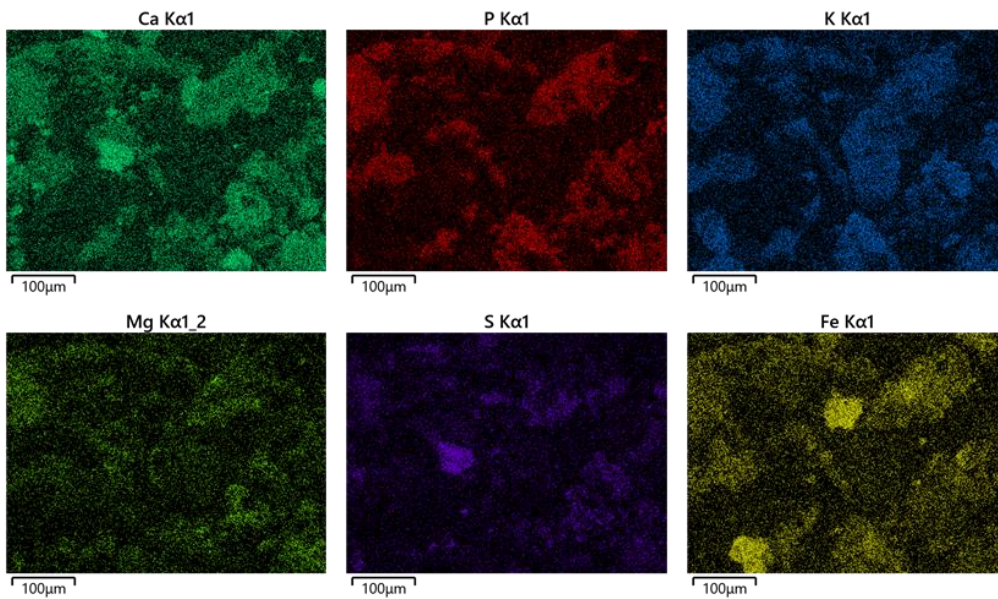


Figure 47: SEM mappings of Figure 46: Ca (above, left), P (above, middle), K (above, right), Mg (below, left), S (below, middle) and Fe (below, right)

Regarding other compounds that are formed, Figure 47 gives rather unambiguous data about Si, Al and K. They appear in high concentrations in the same particle, where there's a noticeable lack of all other elements.

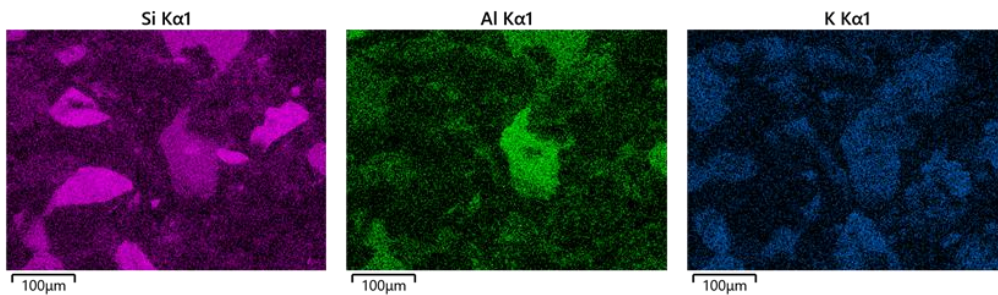


Figure 48: SEM mappings of Figure 46: Si (left), Al (middle) and K (right)

A dilution of cyclone ash is visible in the same way as in experiment one. The quartz particles can be observed in the light microscope and the SEM images, and mainly make up for the high Si concentration. It was previously described that S concentrations are comparatively high. S seemed to have formed fewer volatile compounds. In a few images areas of sulphates that are normally not that stable can be observed. With only sewage sludge as fuel, S only occurred in the filter ash because of forming highly volatile products. The co-combustion with sunflower husk seems to have a great effect on the formation of more stable sulphates.

With regard to the phosphates formed, the correlation of P with Ca, K and Fe leads to the assumption that $\text{CaK}_2\text{P}_2\text{O}_7$ or CaKPO_4 are formed rather than KMgPO_4 . The Mg concentration is comparatively small. Fe-phosphates are present, but some migration of Fe to the surface could also be detected in Figure 46. The phenomenon has already been described. Not only quartz particles, phosphates and sulphates can be observed, but also feldspar particles. In Figure 48 the main elements of feldspar Si, Al and K are predominant. No other elements are present in significant amounts.

Filter ash

The elements seem to be equally distributed (Figure 49 and Figure 50).

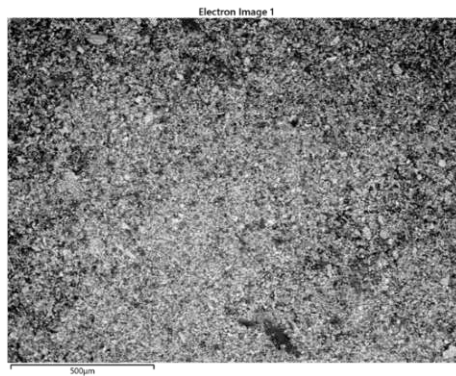


Figure 49: SEM image 1, filter ash, experiment 2

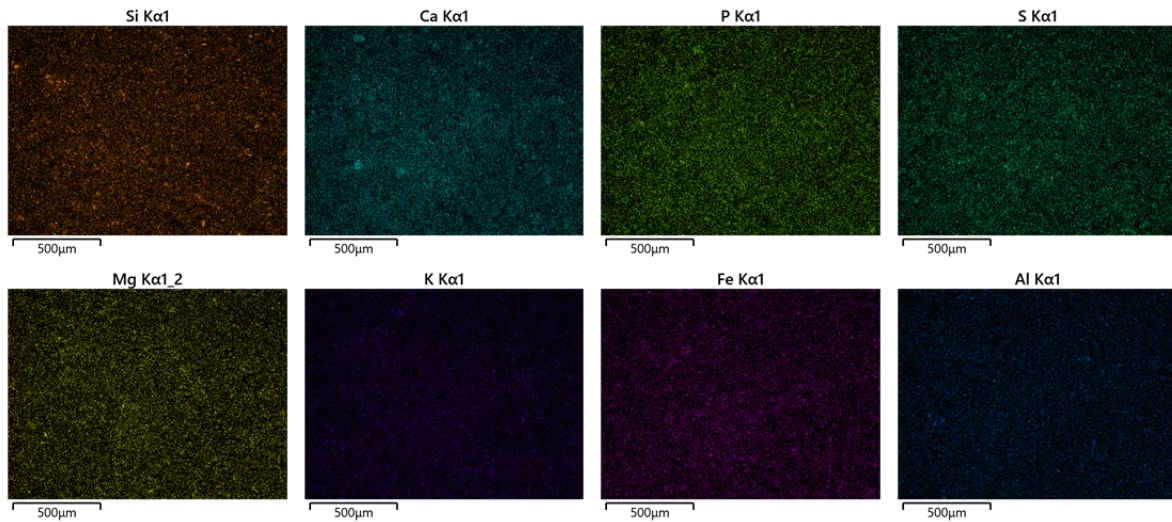


Figure 50: SEM mappings of Figure 71: Si (above, left), Ca (above, 2nd from left), P (above, 3rd from left), S (above, right), Mg (below, left), K (below, 2nd from left) Fe (below, 3rd from left) and Al (below, right)

The Si concentration in the filter ash is only slightly raised to the original concentration in the fuel. The S content is greater in the filter ash (10.2 mol%) than in the fuel (8 mol%), and the Mg share shows significantly higher concentrations in the filter ash (11.9 mol%) than in the fuel itself (7.7 mol%). The filter ash fraction bears only 5.6 mol% of K in comparison to an original concentration of 15.9 mol%.

Table 19: Average molar percentage of elements in filter ash, experiment 2

mol%	Na	Mg	Al	Si	P	S	Cl	K	Ca	Ti	Fe
Fuel	1.4	7.7	7.3	14.6	14.1	8.0	1.1	15.9	16.0	1.3	12.7
Filter ash	2.1	11.9	7.1	15.0	12.7	10.2	0.7	5.6	24.6	0.9	9.5

In a greater magnification, the areas of high phosphorous concentration correlate with areas of high Fe and Ca concentration. The K concentration is low throughout the specimen, and it is not possible to make a statement about correlation with P. In some areas of high K concentration, Si and Al concentrations are also raised.

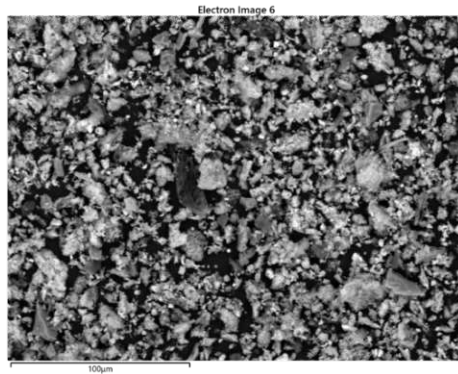


Figure 51: SEM image 6, filter ash, experiment 2

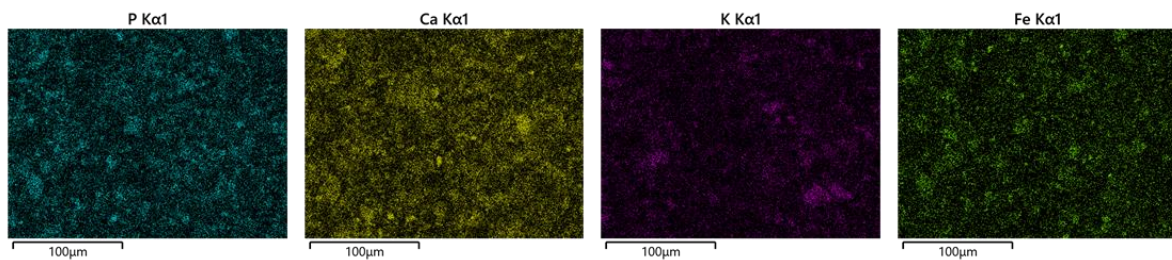


Figure 52: SEM mappings of Figure 51: P(left), Ca (2nd from left), K (3rd from left) and Fe (right)

Equal distribution of elements is a sign for good blending. Sewage sludge and sunflower husk particles seem to have formed compounds throughout the particle boundaries. The filter ash is less diluted with bed material than the cyclone ash which can be observed in the lower Si concentration. Though it is still higher than fuel concentration some quartz particles are also present in this fraction. As K bearing phosphates are of interest in this study, the cyclone ash seems more promising than the filter ash of fuel 2.

The presence of particular elements in cyclone and ash fraction stands out in Table 20. Not surprisingly, the S content is notably higher in the filter ash than in the cyclone ash. Volatile compounds solidify at lower temperatures. The gas cools down on the way to the chimney and already has a lower temperature in the filter. The same could apply for Mg. Its share is substantially raised in the filter ash. In Table 20 the molar concentration of distinct probes of cyclone and filter ash are demonstrated. It is notable that S, K and Mg have very different shares in the ashes. More

sulphates have formed in the filter ash while more K bearing phosphates with Mg content have formed in the cyclone ash.

Table 20: Molar percentages of each element in SEM image 2, cyclone ash, experiment 2 (left) and in SEM image 1, filter ash, experiment 2 (right)

ELEMENT	MOLAR FRACTION (%)	ELEMENT	MOLAR FRACTION (%)
Si	33.2	Ca	24.8
Ca	20.5	Si	14.7
P	9.9	P	12.6
Fe	9.2	Mg	11.9
Al	7.1	S	10.3
K	7.1	Fe	9.4
Mg	5.3	Al	7.1
S	4.5	K	5.6
Na	1.9	Na	2.1
Ti	0.9	Ti	0.9
Cl	0.5	Cl	0.7

All ash fractions show a lower K content than the original fuel. It is suspected that K-carbonates are formed which may be volatilized at higher temperatures. Equilibrium calculations suggest that the Si-lean SH ash tends to form volatile K compounds. As SS and WS-rich ashes contain a high level of anionic compounds such as PO_4^{3-} and SiO_4^{4-} which may create solid K compounds, the volatilization does not occur to the same extent as in SH-rich ashes [16]. The formation of volatile KCl should also be considered, as KCl is a common product in biomass processes [30]. This correlates with observations in this study of lower Cl concentrations in all ash fractions compared to the Cl concentration in the fuel.

3.3. Experiment 3

Bottom ash

The bottom ash of experiment 3 contains a large amount of Si. A significant number of the particles shown in Figure 54 show a high concentration of Si-oxide. This correlates with the overall molar percentages of the probe in Table 22. High Al concentration in Si-rich regions can be observed.

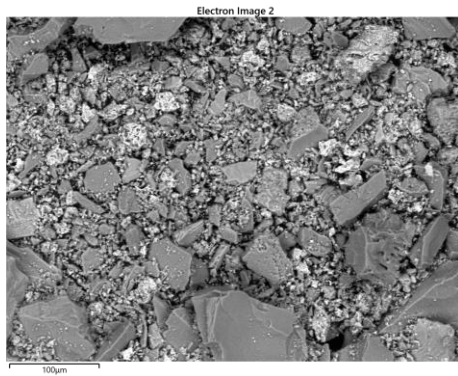


Figure 53: SEM image 2, experiment 3, bottom ash

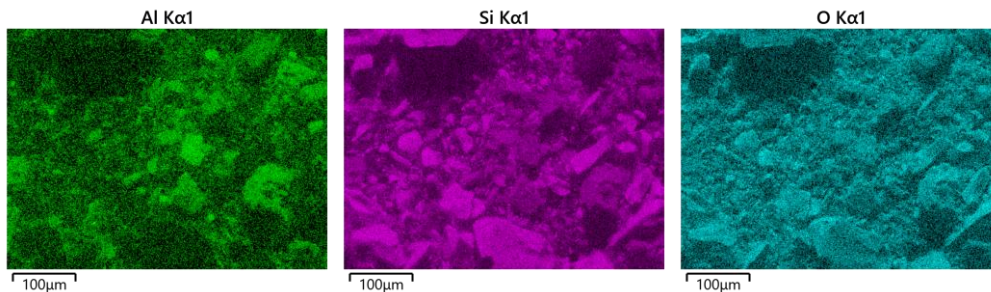


Figure 54: SEM mappings of Figure 53: Al (left) and Si (middle) and O (right)

The ash particles show a similar distribution of the elements Ca, Fe, K, P, Mg, Na and S in the mappings. While there is a large amount of potassium in the bottom ash, Mg, Na and S percentages appear comparatively low.

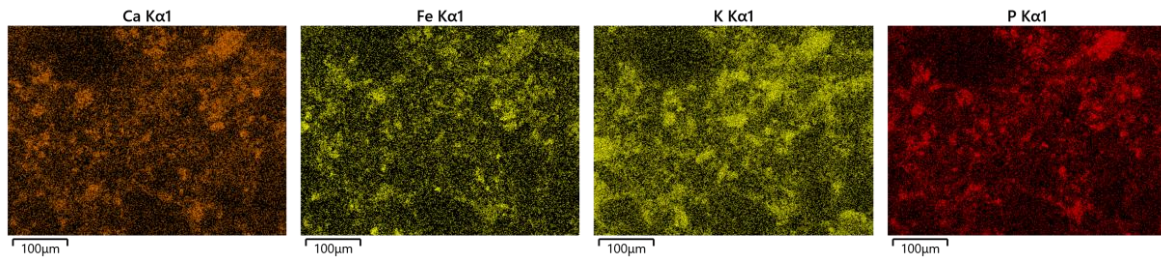


Figure 55: SEM mappings of Figure 79: Ca (left) and Fe (2nd from left), K (3rd from left) and P (right)

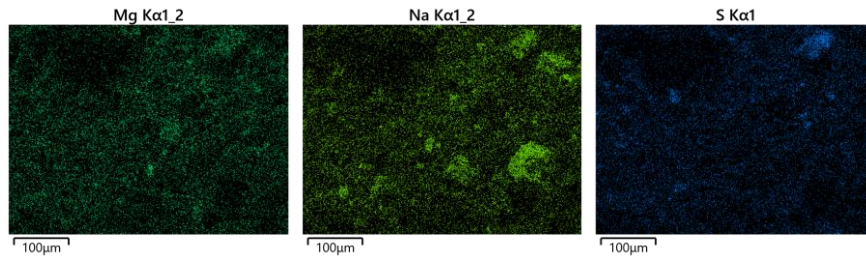


Figure 56: SEM mappings of Figure 79: Mg (left) and Na (middle) and S (right)

A large percentage of potassium and aluminium can be observed in the bottom ash of experiment 3. P correlates positively with K, Fe, Ca, and Al. Areas of high P and K concentrations also show raised Ca concentrations. The circled particles in Figure 59 consist of P, Fe and Ca according to the mappings, while the regions marked with the white squares are of higher Al and K concentrations.

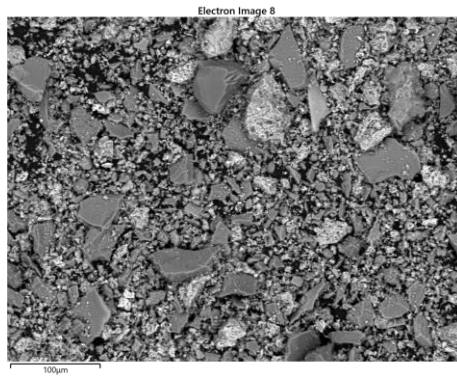


Figure 57: SEM image 8, experiment 3, bottom ash

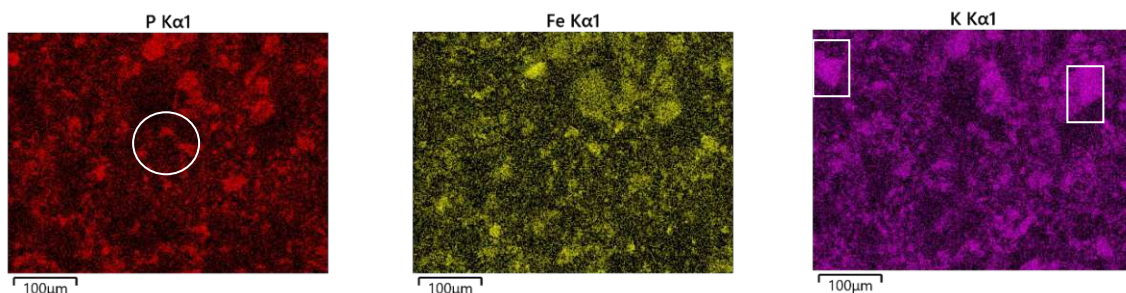


Figure 58: SEM mappings of Figure 57: P (left), Fe (middle) and K (right)

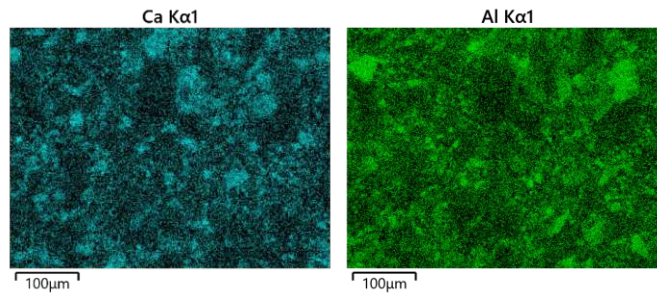


Figure 59: SEM mappings of Figure 57: Ca (left) and Al (right)

The dominance of K and Al in the bottom ash of experiment three is also displayed in Table 21 with 8 mol% and 7.7 mol%. The amount of K is notably higher than in the bottom ash of experiment 1 (2 mol%).

Table 21: Molar concentrations of the elements in SEM image 8

ELEMENT	MOLAR FRACTION (%)
Si	59.1
P	8.1
K	8.0
Al	7.7
Fe	7.0
Ca	5.5
Na	2.3
Mg	1.0
S	0.7
Ti	0.7
Cl	0.0

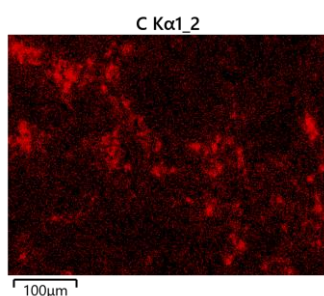


Figure 60: SEM mappings of Figure 57: C

Table 22: average molar percentage of elements in bottom ash, experiment 3

mol%	Na	Mg	Al	Si	P	S	Cl	K	Ca	Ti	Fe
Fuel	1.0	3.5	5.1	34.8	9.3	4.6	4.7	17.1	11.1	0.8	8.1
Bottom ash	2.0	0.8	7.4	63.3	6.8	0.6	0.0	7.7	4.6	0.6	6.2

Areas of significant C concentrations become apparent in the mapping of carbon in the bottom ash in Figure 60. The composition of the fuel clearly influences the composition of the ash fractions. The Ca share is predominant in the cyclone ash fraction. Fuel 3 has high K, Si and Cl concentrations. High dilution with bed material is also notable in this ash fraction. Si and O make up a large percentage of the elements present. The Si concentration amounts to almost 60 mol% in SEM image 8. The correlation between Si and Al leads to the belief that Si-Al-oxides were formed during combustion. As K, Ca, Fe and P seem evenly distributed over the ash particles, it is assumed that mixed phosphates were formed. The mappings show raised K shares in P-rich fractions. It is possible to gain $\text{CaK}_2\text{P}_2\text{O}_7$ or CaKPO_4 . Fe bearing phosphates seem to have prevailed during combustion, as Fe did not precipitate to the surface. Low Mg concentration in the fuel (3.1 mol%) leads to few Mg bearing phosphates such as KMgPO_4 . This is also displayed by the marginal amount of Mg in the mapping (Figure 56) with an average concentration of 3.2 mol% throughout the bottom ash.

Areas of high Al and K shares as indicated in Figure 58 and Figure 59 suggest the formation of feldspar. The correlation between P and Ca is higher than between P and K which can be seen in Figure 58, but the average K concentration of 7.7 mol% is higher than the average Ca concentration with 4.6 mol%. These results are to be interpreted with the Si dilution in mind. Nevertheless, it is noteworthy that the Al share in the bottom ash is greater than in the fuel while the P, K and Ca shares are significantly lower. It is assumed that the high Si share in fuel 3 leads to the formation of Al/K silicates. This assumption is backed by the high amount of Al in the bottom ash.

Interestingly, some particles seem to have been left unburned. The carbon concentration is comparatively high in some areas of the bottom ash. This gives cause to adapt the combustion parameters and procedure.

Cyclone ash

The cyclone ash of experiment 3 is inhomogeneous as seen under the light microscope in Figure 61 and in the following SEM mappings. The ash is highly diluted with bed material.



Figure 61: light microscope image cyclone ash, experiment 3

In comparison to the previously discussed bottom ash, some elements are present in significantly greater amounts in the cyclone ash. The Mg share is slightly raised in the cyclone ash (3.7 mol%) compared to the concentration in the fuel (3.5 mol%) and notably higher than in the bottom ash (0.8 mol%). Calcium is predominant in this fraction with 14.4 mol% compared to 11.1 mol% in the fuel and only 4.6 mol% in the bottom ash. All these values are to be considered comparatively as the dilution with bed material makes quantification difficult.

Aluminium and iron are less present in this ash fraction. Whereas Al is dominant in the bottom ash with 7.4 mol%, it shows only 3.1 mol% in the cyclone ash fraction. Iron suffers a similar fate with 6.2 mol% in the bottom ash and 3.8 mol% in the cyclone ash. Sulfur and chloride show an enhanced presence in the cyclone ash fraction.

Table 23: Average molar percentage of elements in cyclone ash, experiment 3

mol%	Na	Mg	Al	Si	P	S	Cl	K	Ca	Ti	Fe
Fuel	1.0	3.5	5.1	34.8	9.3	4.6	4.7	17.1	11.1	0.8	8.1
Cyclone ash	1.5	3.7	3.1	56.0	6.1	2.8	1.3	7.0	14.4	0.4	3.8

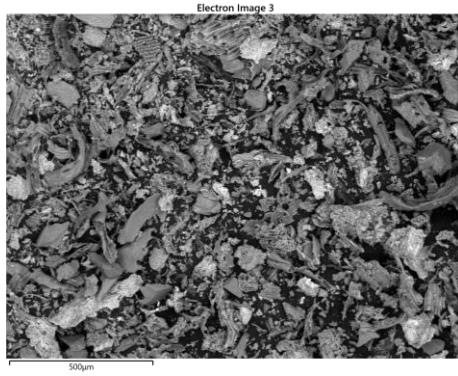


Figure 62: SEM image 3, experiment 3, cyclone ash

Figure 63 gives data about possible correlations. In P-rich areas Ca, K and Fe are clearly present. Potassium is evenly distributed over the ash fraction.

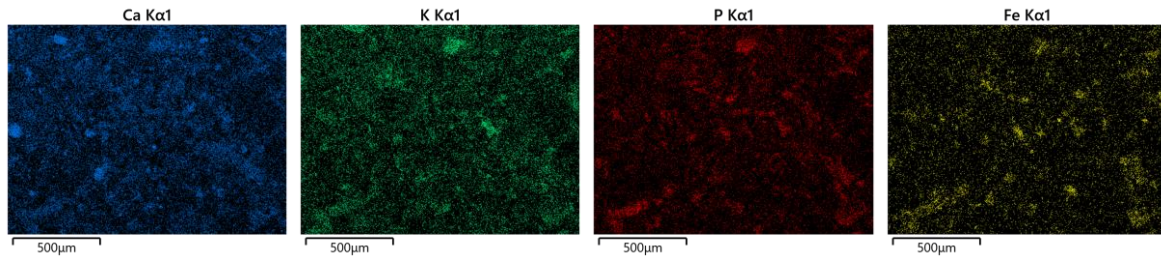


Figure 63: SEM mappings of Figure 62: Ca (left), K (2nd from left), P (3rd from left) and Fe (right)

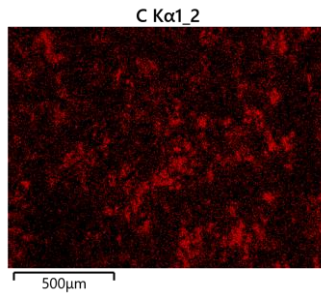


Figure 64: SEM mappings of Figure 88: C

The mapping of carbon in SEM image 3 shows the remaining C in the cyclone ash. The dilution of the cyclone ash with bed material becomes evident in Figure 65. Some particles show high Al and O concentrations or high Al, Si and O concentrations.

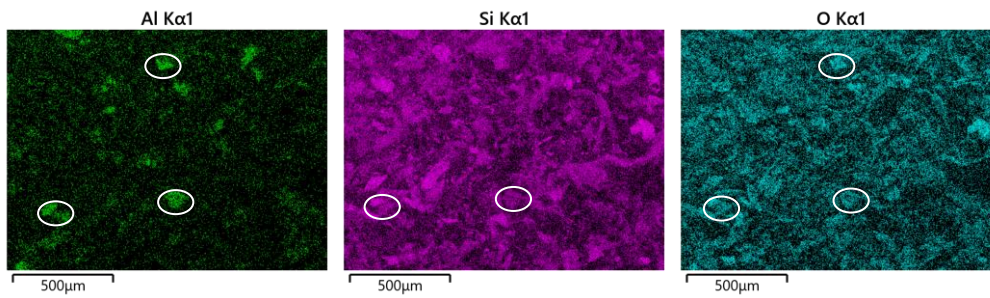


Figure 65: SEM mappings of Figure 88: Al (left), Si (middle) and O (right)

There is more sulphur and magnesium in the cyclone ash than in the bottom ash with 3.7 mol% and 2.8 mol% respectively.

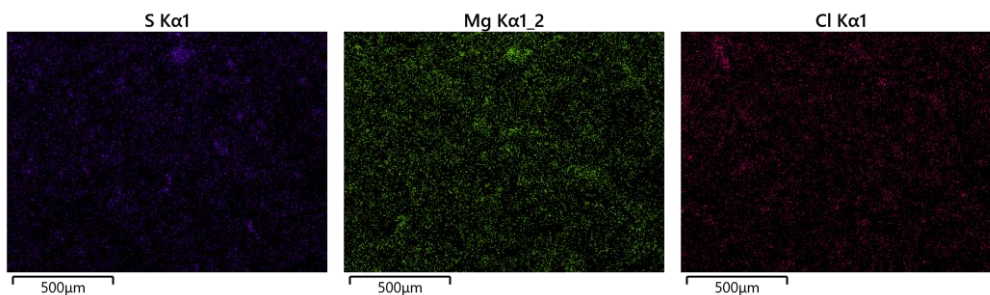


Figure 66: SEM mappings of Figure 88: S (left), Mg (middle) and Cl (right)

Whereas the original Mg concentration in fuel 3 is comparatively low, its share in the cyclone ash is greater than in the bottom or filter ash. The formation of Mg bearing phosphates such as KMgPO_4 is to be expected. The cyclone ash fraction seems to be rich in Ca-bearing phosphates because of the previously described prominent Ca concentration of 14.4 mol% and the positive P-Ca correlation. As Ca-phosphates are in general more stable and less bio-available, these compounds are not favoured for further use in fertilizers [28]. In the bottom ash fraction of this experiment, there is a notable Al share (7.4 mol%) that is expected to have formed Al-silicates. In the cyclone ash there is a significantly lower concentration of 3.1 mol%. The Si share is also lower than in the bottom ash. This also provides evidence of fewer aluminium-silicates being formed although the dilution of bed material needs to be considered. The lower Fe share gives reason to assume a less significant presence of iron-phosphates in the cyclone ash.

As expected, more volatile compounds such as sulphates and chlorides are found in the cyclone ash. This phenomenon was previously described in experiments 1 and 2. With higher K and Cl shares in the fuel, it is assumed that KCl is formed. This is in accordance with the mappings in Figure 63 and

Figure 66. The even distribution of K over the ash fraction indicates good blending of sewage sludge and wheat straw particles.

Filter ash

The filter ash in experiment 3 seems to be less diluted with bed material than the other fraction when taking the Si share into consideration. It only amounts to 42.4 mol% in comparison to 31.3 mol% in the bottom and 56 mol% in the cyclone ash.

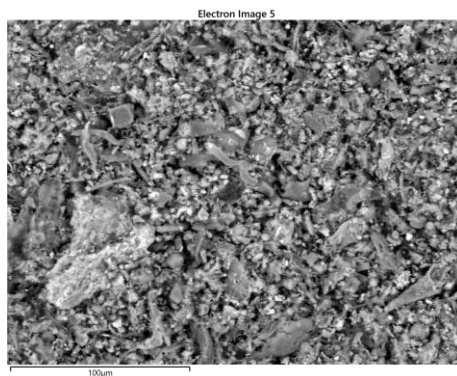


Figure 67: SEM image 5, experiment 3, filter ash

Some shares of elements are more dominant than others. High concentrations of Na, Al, S and K can be found in the ash (Table 24). The Na share of 4.5 mol% is the highest Na share in all the fractions. Sulphur makes up 4.1 mol% of the filter ash compared to only 0.6 mol% of the bottom ash and 2.8 mol% of the cyclone ash. The K concentration is with 18.2 mol% significantly greater than in the other ash fractions with 7-8 mol%. Not only are the concentrations of K and S raised, but they also correlate with P, as their mappings show a high intensity in similar spots (Figure 68). A positive correlation between P and Fe can be observed.

Table 24: average molar percentage of elements in the filter ash, experiment 3

mol%	Na	Mg	Al	Si	P	S	Cl	K	Ca	Ti	Fe
Fuel	1.0	3.5	5.1	34.8	9.3	4.6	4.7	17.1	11.1	0.8	8.1
Filter ash	4.5	2.5	8.3	42.4	7.2	4.1	0.4	18.2	5.6	1.7	5.4

The Ca share is comparatively low (5.6 mol%), but the element is equally distributed over the ash as seen in the mapping in Figure 68.

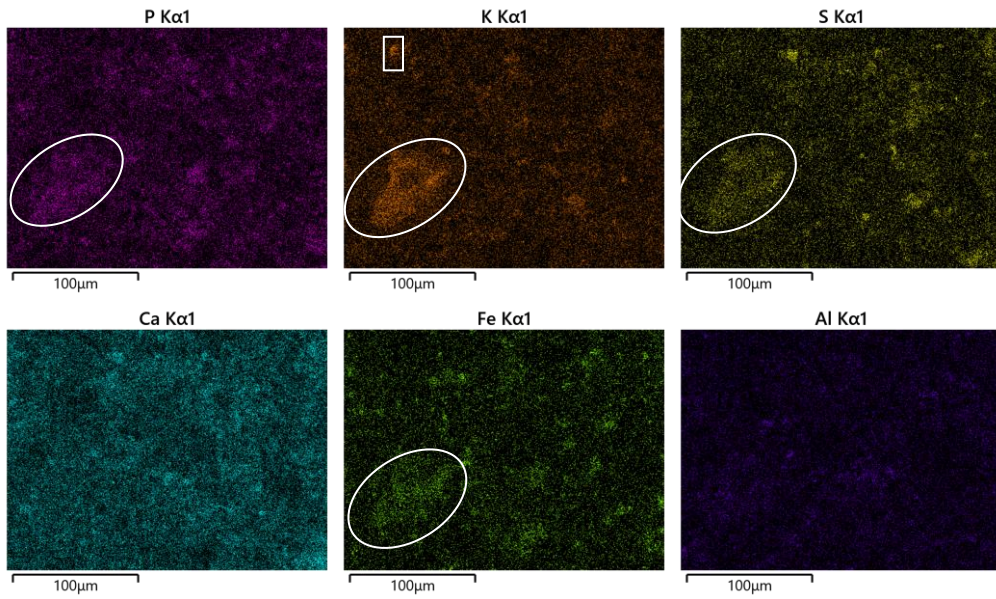


Figure 68: SEM mappings of Figure 67: P (above, left), K (above, middle), S (above, right), Ca (below, left), Fe (below, middle) and Al (below, right)

The concentration of chloride is rather low compared to the original concentration in the fuel (0.4 mol% to 4.7 mol%). Some particles of the ash show high K and high Cl concentrations.

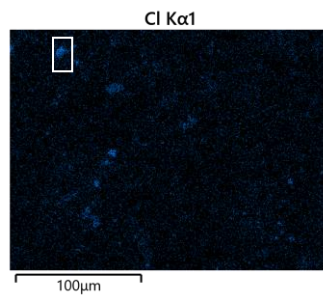


Figure 69: SEM mapping of Figure 67: SEM image 5, experiment 3, filter ash: Cl

In another SEM image spots of higher P share also show higher concentrations of Ca, Al and Fe. The correlation between P and K does not seem to be significant.

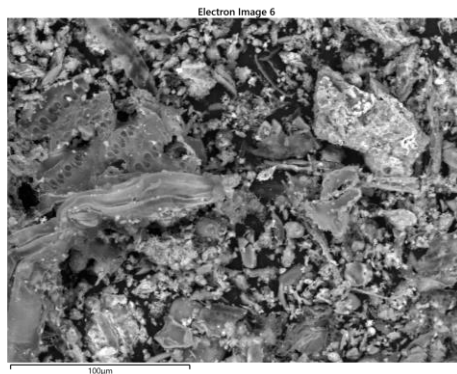


Figure 70: SEM image 6, experiment 3, filter ash

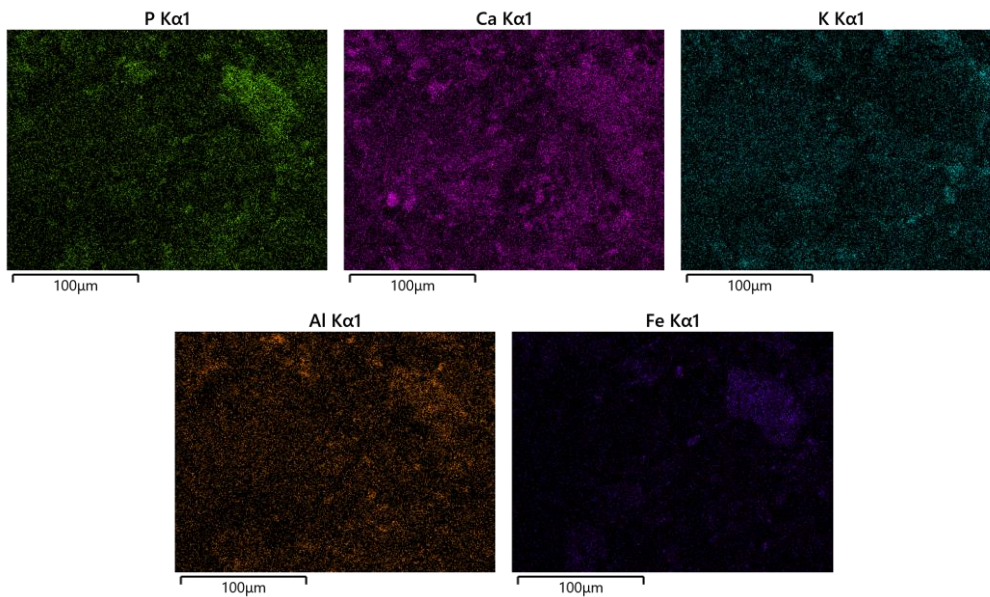


Figure 71: SEM mappings of Figure 70: P (above, left), Ca (above, middle), K (above, right), Al (below, left) and Fe (below, middle)

It is expected that different forms of sulphates are to be gained in this ash fraction. The raised S share and the correlations in the SEM mappings give reason for this assumption. Furthermore, higher K ratios suggest more K bearing phosphates and less Ca bearing phosphates. Iron bearing phosphates seem to exist in the ash as well as in the original fuel. K and Cl show some congruence in the mappings which leads to the assumption of KCl being formed.

The SEM mappings differ from each other. There are some deviations in the ash. In SEM mapping 6 of the filter ash, P seems to correlate more with Ca than with K which suggests more Ca bearing phosphates. It is assumed that different phosphates were formed, and it would be necessary to perform further analysis in order to distinguish between them.

3.4. Experiment 4

Bottom ash

The results of the gasification of fuel 1 do not diverge greatly from the results of the combustion of fuel 1. The shares of the elements are very similar to those under combustion conditions. Only the sulphur share is slightly raised at 1.4 mol% compared to 0.9 mol% in experiment 1.

Table 25: Average molar percentage of elements in the bottom ash, experiment 4

mol%	Na	Mg	Al	Si	P	S	Cl	K	Ca	Ti	Fe
Fuel	2.1	3.1	11.2	20.5	18.7	7.6	0.5	2.0	13.6	1.8	19.0
Bottom ash	2.0	3.1	12.6	18.4	22.2	1.4	0.0	2.1	16.4	2.3	19.7

Some ash particles show phosphorous correlating positively with Al, Ca, Mg and S as seen in the circled areas in Figure 73. The K share in P-rich regions seems to be less pronounced. The percentage over the ash is with 2.1 mol% very similar to the original concentration in the fuel.

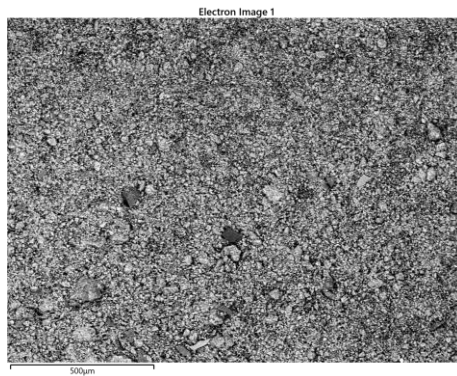


Figure 72: SEM image 1, experiment 4, bottom ash

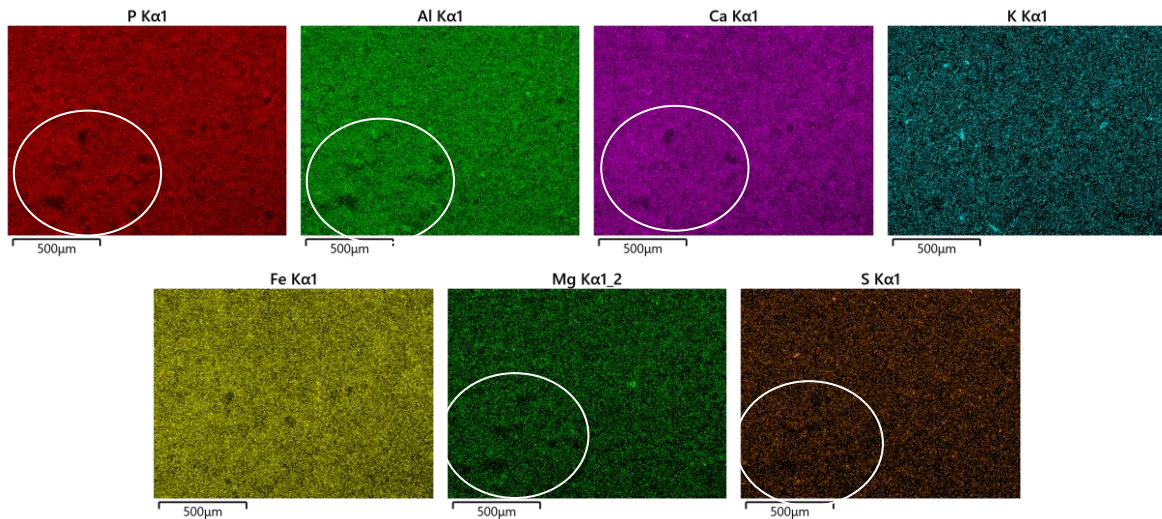


Figure 73: SEM mappings of Figure 72: P (above, left), Al (above, 2nd from left), Ca (above, 3rd from left), K (above, right), Fe (below, left), Mg (below, middle) and S (below, right)

The integrity of the bottom ash was maintained for the most part, but the ash did undergo fragmentation as seen in Figure 74. Compared to the bottom ash in experiment 1, the ash of experiment 4 is of a darker colour and shows less inclusion of bed material particles.



Figure 74: Light microscope image of the bottom ash in experiment 4 (left) and experiment 1 (right)

Gasification conditions seem to change very little with regard to the element composition in the process. The ash is a different colour and appears to be more fragmented, but the element shares give the impression that they depend more on the fuel composition than on the operational conditions. The concentration of Si is significantly lower than in experiment 1 which could be attributed to less bed material inclusion. This is favourable for further use of the ash.

Higher Sulphur concentration gives reason to assume the formation of more sulphates than under combustion conditions. The thermodynamical conditions seem to have an impact there.

Nevertheless, the sulphur share is still notably lower than in the original fuel (1.4 mol% to 7.6 mol%). It is assumed that sulphur as well as Chloride form volatile compounds that are emitted with the exhaust gas. Due to low K concentrations in fuel 1, the K share in the ash is also low. Furthermore few P-K correlations could be determined. Therefore, fewer K-bearing phosphates appear to have formed. Results lead to the assumption that Mg/Ca-bearing phosphates or Al-bearing phosphates are formed.

Cyclone ash

The cyclone ash obtained under gasification conditions shows a different composition than the cyclone ash under combustion conditions. There is less dilution with bed material and therefore lower Si concentration with 33.5 mol% compared to 49.5 mol% in the cyclone ash of experiment 1. The phosphorous share is significantly higher than in experiment 1 (12.2 mol% to 7 mol%). Mg, S, K and Fe are more pronounced in this cyclone ash fraction. The iron share in particular is with 13.1 mol% much higher than the iron share of experiment 1 with 8.3 mol%. K is more pronounced even compared to the original share in the fuel. The sulphur concentration in the cyclone ash is 3.2 mol% and therefore notably higher than the 1.9 mol% share of S in the cyclone ash under combustion conditions.



Figure 75: Light microscope image, experiment 4, cyclone ash

Table 26: average molar percentage of elements in the cyclone ash, experiment 4

mol%	Na	Mg	Al	Si	P	S	Cl	K	Ca	Ti	Fe
Fuel	2.1	3.1	11.2	20.5	18.7	7.6	0.5	2.0	13.6	1.8	19.0
Cyclone ash	1.8	2.8	8.7	33.5	12.2	3.2	0.9	3.0	19.6	1.3	13.1

The Si concentration of the cyclone ash is significantly higher than in the fuel and higher than in the bottom ash. This phenomenon has already been described for experiment 1. This can further be confirmed in the SEM image 2 and its Si and O mappings.

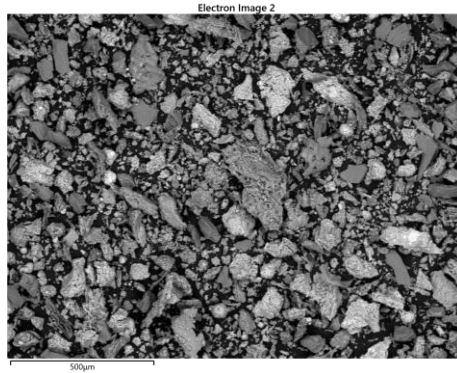


Figure 76: SEM image 2, experiment 4, cyclone ash

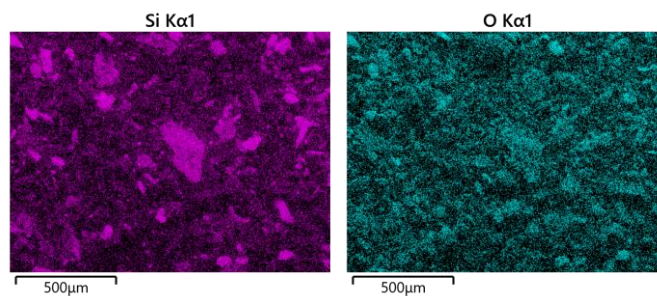


Figure 77: SEM mappings of Figure 76: Si (left) and O (right)

Mappings of SEM image 2 provide a good overview of possible correlations especially between P and Fe. Ca and Al show a higher intensity in similar regions. K correlates more positively with Si than with P. It is not possible to specify the prevailing elements in the S-rich regions.

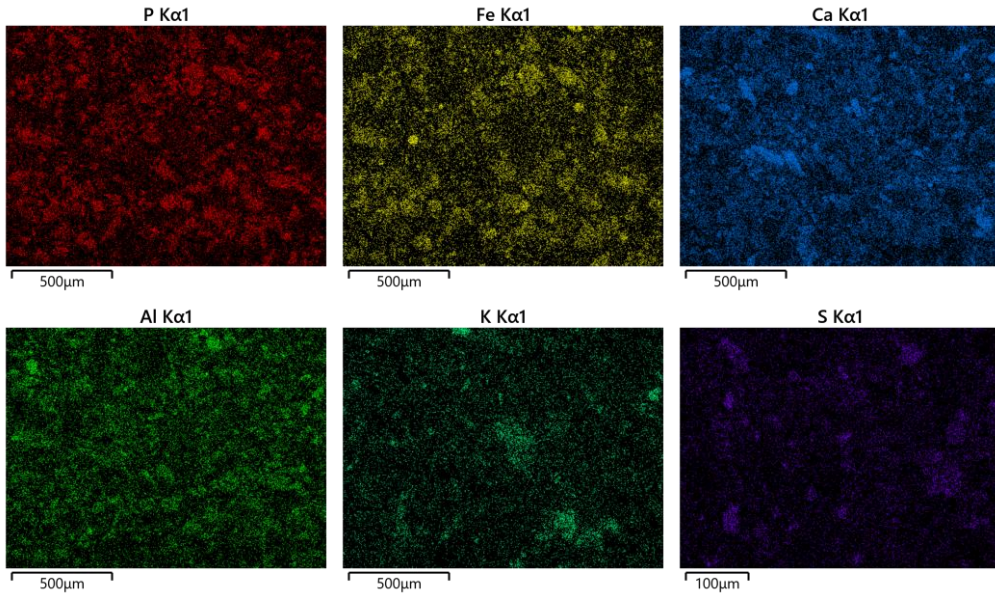


Figure 78: SEM mappings of Figure 76: P (above, left), Fe (above, middle), Ca (above, right), Al (below, left) and K (below, right)

In another SEM image (SEM image 6) bed material inclusions can be observed. As mentioned for the previous SEM image, correlations between P and Fe can be detected here as well (Figure 80). A lot of Ca is present, but not specifically enhanced in P-rich areas.

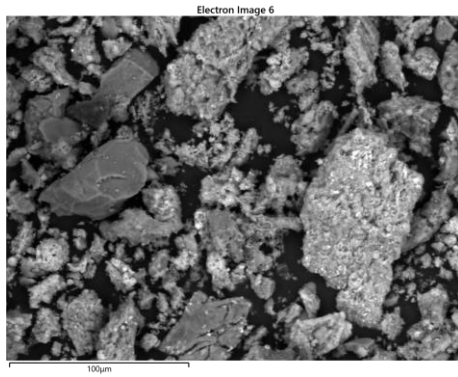


Figure 79: SEM image 6, experiment 4, cyclone ash

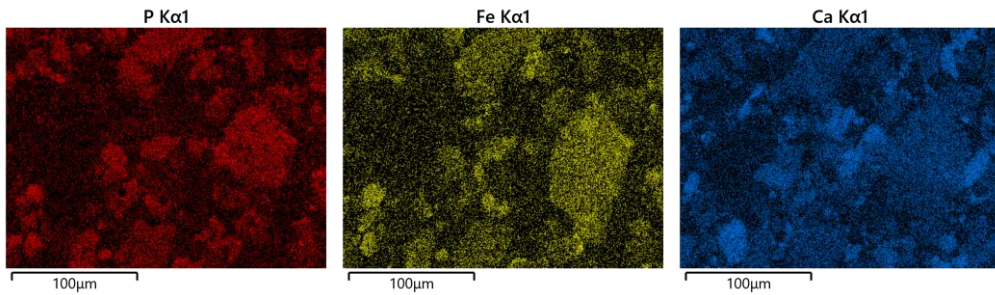


Figure 80: SEM mappings of Figure 79: P (left), Fe (middle) and Ca (right)

Thermal conditions appear to have great influence on the composition of the cyclone ash. Corresponding to a study of melt behaviour of the ashes [16], Al/Fe phosphates seem to be more pronounced under gasification conditions. In these experiments the Al and Fe shares are significantly raised compared to those under combustion conditions. The Ca concentration is very similar. The study revealed a similar effect on sewage sludge fuel as seen in Figure 81.

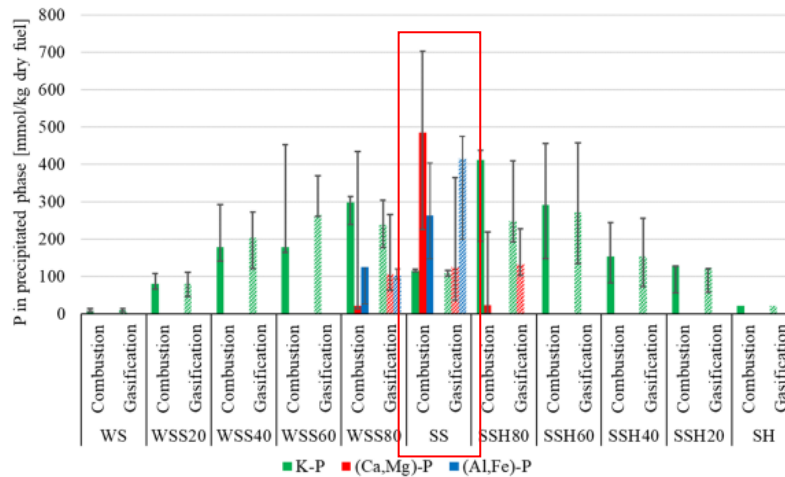


Figure 81: P share in precipitated phase, melt study with different fuels [16]

In the same study the effect of heat on the shift from Ca bearing phosphates to K bearing phosphates was investigated. At higher temperatures, a more K bearing phosphates could be determined. This shift cannot be confirmed for this ash. On the one hand, the K concentration is higher than in the fuel, but on the other hand the mappings show the presence of K in other regions than P. It appears that gasification conditions favour the formation of sulphates.

Filter ash

The filter ash composition under gasification conditions is similar to the filter ash composition in the case of combustion. There is more chloride, more potassium and less aluminium to be found in experiment 4 than in experiment 1. High S and Cl concentrations in comparison to other ash fractions are of note. The Si dilution of the probe is less than in the cyclone ash with only slightly raised Si concentration (21.9 %) with regard to the original concentration with 20.5 mol%. The Ca share is raised (20.1 mol%) compared to 13.6 mol% in the fuel. The results in the case of combustion show similar values.

Table 27: Average molar percentage of elements in the filter ash, experiment 4

mol%	Na	Mg	Al	Si	P	S	Cl	K	Ca	Ti	Fe
Fuel	2.1	3.1	11.2	20.5	18.7	7.6	0.5	2.0	13.6	1.8	19.0
Filter ash	2.1	3.6	10.5	21.9	16.2	4.3	1.4	2.7	20.1	1.6	16.0

The dilution of the filter ash with bed material can be registered in Figure 82 and Figure 83. Spots of high Si and O concentrations are clearly visible. P-rich regions show also higher concentrations of Ca, Al, and Fe. Iron-oxide can be seen in the circled area. K is to be found not only in phosphates but also in silicates as seen in the squared area.

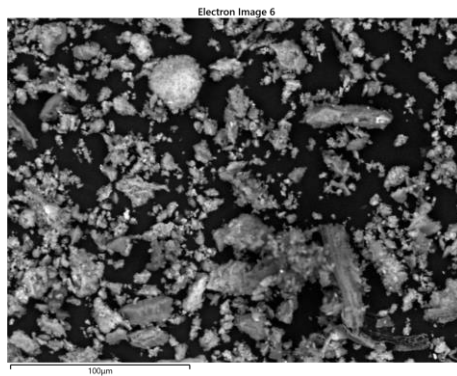


Figure 82: SEM image 6, experiment 4, filter ash

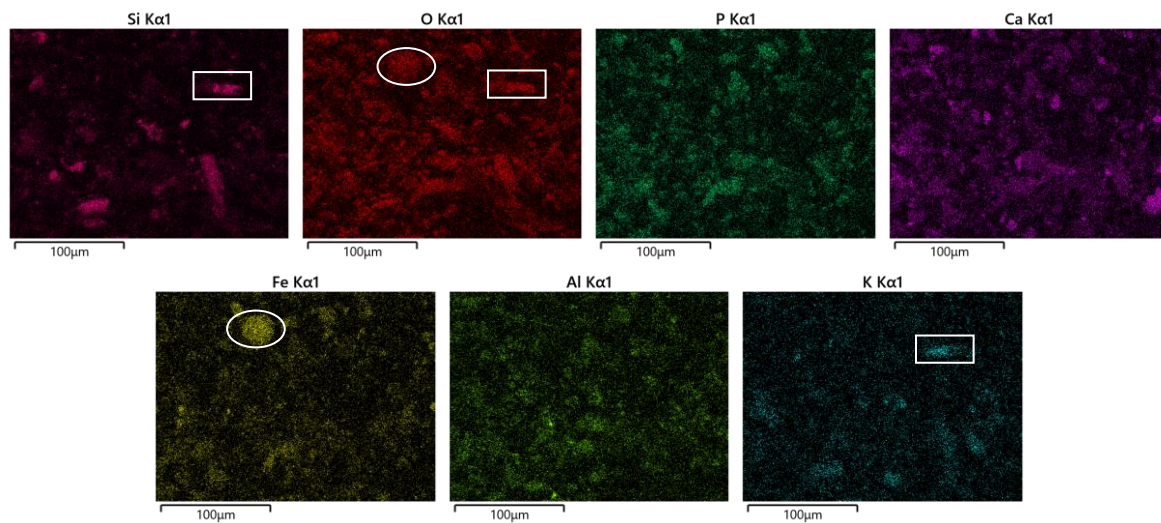


Figure 83: SEM mappings of Figure 82: Si (above, left), O (above, 2nd from left), P (above, 3rd from left), Ca (above, right), Fe (below, left), Al (below, middle) K (below, right)

Mg and S concentrations are comparatively high. In some areas there is a large amount of both elements present e.g., the marked area in Figure 84. A positive correlation of S and Ca was also detected.

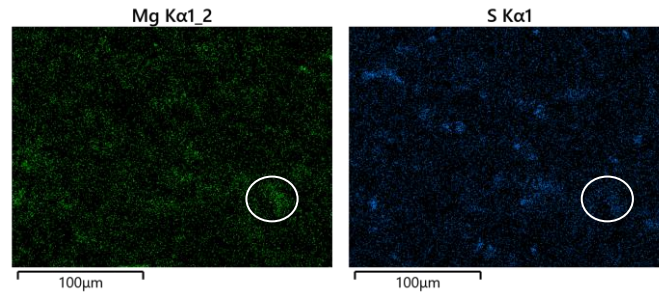


Figure 84: SEM mappings of Figure 85: Mg (below, left) and S (below, right)

The difference in process conditions has only a small effect on the filter ash composition for fuel 1. Nevertheless, more volatile chloride components which solidified in the filter seem to have formed. The potassium content is also raised which leads to the assumption that KCl has been formed. Fe shows a lower tendency for accumulation and positive Fe-P correlation could be determined in Figure 83. This indicates a state of non-equilibrium as the Fe precipitation and formation of K-phosphates would be expected, based on thermochemical studies [16]. The raised Ca content gives reason to assume the retention of Ca bearing phosphates and less conversion to K bearing phosphates. The most positive correlation in the ashes was obtained in the case of Si-Al-K compounds. This was also illustrated in Figure 83. Due to high S concentrations, it is assumed that different sulphates were formed. Ca and Mg show correlations with S.

3.5. Experiment 5

Bottom ash

Because of the strong dilution with bed material, the comparison between the combustion and the gasification conditions in the runs using fuel 2 proved difficult. Some ratios can be contrasted with each other. The K to Ca ratio in experiment 5 is, at 1.6 significantly higher than that in experiment 2 at only 0.5. In this ash fraction the Al concentration is higher than the Fe concentration whereas in experiment 2 it is the other way around. The Fe/P ratio is approximately the same in both experiments (around 1), but the Al/P ratio is very different. In experiment 2 under combustion conditions, the Al/P ratio is only 0.53 and the ratio in experiment 5 amounts to 2.28.

Table 28: Average molar percentage of elements in the bottom ash, experiment 5

mol%	Na	Mg	Al	Si	P	S	Cl	K	Ca	Ti	Fe
Fuel	1.4	7.7	7.3	14.6	14.1	8.0	1.1	15.9	16.0	1.3	12.7
Bottom ash	1.5	0.5	9.6	72.4	4.2	0.4	0.0	4.4	2.7	0.4	3.8

There was very little bottom ash to be obtained in experiment 5. The high degree of dilution with bed material can be seen in the light microscope image in Figure 85. Bed material and ash particles could not be separated easily. Hence there is a large percentage of Si in the results.



Figure 85: light microscope image, experiment 5, bottom ash

The dilution is illustrated in Figure 87 with high concentrations of Si and O in the bed material particles. The ash particles seem to be even smaller than the bed material particles which are about 0.2 mm in diameter.

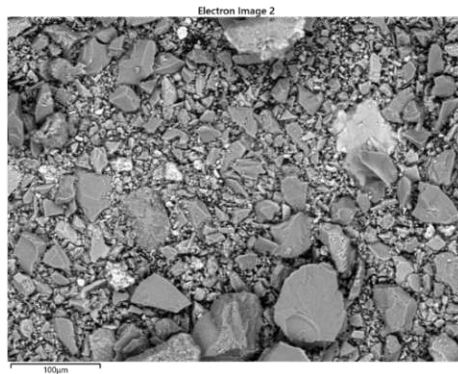


Figure 86: SEM image 2, experiment 4, bottom ash

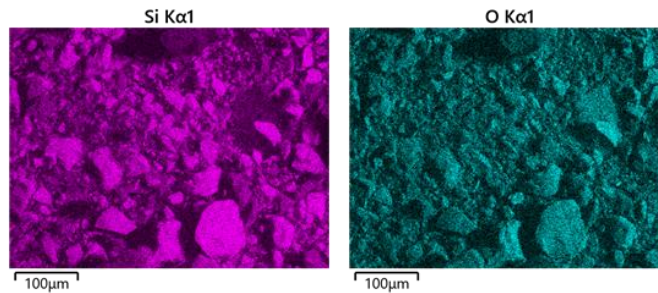


Figure 87: SEM mappings of Figure 86: Si (left) and O (right)

The light spots in the SEM image indicate the presence of heavy elements. This correlates with the Fe mapping of this SEM image in Figure 88. In some Fe-rich particles Al and O or Al, O and Mg are present (Figure 88 and Figure 89). In the bright spot in the left bottom corner, there seems to be only Fe without any correlation.

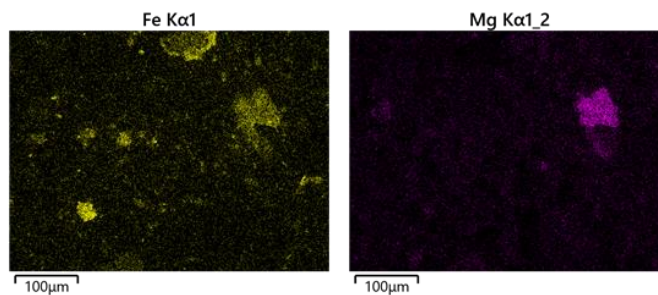


Figure 88: SEM mappings of Figure 86: Fe (left) and Mg (right)

In the following mappings of K and Al a positive correlation between these two and the presence of Si in these areas can be observed.

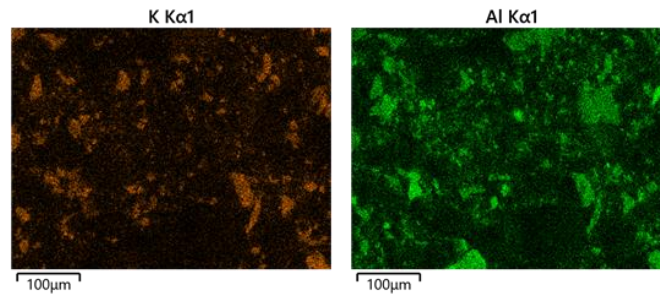


Figure 89: SEM mappings of Figure 86: K (left) and Al (right)

Very similar effects can be seen in other SEM images. In SEM image 4 it is clearly visible that P, Fe and Ca occur in the same spots of the probe.

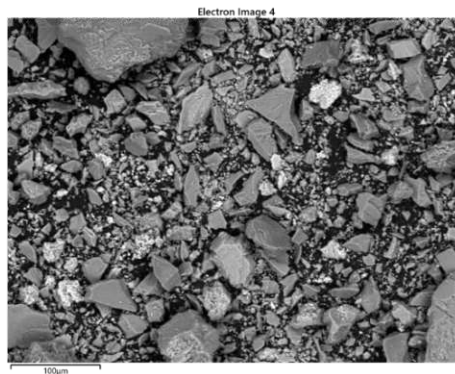


Figure 90: SEM image 4, experiment 5, bottom ash

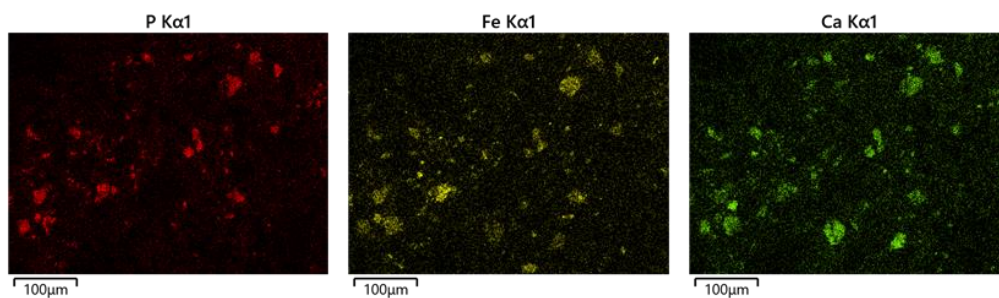


Figure 91: SEM mappings of Figure 90: P (left), Fe (middle) and Ca (right)

In the previously described gasification run with fuel 2, the higher K to Ca ratio is prima facie a desired effect. It leads to the assumption that more K-bearing phosphates than Ca-phosphates were formed. On taking a closer look at the data, a large correlation between spots of high K, Al and Si concentrations can be observed. This gives reason to believe that feldspar or similar compounds

were formed. P seems to correlate, on the other hand with Ca and Fe in particular. As this is also the case in the fuel, it is expected that no great change in formation was achieved in the gasification run. The assumption that there are primarily Fe-phosphates present in the bottom ash similar to the sewage sludge itself is supported by the fact that the Fe concentration decreased in a similar way as P in contrast to other elements. This is further underlined by the mappings in Figure 91. The raised Al concentration in comparison to the P concentration underlines the assumption that feldspar was formed. This can also be seen in Figure 89.

The iron precipitation in Figure 87 Figure 88 respectively is very notable in this probe. Gasification conditions could enhance this phenomenon. It is noticeable that the Mg share is very low, and Mg appears in only small amounts over the whole ash. In image 2, Mg occurs in correlation with Fe and O. This diminishes the probability of K/Mg-phosphates forming under these conditions.

Cyclone ash

The cyclone ash of experiment 5 under gasification conditions shows a very dark colour in comparison to the cyclone ash of the same fuel under combustion conditions. Furthermore, it seems to be less diluted with bed material. The integrity of the sunflower husk threads is maintained to a higher degree than under combustion conditions.

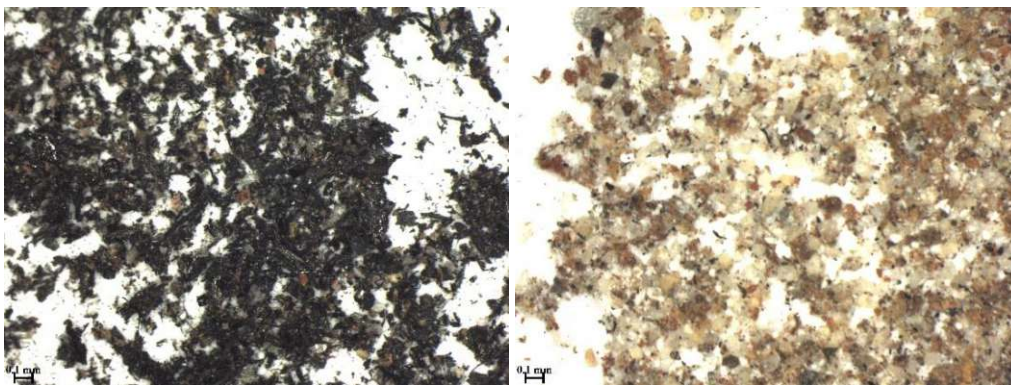


Figure 92: Light microscope image, cyclone ash, gasification conditions (left) and combustion conditions (right)

The Si share of the cyclone ash is significantly raised compared to the original composition of the fuel and the dilution with bed material can be seen in the following SEM picture. This leads to distortion of the ash element concentrations regarding fuel composition. Nevertheless, the K share is considerably less than in the fuel. Furthermore, the Ca share is raised even when taking the Si

dilution into account. Chloride concentrations are higher than in the fuel and the sulphide concentration (5.9 mol%) is notably higher than in the bottom ash fraction (0.4 mol%). While most element concentration decreases, the Na content of the cyclone ash is higher than the one in the fuel.

Table 29: average molar percentage of elements in the cyclone ash, experiment 5

mol%	Na	Mg	Al	Si	P	S	Cl	K	Ca	Ti	Fe
Fuel	1.4	7.7	7.3	14.6	14.1	8.0	1.1	15.9	16.0	1.3	12.7
Cyclone ash	1.7	7.1	6.9	29.8	11.6	5.9	2.0	5.6	18.6	1.0	9.8

The concentrations of the elements in the combustion and in the gasification case are very similar except for the higher Si concentration in the combustion case. The K/Ca ratio is almost the same in both cases. There is more Mg and P in the gasification case in comparison to the other elements.

In SEM image 4 bed material, sewage sludge and sunflower husk can be observed as separate particles. As formerly described, the integrity of the sunflower husk threads remains.

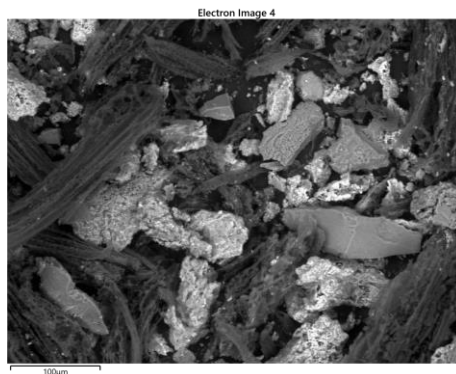


Figure 93: SEM image 4, experiment 5, cyclone ash

This observation is confirmed in the SEM mappings of the elements as the sunflower husk threads consist mainly of carbon, that has not been oxidised. Bed material particles can be detected on account of their high share of Si and O, and sewage sludge particles show higher concentrations of P, Fe, K, Ca and Al.

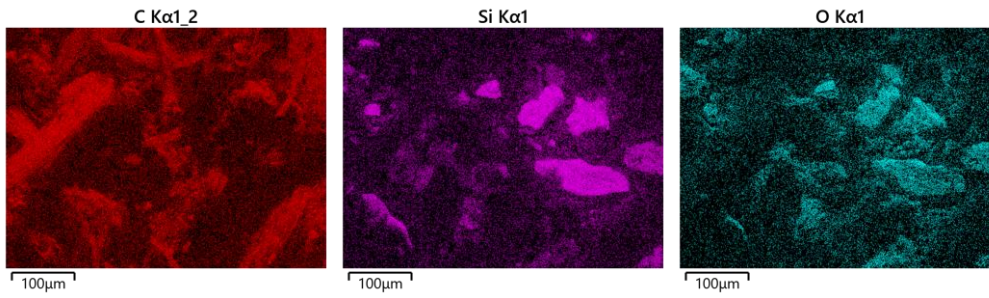


Figure 94: SEM mappings of Figure 93: C (left), Si (middle) and O (right)

There is high correlation between Fe and P. A high Fe share is already indicated by the light spots on the particles in SEM image 4. Areas of higher S concentration also show a significant amount of Ca.

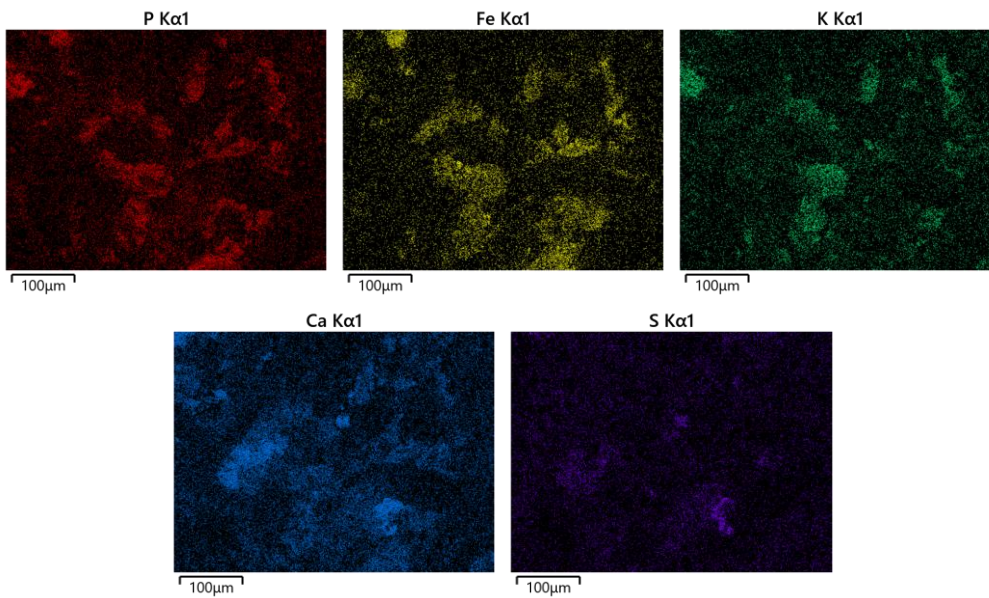


Figure 95: SEM mappings of Figure 93: P (above, left), Fe (above, middle), K (above, right), Ca (below, left) and S (below, right)

The aluminium concentration correlates with P, but also with Si and Na as seen in Figure 96.

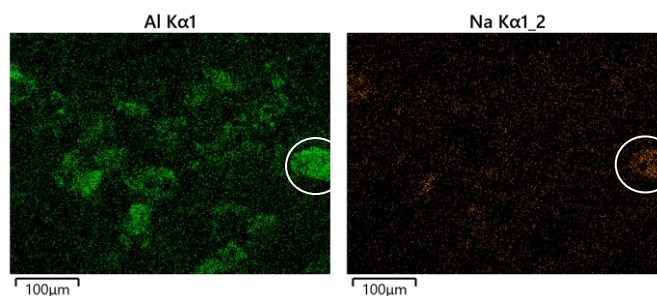


Figure 96: SEM mappings of Figure 93: Al (left) and Na (right)

Higher Mg and Ca shares indicate the presence of Mg-bearing Ca-phosphates. It is not completely clear in which form Al/Fe/Ca/K-phosphates are present. The dominance of Fe in concentration and in correlation with P in P-rich spots, leads to the assumption of the presence of a significant amount of iron phosphates.

Regarding optical factors, the dark colour of the cyclone ash in experiment 5 could derive from a high peak in temperature after an accidentally large feed of fuel. As there was less oxidation of carbon, the form of the sunflower husk threads was maintained and a large amount of carbon can still be observed in the ash.

It is assumed that sewage sludge particles and sunflower husk particles did not fuse well in this experiment. SEM images and their mappings show the separation of the two fractions. This is unsatisfactory as the aim was to acquire more K-bearing phosphates. In comparison to the K content in the fuel, the K concentrations is low. This supports the premise of the formation of fewer K-bearing phosphates. K seems to form volatile compounds and to be emitted in the exhaust gas.

Other volatile compounds such as Cl and S appear in higher concentrations in this ash fraction. This phenomenon was formerly observed and described. The formation of compounds as Al/Na-silicates can be observed in this ash fraction which could lead to fewer Al-phosphates and more Al-silicates. The dominant phosphates in this fraction seem to be Fe-phosphates and Ca-phosphates.

Filter ash

As previously seen with the cyclone ash, the filter ash under gasification conditions is also much darker than the filter ash of the same fuel under combustion conditions.

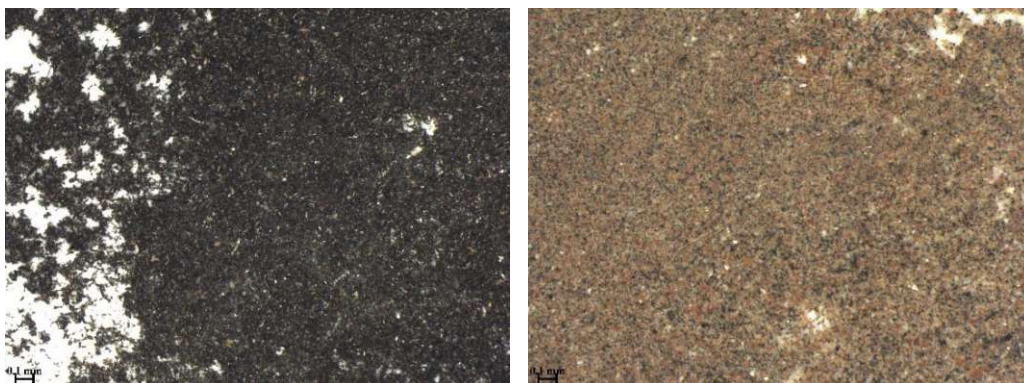


Figure 97: Light microscope image, filter ash, experiment 5 (left) and experiment 2 (right)

The composition of the filter ash is remarkable in several aspects. There are exceptionally large shares of Mg, S, Cl and Ca to be found in this ash compared to fuel composition and to the composition of the other ash fractions. The distribution of elements is almost the same as in experiment 2 with the same fuel under combustion conditions. However the Cl share is notably higher and the Fe concentration a little bit lower. The ash fraction seems to be the least diluted with bed material of the three ash fractions.

Table 30: Average molar percentage of elements in the filter ash, experiment 5

mol%	Na	Mg	Al	Si	P	S	Cl	K	Ca	Ti	Fe
Fuel	1.4	7.7	7.3	14.6	14.1	8.0	1.1	15.9	16.0	1.3	12.7
Filter ash	2.6	11.05	7.2	15.1	12.7	8.9	3.0	5.5	24.4	1.0	8.7

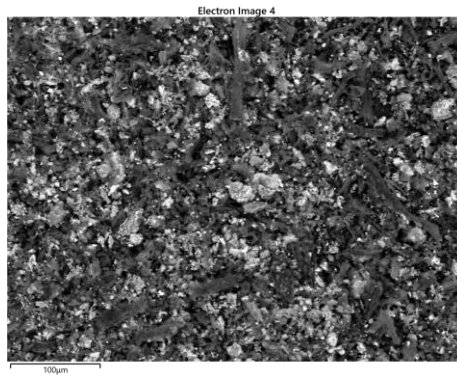


Figure 98: SEM image 4, experiment 5, filter ash

Although the ash fraction is less diluted than the others, there are still some bed material particles to be observed in the SEM mappings of Si and O. Uncombusted carbon remains in the ash as seen in Figure 99.

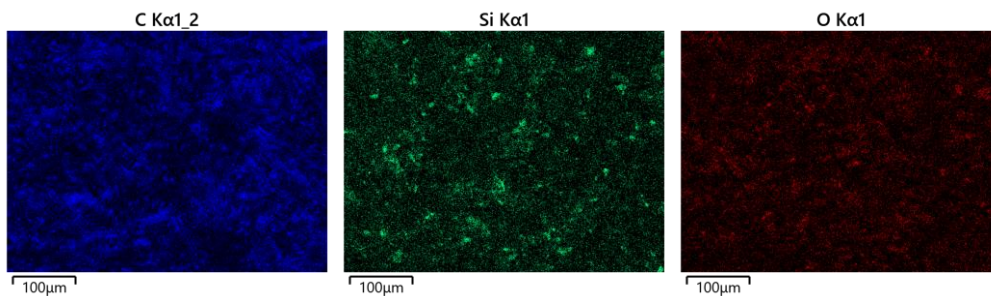


Figure 99: SEM mappings of : C (left), Si (middle) and O (right)

The filter ash shows high concentration of Ca and a few spots of high intensity of Ca that do not seem to correlate with any particular element. Some correlation with phosphorous can be observed. Furthermore, Fe and Al are present in P-rich areas.

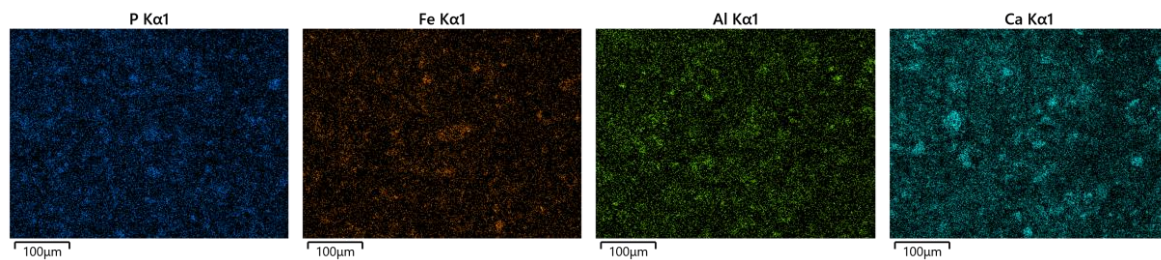


Figure 100: SEM mappings of Figure 99: P(left), Fe (2nd from left), Al (3rd from left) and Ca (right)

The presence of S and Cl over the ash fraction can be observed in Figure 101. Some calcium-sulphates seem to have formed.

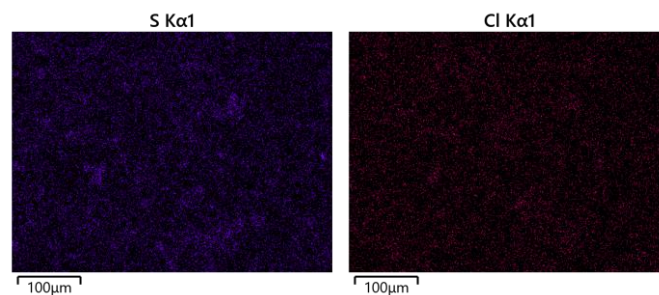


Figure 101: SEM mappings of Figure 99: S (left) and Cl (right)

Wheat straw and sewage sludge particles can be distinguished from each other. The carbon share is associated primarily with the wheat straw particles. A high Ca content leads to the assumption that Ca-phosphates and Ca/Mg-phosphates are present. Ca-phosphates are already present in the fuel, but in the mapping, there is a much higher concentration of Ca to be observed than in the fuel. On the one hand, this might give reason to presume the formation of further Ca-phosphates. On the other hand, it seems inevitable that some Ca-sulphates were formed. As K-phosphates are the desired composition, it appears favourable that some Ca atoms might bond elsewhere. Nevertheless, the K concentration in this ash fraction is almost negligible. This does not seem to be the desired ash fraction for further use as fertilizer. Fe precipitation can be observed as well as some correlation of Fe and P to form Fe-phosphates.

3.6. Experiment 6

Bottom ash

The elemental composition of all ashes in experiment 6 show a large S and Cl content compared to the composition of the ashes in experiment 3 with the same fuel under combustion conditions. This is coherent with previous observations in the former gasification experiments with different fuels. As expected, the S and Cl percentages in the bottom ash are still only about a quarter of the percentages in the other ash fractions. The ash under gasification conditions seems to be less diluted than the bottom ash under combustion conditions. This was also the case for the previously discussed experiments with fuel 1 and 2. The K/Ca ratio in experiment 6 is with 1.1 to 1.7 lower than in experiment 3. A greater content of iron can be observed for fuel 3 under gasification conditions. The Al/Fe ratio of 0.8 is significantly lower than that in experiment 3 with 1.2. Ca and Fe are more prominent under gasification conditions.

Table 31: average molar percentage of elements in the filter ash, experiment 5

mol%	Na	Mg	Al	Si	P	S	Cl	K	Ca	Ti	Fe
Fuel	1.0	3.5	5.1	34.8	9.3	4.6	4.7	17.1	11.1	0.8	8.1
Bottom ash	2.1	1.2	7.3	55.4	9.5	1.2	0.1	7.5	6.6	0.8	8.3

The SEM image shows diluted bottom ash. Bed material particles and ash particles can be observed. The ash particles seem to have separated into sewage sludge fractions and wheat straw fractions. In the image the light particles catch the eye. These areas correlate with the Fe mapping. The same particles show a high concentration of Fe which was not registered to this extent in experiment 3. Light spots can be seen in the circled area. They appear on a particle of high carbon concentration as seen in the mappings below. The spots correlate with the silicate mapping.

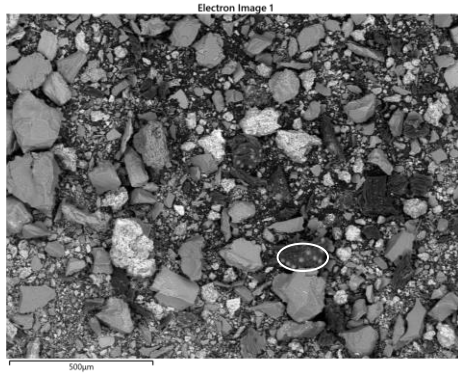


Figure 102: SEM image 1, experiment 6, bottom ash

The uncombusted carbon seems to appear in the wheat straw fibres. The areas of high carbon intensity do not correlate strongly with other elements. Al and Na show strong correlation with each other and with Si.

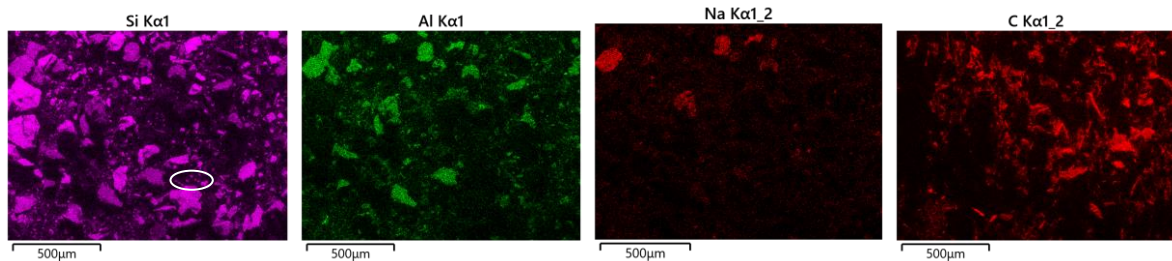


Figure 103: SEM mappings of Figure 102: Si (left), Al (middle) and Na (right)

In the following mappings correlations of phosphorous with Ca, K, Fe and the previously discussed Al can be observed. A correspondence between K and Al can be observed in certain areas.

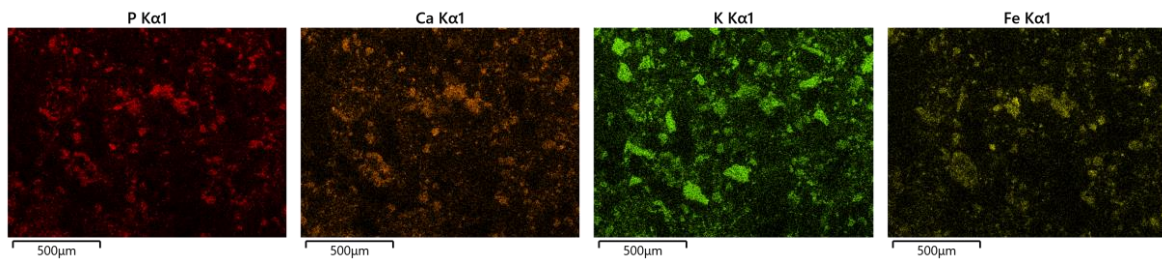


Figure 104: SEM mappings of Figure 102: P (left), Ca (2nd from left), K (3rd from left) and Fe (right)



Figure 105: SEM image 7, experiment 6, bottom ash

The difference in composition of the ash particles can also be observed in SEM image 7 and its mappings respectively. There are particles with high carbon concentration that also contain a little sulphur and silicate. In these areas few other elements are present; the same is true for the carbon mapping.

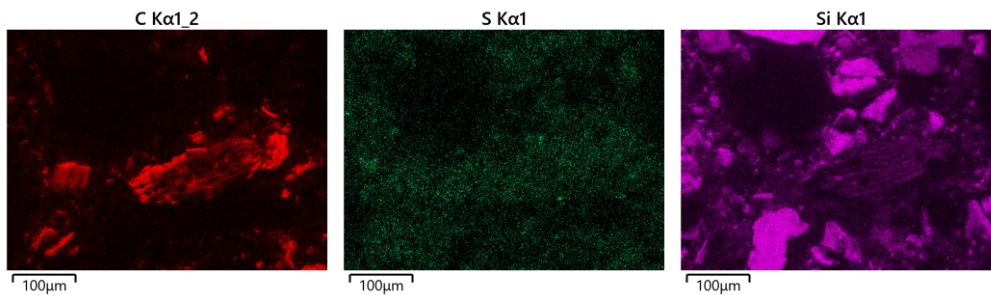


Figure 106: SEM mappings of Figure 105: C (left), S (middle) and Si (right)

The mappings of image 7 underline the previous statement concerning correlations between Al, K and Si. P-rich areas show higher concentrations of all four elements Fe, Ca, K and Al.

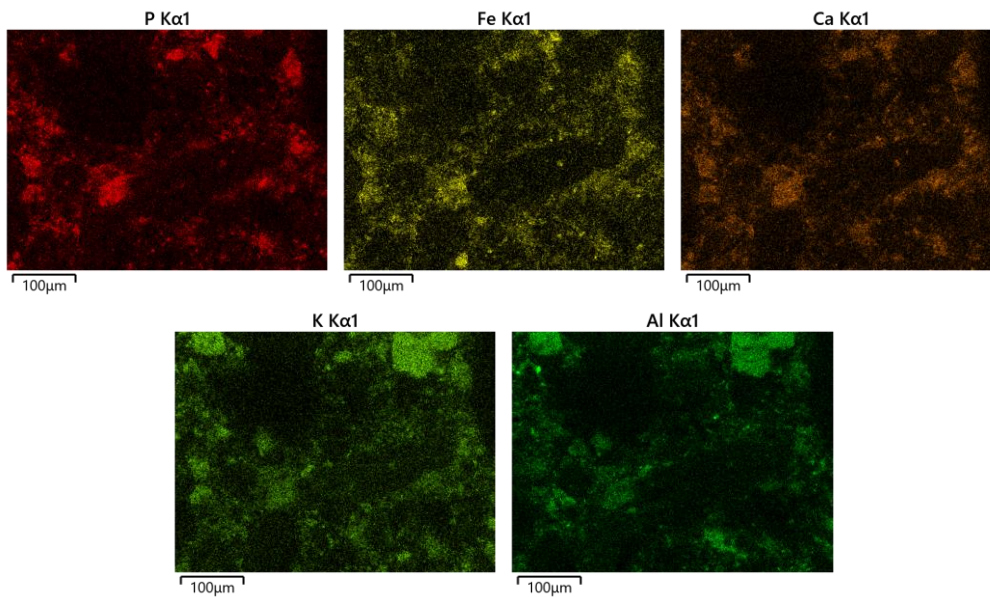


Figure 107: SEM mappings of Figure 105: P (above, left), Fe (above, middle), Ca (above, right), K (below, left) and Al (below, right)

It is assumed that the formation of different kinds of feldspar consisting of Al/Na/Si or Al/K/Si particles took place. The higher Fe concentration in this experiment in comparison to the experiment conducted under combustion conditions could be caused by stronger Fe precipitation. This could lead to fewer Fe phosphates and to the formation of other more bio available phosphates. There is still a strong correlation between Fe and P to be seen as well, as for Ca, K and Al with phosphorous. The K/Ca ratio is greater than in experiment 3, but K shows a high correlation with Al and Si by forming feldspar.

In general, the dilution factor under gasification conditions seems to be smaller. Less inclusion of bed material in the ash particles could be the reason. Nevertheless, some inclusions could also be observed in this experiment as spots of high Si concentration are visible in ash particles.

Cyclone ash

The optical reception of the cyclone ash of fuel 3 under gasification and under combustion conditions differ from one another. The ash in the gasification run is darker, more homogenous, and less diluted.

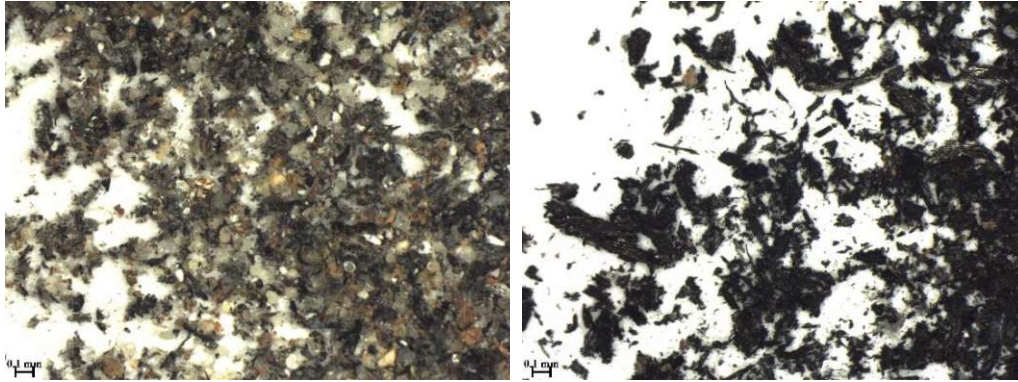


Figure 108: Light microscope image of cyclone ash in experiment 3 (left) and experiment 6 (right)

The ash composition of experiment 6 is again very similar to that with the same fuel under combustion conditions. As shown for fuel 2, the main difference lies in the stronger presence of sulphur and chloride. Also, the Na share is raised, and the Al concentration is significantly lower than in experiment 3 (1.6% and 3.1 mol%). The Si dilution seems to be similar and therefore the results better comparable.

In contrast to the original fuel concentrations, the iron and aluminium shares are diminished. In all ash fractions a low K concentration compared to the original concentration can be observed.

Table 32: : average molar percentage of elements in the cyclone ash, experiment 6

mol%	Na	Mg	Al	Si	P	S	Cl	K	Ca	Ti	Fe
Fuel	1.0	3.5	5.1	34.8	9.3	4.6	4.7	17.1	11.1	0.8	8.1
Cyclone ash	2.2	3.7	1.6	55.0	6.4	4.2	4.6	7.0	12.0	0.2	3.1

In SEM image 2 the shape and composition of the ash is displayed. The structure of the wheat straw particles seems to have been maintained during the gasification process. In the mappings, high C and Si concentrations appear in the same spots where fibre structures can be noticed. A great share of uncombusted carbon is to be observed. In some fibre structures little spots of high Si concentration appear as seen in the circled area.

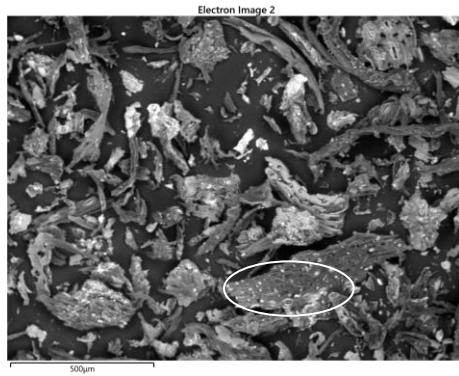


Figure 109: SEM image 2, experiment 6, cyclone ash

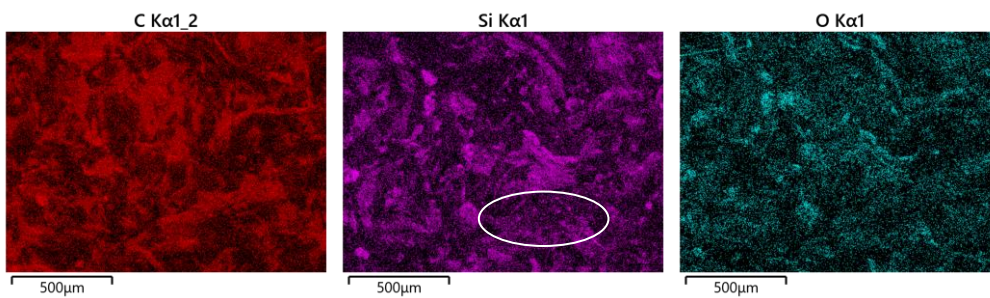


Figure 110: SEM mappings of Figure 109: C (left), Si (middle) and O (right)

P-rich areas also show the presence of Ca, K and Fe in the mappings. The Fe-P correlation is positive. The Si-P/Fe correlation is negative. There is fewer Fe and fewer P present than in the other ash fractions.

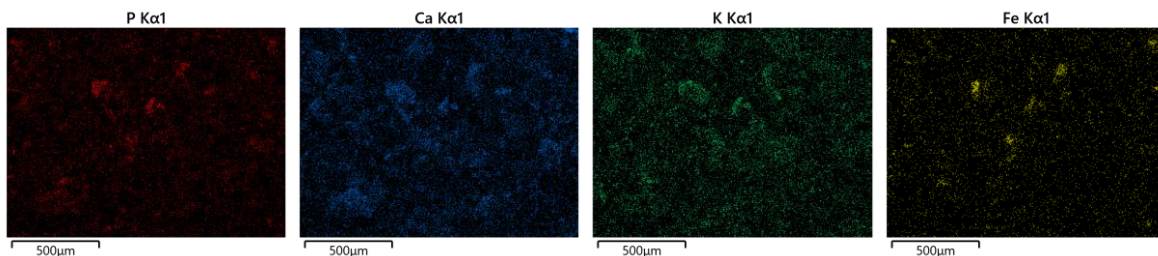


Figure 111: SEM mappings of Figure 109: SEM image 2, experiment 6, cyclone ash Figure 109: P (left), Ca (2nd from left), K (3rd from left) and Fe (right)

In SEM image 4 the previously described inclusion of bed material particles is shown in detail. Compared to the Si mapping, a strong correlation between the light spots in the SEM image and the spots of higher intensity in the SEM mapping become evident.

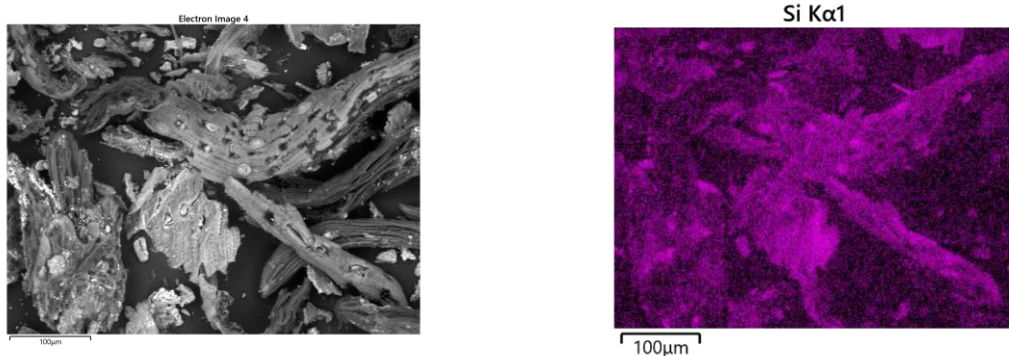


Figure 112: SEM image 4 and SEM mapping of Si, experiment 6, cyclone ash

The diminished P and Fe concentrations could relate to a reduced presence of sewage sludge particles in the cyclone ash. It seems that the wheat straw particles are predominant in this ash fraction. It is not entirely possible to determine the level of blending of the fractions. The formation of more volatile sulphur and chloride compounds during gasification is assumed as the S and Cl concentrations are notably higher than under combustion conditions. Considering these mappings, it is hard to draw conclusions about the phosphate composition. Regarding K-bearing phosphates this fraction does not seem promising.

Filter ash

The filter ash of the gasification of fuel 3 is significantly darker than the filter ash of the same fuel under combustion conditions. The shape and size appear to be similar.

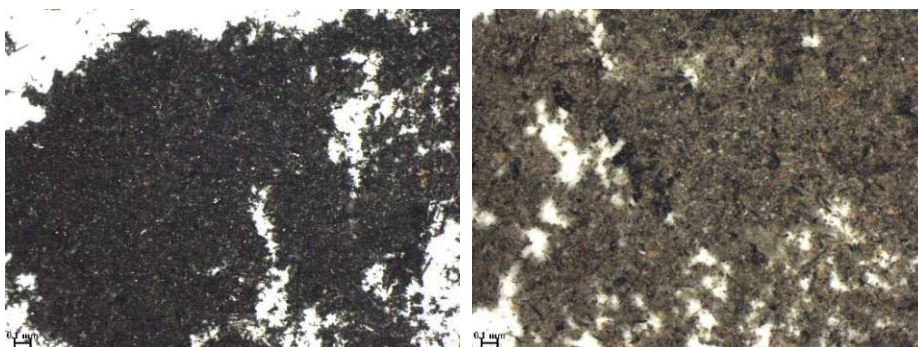


Figure 113: Light microscope image of filter ash in experiment 6 (left) and experiment 3 (right)

The Na share of the filter ash is considerably higher in comparison to the original composition. Nevertheless, it is still lower than the Na concentration in experiment 3 under combustion conditions at 4.5 mol%. The results are the opposite for magnesium. The filter ash in experiment 6 shows higher Mg, the filter ash in experiment 3 lower Mg concentrations (2.5 mol%) than in the original fuel. Under combustion conditions a drastic rise in Al concentration could be detected in the filter ash. This is not the case here under gasification conditions. The distribution of K and Ca over the ashes diverges strongly when conditions are changed. Under combustion conditions a significant rise in K concentration to 18 mol% could be seen and Ca concentrations were merely 5.6 mol%. Under gasification conditions the K concentration only amounts to 7.2 mol% and the Ca concentration shows 13.6 mol%. The iron share is small compared to the original concentration and in comparison to the results of experiment 3.

Table 33: Average molar percentage of elements in the filter ash, experiment 6

mol%	Na	Mg	Al	Si	P	S	Cl	K	Ca	Ti	Fe
Fuel	1.0	3.5	5.1	34.8	9.3	4.6	4.7	17.1	11.1	0.8	8.1
Filter ash	3.1	4.7	3.2	43.6	8.0	4.9	7.5	7.2	13.6	0.4	4.2

SEM image 7 gives a picture of the inhomogeneous filter ash. Uncombusted carbon particles and bed material dilution can be observed.

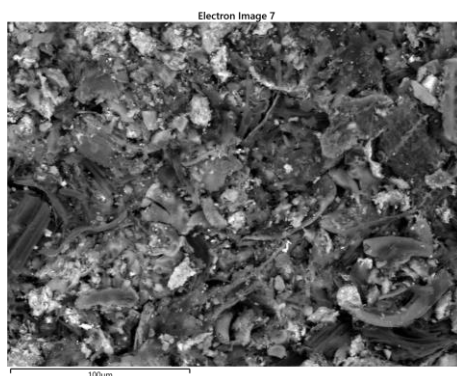


Figure 114: SEM image 7, experiment 6, filter ash

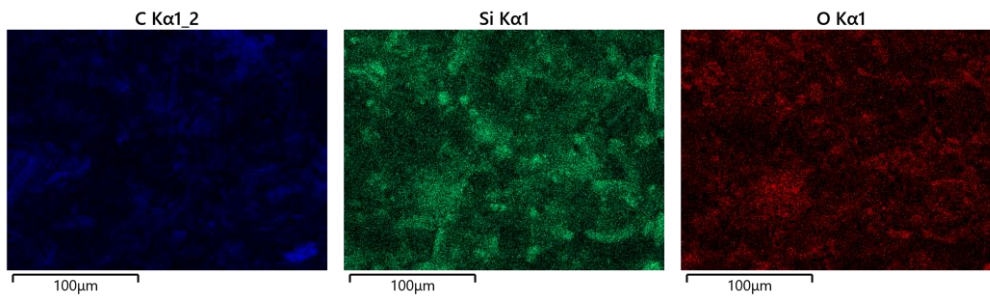


Figure 115: SEM mappings of Figure 114: C (left), Si (middle) and O (right)

Although the Fe concentration is low, areas of high Fe intensity correlate with P-rich areas. Some other correlations between Al and P and Ca and P can be observed. The Ca/P correlation seems to be weaker than the others.

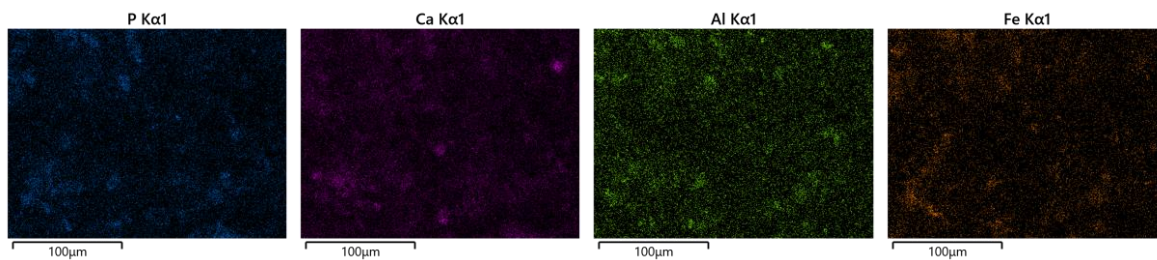


Figure 116: SEM mappings of Figure 114: P (left), Ca (2nd from left), Al (3rd from left) and Fe (right)

In accordance with previous observations, Cl and S concentrations are highest in the filter ash. Whereas the sulphur concentration is comparable to that under combustion conditions, the chloride concentration is almost 19 times higher (7.5 mol% to 0.4 mol%). In the following mappings correlations between spots of high K and high Cl concentration can be seen. Ca is also present in S-rich areas.

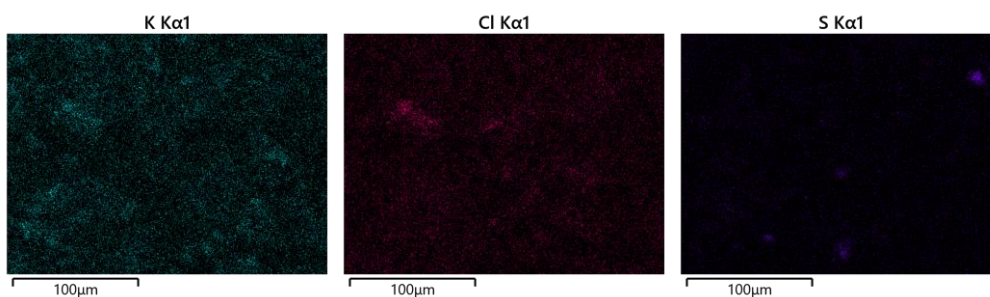


Figure 117: SEM mappings of Figure 114: K (left), Cl (middle) and S (right)

High Na and Mg concentrations, equally distributed over the ash, lead to the assumption that the two fuel fractions sewage sludge and wheat straw have blended to some extent. The wheat straw particles show very low Na and Mg share which would be provided by the sewage sludge particles. It is, therefore, likely that Mg- or Na-bearing phosphates will be found in the ash.

Low K share indicates the lack of formation of K bearing phosphates. Ca-phosphates appear to be more prominent in this fraction due to mapping results and total Ca concentration. Nevertheless, correlations between phosphorous and aluminium and iron are dominant. The lower iron concentration could be a result of precipitation of iron during gasification. It still correlates strongly with phosphorous. Therefore, it is assumed that Fe-phosphates as well as Ca-phosphates remained stable and the tendency to form other phosphates was weak.

This ash fraction stands out regarding its chloride concentration. Performance conditions seem to have an influence on the formation of KCl and other volatile chloride components. A correlation between K and Cl can be observed in the mappings of the filter ash. There is less K in the ash than in the original fuel and K appears to form compounds with Cl. Therefore, the formation of K bearing phosphates becomes less likely. As observed in other ash fractions under gasification conditions, Ca-sulphates seem to be present in the filter ash. These compounds appear to be more volatile as they are found primarily in the filter ash where a correlation between K and Cl can be observed in the mappings of the filter ash.

Chapter 4

Conclusion

In all the experiments and ash fractions, the K content in ashes is less than in the fuels. It can be expected that K forms volatile compounds which are partly exhausted via the chimney. One of these compounds could be KCl as it was also detected in the filter ash fraction where the condensation temperature is lower. KCl is a common product in biomass processes (Wei, Schnell and Hein, 2005). This correlates with observations in this study of lower Cl concentrations in all ash fractions compared to Cl concentrations in the fuel. Equilibrium calculations suggest that the Si-lean SH ash tends to form volatile K compounds. SS and WS-rich ashes contain a high level of anionic compounds such as PO_4^{3-} and SiO_4^{4-} which may create solid K compounds. The volatilization of K therefore does not occur to the same extent as in SH-rich ashes (Hannl et al., 2021). This can be seen to some extent in the ash fractions examined. The cyclone and filter ashes of fuel 2 (SS and SH) show a low K/Ca ratio in comparison to the K/Ca ratio of experiment 3 with fuel 3 (SS and WS). A higher concentration of K can be observed. Nevertheless, the bottom ash fractions of all three experiments under combustion conditions appear to be promising regarding the formation of K bearing phosphates. Comparing the co-combustion with biological residues to the combustion of sewage sludge only, blending and positive effects on the formation of K bearing phosphates are indicated. K seems to be equally distributed over the bottom ashes of experiment 2 and 3.

This changes under gasification conditions. The K/Ca ratio seems to be affected by the experiment conditions. Under gasification conditions there is less K to be found in the ashes of all three fuels. More correlations of K, Al and Si were detected as these elements tend to form feldspar. Furthermore, the KCl correlation and concentration is significantly raised in comparison to the experiments under combustion conditions. In experiment 4 in particular, the formation of feldspar and KCl can be observed in the filter ash, but also in the cyclone ash a greater correlation between K and Si than between K and P was detected. This is the case for all gasification probes. As regards the K/Ca ratio and the K-P correlation these fractions are not promising. In the bottom ash of experiment 5 and 6 a strong correlation between K, Al and Si was detected. The K-P correlation in the cyclone and filter ash fractions of experiments 5 and 6 appear to be very low. Nevertheless, feldspar is detected in almost all ash fractions. The cyclone ash of experiment 2 and 3 and the bottom ash of experiment 3 show high concentrations of Al-Si and Al-Si-K. Under gasification conditions the Fe-P

and the Ca-P correlations appear to be predominant. As these compounds already exist in the fuel, it is assumed that the blending of the fuel fractions and the conversion of Fe and Ca phosphates to K phosphates progressed unsatisfactorily. This correlated with the SEM and light microscope images where the fibres of the biological residues and the sewage sludge particles can easily be distinguished from one another. This is not a good sign for the desired blending process. Precipitation of Fe was registered in the bottom ash of experiments 1, 2 and 6, in the cyclone ash of experiment 2 and the filter ash of experiment 5. It is not possible to determine the effect of performance conditions or fuel on the precipitation of Fe. It may be favourable to let Fe precipitate in order to gain less iron-phosphates and enhance the formation of other phosphates. Bed material dilution occurs in all ash probes. This hampers the use of the ash as fertilizer and makes analysis and comparison of the fractions more difficult. As a result of this, alternative separation methods would have to be employed in order to receive the ash particles only. Furthermore, some bed material inclusion was detected in some fractions. This was more often the case in the bottom ash of the combustion experiments and in the biological fibres of fuels 2 and 3 under gasification conditions. A very promising ash fraction regarding fertilizer usage appears to be the bottom ash of fuel 2 under combustion conditions as a result of high K and low Ca concentrations and positive K-P correlations.

P-recovery outlook

For further use of sewage sludge ashes as fertilizer the heavy metal content needs to be examined. It is of interest if the use of biogenic residues like sunflower husk or wheat straw in co-combustion or co-gasification also effects the removal of heavy metals. Further analysis is yet to be conducted to examine the blending with additives to improve the volatilisation behaviour of heavy metals. Co-pyrolysis of sewage sludge with agricultural residues has shown its practical benefits in terms of heavy metal immobilization [16]. In studies that used chlorine donors to vaporize heavy metals through chlorination, because the vapor pressure of the respective heavy metals is higher compared to their oxides, vaporization of heavy metals can be observed. Cd, Pb, Zn, Ni and Cr can be completely vaporized as chlorides at temperatures below 1000 °C [31]. Co-combustion and co-gasification with biogenic residues like wheat straw, which shows high chloride concentration, seem promising regarding the removal of heavy metals. XRD analysis would give an extended insight in the actual formation of the phosphates. In this study the correlations were estimated by SEM analysis to get an overview of the existing elements. It would be of interest to quantify the amount of $\text{Ca}_5(\text{PO}_4)_3\text{OH}$, $\text{Ca}_5(\text{PO}_4)_6(\text{SiO}_4)_4(\text{OH})_6$, types of whitlockite ($\text{Ca}_3(\text{PO}_4)_2$), $\text{Ca}_4(\text{Mg,Fe})_5(\text{PO}_4)_6$, AlPO_4 , CaKPO_4 or silicates and aluminosilicates to assess the possibility of the ashes for fertilizer usage.

List of Figures

Figure 1: Structural formula of orthophosphate [13]	5
Figure 2: Occuring processes in the phosphorous cycle [6].....	5
Figure 3: Phosphorous accessibility for plants [6].....	6
Figure 4: Fuels used in the experiments: fuel 1 (left), fuel 2 (middle) and fuel 3 (right)	11
Figure 5: Flow chart of the process	12
Figure 6: bubbling fluidized bed reactor	12
Figure 7: Bunkers and flushing system used during the experiments: small bunker (left), big bunker (middle), N ₂ flush of bunkers (right).....	13
Figure 8: The feed flow is regulated by setting the rotation frequency of the screw conveyor (displayed on the left). The screw conveyor can be seen on the right.	13
Figure 9: Geldart figure for estimating the behaviour of particles according to their density and size [22]	14
Figure 10: Forces on the particles relevant for classifying after Geldart [20].....	14
Figure 11: Rotameter (left) and valve (right)	16
Figure 12: The electron can interact with the atom in the following ways: (a) low angle scattering, (b) back or high-angle scattering, (c) emission of a secondary electron and characeristic x-rays, (d) emission of a secondary electron and an Auger electron [23].....	18
Figure 13: The electron beam interacts with atoms up to a specific specimen depth. Backscattered electrons and x-rays are emitted from these regions [23].....	19
Figure 14: The SEM analysis gives a spectrum of peaks of different heights at intensities characteristic for each element	20
Figure 15: The ash fractions amount to different percentages of the total ash depending on the experiment	22
Figure 16: The heating, combustion and cooling down periode of experiment 1 are portrayed in the temperature profile.....	24
Figure 17: Gas composition profile of experiment 1.....	25
Figure 18: Temperature profile of experiment 2	26
Figure 19: Gas composition of experiment 2	26
Figure 20: SEM image 1, bottom ash, experiment 1	28
Figure 21: SEM mapping of Si in SEM image 1	28
Figure 22: SEM image 2, bottom ash, experiment 1	28
Figure 23: SEM mapping of SEM image 2: Fe (left) and Si (right)	28

Figure 24: bottom ash experiment 1, inclusion of bed material particles	29
Figure 25: SEM image 3 of cyclone ash, experiment 1.....	30
Figure 26: SEM mappings of SEM image 3 (cyclone ash, experiment 1) P(left), Fe (middle) and Ca (right).....	30
Figure 27: SEM image 6, cyclone ash, experiment 1.....	31
Figure 28: SEM mappings of SEM image 6: P (left), Fe (middle) and Ca (right)	31
Figure 29: SEM mappings of SEM image 6: Na (left) and K (right)	31
Figure 30: Light microscope image of cyclone ash, experiment 1	31
Figure 31: SEM image of cyclone ash, experiment 1.....	32
Figure 32: SEM mappings of SEM image 1 (cyclone ash, experiment1) Si (left), O (middle) and Ca (right).....	32
Figure 33: SEM image 1, filter ash, experiment 1	33
Figure 34: SEM mappings of Figure 33: Si (left), Ca (2 nd from left), P (3 rd from left) and Fe (right)	33
Figure 35: SEM mappings of Figure 33: SEM image 1, filter ash, experiment 1: S (left) and Cl (right)	34
Figure 36: SEM image 3, filter ash, experiment 1	34
Figure 37: SEM mapping of Figure 36: Ca (left), Fe (middle) and P (right).....	35
Figure 38: SEM image 1, bottom ash, experiment 2	36
Figure 39: SEM mappings of Figure 38 : Fe (left), Mg (2 nd from left), Na (3 rd from left) and Si (right) .	36
Figure 40: SEM mappings of Figure 38 : Ca (left), Al (2 nd from left), K (3 rd from left) and P (right)	36
Figure 41: SEM image 5, bottom ash, experiment 2	37
Figure 42: SEM mapping of Figure 41: Fe.....	37
Figure 43: SEM image 2 and light microscope image, cyclone ash, experiment 2	38
Figure 44: SEM mappings of Figure 43: Si (left) and O (right)	38
Figure 45: SEM mappings of Figure 43: Ca (above, left), P (above, middle), K (above, right), Mg (below, left), S (below, middle) and Fe (below, right).....	39
Figure 46: SEM image 5, cyclone ash, experiment 2.....	40
Figure 47: SEM mappings of Figure 46: Ca (above, left), P (above, middle), K (above, right), Mg (below, left), S (below, middle) and Fe (below, right).....	40
Figure 48: SEM mappings of Figure 46: Si (left), Al (middle) and K (right)	40
Figure 49: SEM image 1, filter ash, experiment 2	41
Figure 50: SEM mappings of Figure 71: Si (above, left), Ca (above, 2 nd from left), P (above, 3 rd from left), S (above, right), Mg (below, left), K (below, 2 nd from left) Fe (below, 3 rd from left) and Al (below, right)	42
Figure 51: SEM image 6, filter ash, experiment 2	43
Figure 52: SEM mappings of Figure 51: P(left), Ca (2 nd from left), K (3 rd from left) and Fe (right)	43

Figure 53: SEM image 2, experiment 3, bottom ash	45
Figure 54: SEM mappings of Figure 53: Al (left) and Si (middle) and O (right)	45
Figure 55: SEM mappings of Figure 79: Ca (left) and Fe (2 nd from left), K (3 rd from left) and P (right). 46	46
Figure 56: SEM mappings of Figure 79: Mg (left) and Na (middle) and S (right)	46
Figure 57: SEM image 8, experiment 3, bottom ash	46
Figure 58: SEM mappings of Figure 57: P (left), Fe (middle) and K (right)	46
Figure 59: SEM mappings of Figure 57: Ca (left) and Al (right)	47
Figure 60: SEM mappings of Figure 57: C.....	48
Figure 61: light microscope image cyclone ash, experiment 3	49
Figure 62: SEM image 3, experiment 3, cyclone ash.....	50
Figure 63: SEM mappings of Figure 62: Ca (left), K (2 nd from left), P (3 rd from left) and Fe (right)	50
Figure 64: SEM mappings of Figure 88: C.....	50
Figure 65: SEM mappings of Figure 88: Al (left), Si (middle) and O (right)	51
Figure 66: SEM mappings of Figure 88: S (left), Mg (middle) and Cl (right).....	51
Figure 67: SEM image 5, experiment 3, filter ash	52
Figure 68: SEM mappings of Figure 67: P(above, left), K (above, middle), S (above, right), Ca (below, left), Fe (below, middle) and Al (below, right)	53
Figure 69: SEM mapping of Figure 67: SEM image 5, experiment 3, filter ash: Cl	53
Figure 70: SEM image 6, experiment 3, filter ash	53
Figure 71: SEM mappings of Figure 70: P (above, left), Ca (above, middle), K (above, right), Al (below, left) and Fe (below, middle)	54
Figure 72: SEM image 1, experiment 4, bottom ash	55
Figure 73: SEM mappings of Figure 72: P (above, left), Al (above, 2 nd from left), Ca (above, 3 rd from left), K (above, right), Fe (bleow, left), Mg (below, middle) and S (below, right)	56
Figure 74: Light microscope image of the bottom ash in experiment 4 (left) and experiment 1 (right)	56
Figure 75: Light microscope image, experiment 4, cyclone ash.....	57
Figure 76: SEM image 2, experiment 4, cyclone ash.....	58
Figure 77: SEM mappings of Figure 76: Si (left) and O (right)	58
Figure 78: SEM mappings of Figure 76: P (above, left), Fe (above, middle), Ca (above, right), Al (below, left) and K (below, right)	59
Figure 79: SEM image 6, experiment 4, cyclone ash.....	59
Figure 80: SEM mappings of Figure 79: P (left), Fe (middle) and Ca (right)	59
Figure 81: P share in precipitaed phase, melt study with different fuels [16].....	60
Figure 82: SEM image 6, experiment 4, filter ash	61

Figure 83: SEM mappings of Figure 82: Si (above, left), O (above, 2 nd from left), P (above, 3 rd from left), Ca (above, right), Fe (below, left), Al (below, middle) K (below, right)	61
Figure 84: SEM mappings of Figure 85: Mg (below, left) and S (below, right).....	62
Figure 85: light microscope image, experiment 5, bottom ash	63
Figure 86: SEM image 2, experiment 4, bottom ash.....	64
Figure 87: SEM mappings of Figure 86: Si (left) and O (right)	64
Figure 88: SEM mappings of Figure 86: Fe (left) and Mg (right)	64
Figure 89: SEM mappings of Figure 86: K (left) and Al (right)	65
Figure 90: SEM image 4, experiment 5, bottom ash	65
Figure 91: SEM mappings of Figure 90: P (left), Fe (middle) and Ca (right)	65
Figure 92: Light microscope image, cyclone ash, gasification conditions (left) and combustion conditions (right).....	66
Figure 93: SEM image 4, experiment 5, cyclone ash.....	67
Figure 94: SEM mappings of Figure 93: C (left), Si (middle) and O (right)	68
Figure 95: SEM mappings of Figure 93: P (above, left), Fe (above, middle), K (above, right), Ca (below, left) and S (below, right).....	68
Figure 96: SEM mappings of Figure 93: Al (left) and Na (right).....	68
Figure 97: Light microscope image, filter ash, experiment 5 (left) and experiment 2 (right).....	69
Figure 98: SEM image 4, experiment 5, filter ash	70
Figure 99: SEM mappings of : C (left), Si (middle) and O (right)	70
Figure 100: SEM mappings of Figure 99: P(left), Fe (2 nd from left), Al (3 rd from left) and Ca (right)..	71
Figure 101: SEM mappings of Figure 99: S (left) and Cl (right)	71
Figure 102: SEM image 1, experiment 6, bottom ash.....	73
Figure 103: SEM mappings of Figure 102: Si (left), Al (middle) and Na (right)	73
Figure 104: SEM mappings of Figure 102: P (left), Ca (2 nd from left), K (3 rd from left and Fe (right) .	73
Figure 105: SEM image 7, experiment 6, bottom ash.....	74
Figure 106: SEM mappings of Figure 105: C (left), S (middle) and Si (right)	74
Figure 107: SEM mappings of Figure 105: P (above, left), Fe (above, middle), Ca (above,right), K (below, left) and Al (below, right)	75
Figure 108: Light microscope image of cyclone ash in experiment 3 (left) and experiment 6 (right) ..	76
Figure 109: SEM image 2, experiment 6, cyclone ash.....	77
Figure 110: SEM mappings of Figure 109: C (left), Si (middle) and O (right)	77
Figure 111: SEM mappings of Figure 109: SEM image 2, experiment 6, cyclone ashFigure 109: P (left), Ca (2 nd from left), K (3 rd from left) and Fe (right)	77
Figure 112: SEM image 4 and SEM mapping of Si, experiment 6, cyclone ash.....	78

Figure 113: Light microscope image of filter ash in experiment 6 (left) and experiment 3 (right).....	78
Figure 114: SEM image 7, experiment 6, filter ash	79
Figure 115: SEM mappings of Figure 114: C (left), Si (middle) and O (right)	80
Figure 116: SEM mappings of Figure 114: P(left), Ca (2 nd form left), Al (3 rd from left) adn Fe (right) ..	80
Figure 117: SEM mappings of Figure 114: K (left), Cl (middle) and S (right)	80
Figure 118: Temperature profile experiment 4.....	92
Figure 119: Temperature profile experiment 6.....	92
Figure 120: Temperature profile experiment 3.....	92
Figure 121: Temperature profile experiment 5.....	92
Figure 122: Gas composition experiment 4	92
Figure 123: Gas composition experiment 6	92
Figure 124: Gas composition experiment 3	92
Figure 125: Gas composition experiment 5	92

List of Tables

Table 1: World phosphate supply, demand and balance in the time frame of 2015-2020 [22] (in thousand tons P_2O_5)	2
Table 2: Central Europe phosphate supply, demand and balance in the time frame of 2015-2020 [22]	2
Table 3: predicted effects of climate change on agriculture over the next 50 years [11]	4
Table 4: Common phosphorous fertilizers and their sources [15]	7
Table 5: fuel composition, sewage sludge	8
Table 6: fuel composition, sunflower husk	8
Table 7: fuel composition, wheat straw	8
Table 8: Six different experiments with three different fuels were conducted.....	10
Table 9: Elemental composition of SS (1 st), SSH15 (2 nd) and WSS10 (3 rd)	11
Table 10: Data for calculating the produced ash in total with Equation 1.....	21
Table 11: Weighted ash mass fractions of bottom ash, cyclone ash and filter ash	22
Table 12: Comparison of the expected ash mass fractions versus the real ash mass fractions	23
Table 13: Average lambda values in the experiments 1-6	23
Table 14: The rotation frequency of the screw conveyor is calibrated according to the resulting mass flow of each fuel in a calibration curve	25
Table 15: Molar percentage of elements in the bottom ash of experiment 1.....	27
Table 16: molar percentage of elements in the filter ash and the fuel	34
Table 17: average mol percentage of elements in bottom ash, experiment 2	37
Table 18: Average molar percentage of elements in cyclone ash, experiment 2	39
Table 19: Average molar percentage of elements in filter ash, experiment 2.....	42
Table 20: Molar percentages of each element in SEM image 2, cyclone ash, experiment 2 (left) and in SEM image 1, filter ash, experiment 2 (right)	44
Table 21: Molar concentrations of the elements in SEM image 8	47
Table 22: average molar percentage of elements in bottom ash, experiment 3.....	48
Table 23: Average molar percentage of elements in cyclone ash, experiment 3	49
Table 24: average molar percentage of elements in the filter ash, experiment 3.....	52
Table 25: Average molar percentage of elements in the bottom ash, experiment 4	55
Table 26: average molar percentage of elements in the cyclone ash, experiment 4	57
Table 27: Average molar percentage of elements in the filter ash, experiment 4	61
Table 28: Average molar percentage of elements in the bottom ash, experiment 5	63

Table 29: average molar percentage of elements in the cyclone ash, experiment 5	67
Table 30: Average molar percentage of elements in the filter ash, experiment 5	70
Table 31: average molar percentage of elements in the filter ash, experiment 5.....	72
Table 32: : average molar percentage of elements in the cyclone ash, experiment 6	76
Table 33: Average molar percentage of elements in the filter ash, experiment 6	79

Bibliography

- [1] D. Cordell, J.-O. Drangert, und S. White, „The story of phosphorus: Global food security and food for thought“, *Tradit. Peoples Clim. Change*, Bd. 19, Nr. 2, S. 292–305, Mai 2009, doi: 10.1016/j.gloenvcha.2008.10.009.
- [2] C. D. Fraiture, „Future Water Requirements for Food - Three Scenarios“, *International Water Management Institute (IWMI)*, Nr. August 12th-18th, 2007.
- [3] I. Steen, „Phosphorus availability in the 21st century : Management of a non-renewable resource“, *Phosphorus Potassium*, Bd. 217, S. 25–31, 1998.
- [4] S. Jasinski, „Phosphate Rock Data Sheet“, USGS, geological survey, Jan. 2021. Zugegriffen: 27. Juni 2021. [Online]. Verfügbar unter: <https://pubs.usgs.gov/periodicals/mcs2021/mcs2021-phosphate.pdf>
- [5] P. Heffer und I. F. Society, *Phosphorus Fertilisation: Issues and Outlook*. International Fertiliser Society, 2006. [Online]. Verfügbar unter: <https://books.google.at/books?id=JWT2xwEACAAJ>
- [6] A. Bhattacharya, „Chapter 5 - Changing Environmental Condition and Phosphorus-Use Efficiency in Plants“, in *Changing Climate and Resource Use Efficiency in Plants*, A. Bhattacharya, Hrsg. Academic Press, 2019, S. 241–305. doi: 10.1016/B978-0-12-816209-5.00005-2.
- [7] Y. Xu, H. Hu, J. Liu, J. Luo, G. Qian, und A. Wang, „pH dependent phosphorus release from waste activated sludge: contributions of phosphorus speciation“, *Chem. Eng. J.*, Bd. 267, S. 260–265, Mai 2015, doi: 10.1016/j.cej.2015.01.037.
- [8] S. Li, W. Zeng, Z. Jia, G. Wu, H. Xu, und Y. Peng, „Phosphorus species transformation and recovery without apatite in FeCl₃-assisted sewage sludge hydrothermal treatment“, *Chem. Eng. J.*, Bd. 399, S. 125735, Nov. 2020, doi: 10.1016/j.cej.2020.125735.
- [9] R. Li, J. Cui, X. Li, und X. Li, „Phosphorus Removal and Recovery from Wastewater using Fe-Dosing Bioreactor and Cofermentation: Investigation by X-ray Absorption Near-Edge Structure Spectroscopy“, *Environ. Sci. Technol.*, Bd. 52, Nr. 24, S. 14119–14128, Dez. 2018, doi: 10.1021/acs.est.8b03355.
- [10] A. Bhattacharya, „Chapter 1 - Global Climate Change and Its Impact on Agriculture“, in *Changing Climate and Resource Use Efficiency in Plants*, A. Bhattacharya, Hrsg. Academic Press, 2019, S. 1–50. doi: 10.1016/B978-0-12-816209-5.00001-5.
- [11] The University of Reading ECIFM, „Climate change and agriculture“. [Online]. Verfügbar unter: http://www.ecifm.rdg.ac.uk/climate_change.htm
- [12] B. Urych und A. Smoliński, „Kinetics of Sewage Sludge Pyrolysis and Air Gasification of Its Chars“, *Energy Fuels*, Bd. 30, Nr. 6, S. 4869–4878, Juni 2016, doi: 10.1021/acs.energyfuels.6b00332.
- [13] „National Center for Biotechnology Information. PubChem Compound Summary for CID 1061, Phosphate“, *national library of medicine, pubchem*, 27. Juni 2021. <https://pubchem.ncbi.nlm.nih.gov/compound/Phosphate>.
- [14] J. Elser und E. Bennett, „A broken biogeochemical cycle“, *Nature*, Bd. 478, Nr. 7367, S. 29–31, Okt. 2011, doi: 10.1038/478029a.
- [15] D. B. Beegle, „Managing Phosphorus for Crop Production“, *Penn State Extension*, 2002, [Online]. Verfügbar unter: <file:///C:/Users/user/Downloads/managing-phosphorus-for-crop-production.pdf>
- [16] T. K. Hannl, H. Sefidari, M. Kuba, N. Skoglund, und M. Öhman, „Thermochemical equilibrium study of ash transformation during combustion and gasification of sewage sludge mixtures with agricultural residues with focus on the phosphorus speciation“, *Biomass Convers. Biorefinery*, Bd. 11, Nr. 1, S. 57–68, Feb. 2021, doi: 10.1007/s13399-020-00772-4.
- [17] J. Stemann, B. Peplinski, und C. Adam, „Thermochemical treatment of sewage sludge ash with sodium salt additives for phosphorus fertilizer production--Analysis of underlying chemical reactions“, *Waste Manag.*, Bd. 45, S. 385–390, Nov. 2015, doi: 10.1016/j.wasman.2015.07.029.

- [18] O. Holm, E. Thomé-Kozmiensky, P. Quicker, und S. Kopp-Assenmacher, Hrsg., *Verwertung von Klärschlamm. Band [1]*. Neuruppin: Thomé-Kozmiensky Verlag GmbH, 2018.
- [19] D. Steckenmesser, C. Vogel, C. Adam, und D. Steffens, „Effect of various types of thermochemical processing of sewage sludges on phosphorus speciation, solubility, and fertilization performance“, *Waste Manag.*, Bd. 62, S. 194–203, Apr. 2017, doi: 10.1016/j.wasman.2017.02.019.
- [20] H. Hofbauer, *Unterlagen zur Vorlesung der Wirbelschichttechnik 159.220*. 1995.
- [21] P. Kerdoncuff, „Modellierung und Bewertung von Prozessketten zur Herstellung von Biokraftstoffen der zweiten Generation“, 2008. doi: 10.5445/IR/1000009255.
- [22] Fakultät Maschinenwesen Institut für Energietechnik, „Auslegung von Wirbelschichtanlagen“, 4. November 2009. https://tu-dresden.de/ing/maschinenwesen/iet/ressourcen/dateien/kwt/lehre/stubi/Wirbelschichtanlage_n.pdf?lang=de
- [23] K. D. Vernon-Parry, „Scanning electron microscopy: an introduction“, *III-Vs Rev.*, Bd. 13, Nr. 4, S. 40–44, Juli 2000, doi: 10.1016/S0961-1290(00)80006-X.
- [24] J. H. Holgate und J. Webb, „MICROSCOPY | Light Microscopy and Histochemical Methods“, in *Encyclopedia of Food Sciences and Nutrition (Second Edition)*, B. Caballero, Hrsg. Oxford: Academic Press, 2003, S. 3917–3922. doi: 10.1016/B0-12-227055-X/00778-1.
- [25] F. García-Labiano, E. Hampartsoumian, und A. Williams, „Determination of sulfur release and its kinetics in rapid pyrolysis of coal“, *Fuel*, Bd. 74, Nr. 7, S. 1072–1079, Juli 1995, doi: 10.1016/0016-2361(95)00049-B.
- [26] M. B. Folgueras, R. M. Díaz, J. Xiberta, und I. Prieto, „Volatilisation of trace elements for coal–sewage sludge blends during their combustion☆“, *4th UK Meet. Coal Res. Its Appl.*, Bd. 82, Nr. 15, S. 1939–1948, Okt. 2003, doi: 10.1016/S0016-2361(03)00152-2.
- [27] G. Häggström, T. K. Hannl, A. Hedayati, M. Kuba, N. Skoglund, und M. Öhman, „Single Pellet Combustion of Sewage Sludge and Agricultural Residues with a Focus on Phosphorus“, *Energy Fuels*, Bd. 35, Nr. 12, S. 10009–10022, Juni 2021, doi: 10.1021/acs.energyfuels.1c00882.
- [28] T. Krogstad, T. A. Sogn, Å. Asdal, und A. Sæbø, „Influence of chemically and biologically stabilized sewage sludge on plant-available phosphorous in soil“, *Ecol. Eng.*, Bd. 25, Nr. 1, S. 51–60, Juli 2005, doi: 10.1016/j.ecoleng.2005.02.009.
- [29] M. Kalbasi und K. G. Karthikeyan, „Phosphorus Dynamics in Soils Receiving Chemically Treated Dairy Manure“, *J. Environ. Qual.*, Bd. 33, Nr. 6, S. 2296–2305, Nov. 2004, doi: 10.2134/jeq2004.2296.
- [30] X. Wei, U. Schnell, und K. R. G. Hein, „Behaviour of gaseous chlorine and alkali metals during biomass thermal utilisation“, *Fuel*, Bd. 84, Nr. 7, S. 841–848, Mai 2005, doi: 10.1016/j.fuel.2004.11.022.
- [31] D. Steckenmesser, C. Vogel, L. Böhm, B. Heyde, und C. Adam, „Fate of heavy metals and polycyclic aromatic hydrocarbons (PAH) in sewage sludge carbonisates and ashes – A risk assessment to a thermochemical phosphorus-recycling process“, *Waste Manag.*, Bd. 78, S. 576–587, Aug. 2018, doi: 10.1016/j.wasman.2018.06.027.

Appendix I

Temperature profiles

 fluidizing bed

 preheating

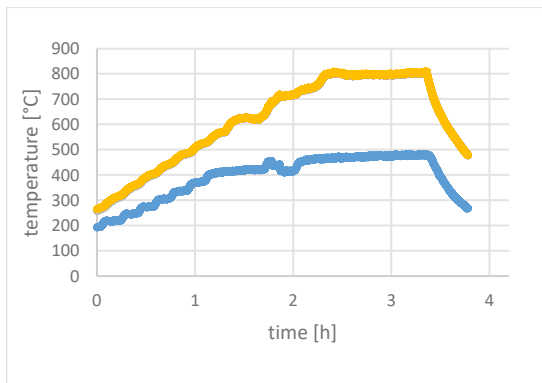


Figure 120: Temperature profile experiment 3

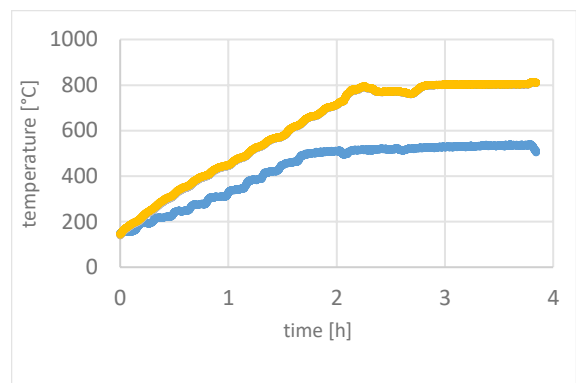


Figure 118: Temperature profile experiment 4

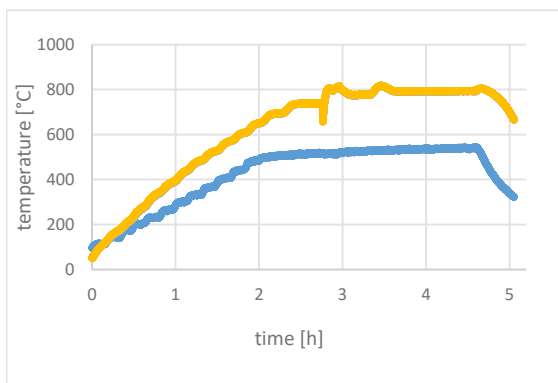


Figure 121: Temperature profile experiment 5

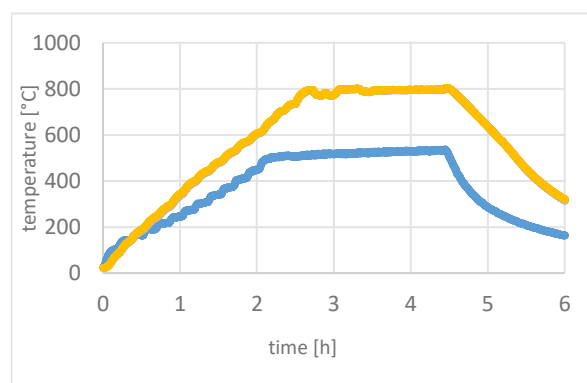


Figure 119: Temperature profile experiment 6

Appendix II

Gas composition profiles

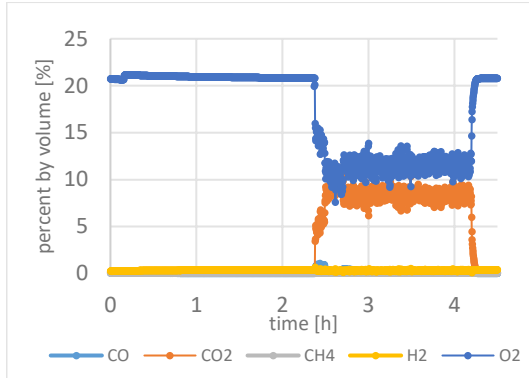


Figure 124: Gas composition experiment 3

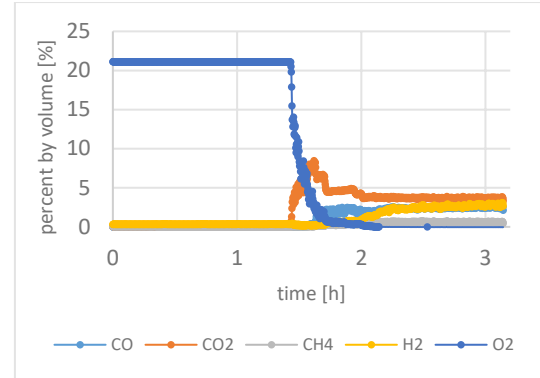


Figure 122: Gas composition experiment 4

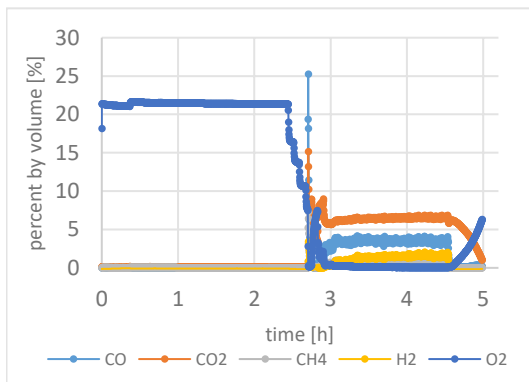


Figure 125: Gas composition experiment 5

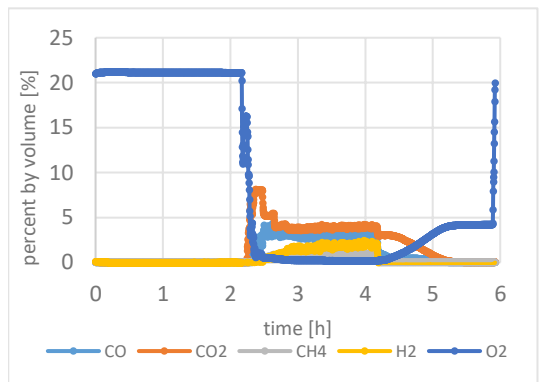


Figure 123: Gas composition experiment 6

Appendix III

Air-to-fuel-ratio λ over the duration of experiment 1

Time	Time difference [min]	Minutes	Hours	Conveyor frequency	m [g/min]	m [kg/h]	m [kg/h]*t	A_min,f[Nm ³ /h]	Air [NI/h]	Air [Nm ³ /h]	λ
12:21	3.00	0	0.0	20.1	4.73	0.2838	0.8514	1.06	5000	5	4.72
12:24	4	3.00	0.1	30	8.97	0.5382	2.1528	2.01	5000	5	2.49
12:28	5	7.00	0.1	30	8.97	0.5382	2.691	2.01	6000	6	2.99
12:33	4	12.00	0.2	25	6.85	0.411	1.644	1.53	6000	6	3.91
12:37	11	16.00	0.3	20.1	4.73	0.2837	3.1207	1.06	7000	7	6.61
12:48	2	27.00	0.5	20.1	8.97	0.5383	1.0766	2.01	7000	7	3.48
12:50	6	29.00	0.5	15.2	3.54	0.21265	1.2759	0.79	7000	7	8.82
12:56	16	35.00	0.6	10.1	2.36	0.14185	2.2696	0.53	7000	7	13.22
13:12	19	51.00	0.9	10.1	2.36	0.1416	2.6904	0.53	8000	8	15.14
13:31	10	70.00	1.2	10.1	2.36	0.1416	1.416	0.53	9000	9	17.03
13:41	10	80.00	1.3	10.1	2.36	0.1416	1.416	0.53	10000	10	18.92
13:51	10	90.00	1.5	10.1	2.36	0.1416	1.416	0.53	10000	10	18.92
14:01	10	100.00	1.7	10.1	2.36	0.1416	1.416	0.53	10000	10	18.92
14:11	16	110.00	1.8	10.1	2.36	0.1416	2.2656	0.53	10000	10	18.92
14:27	4	126.00	2.1	10.1	2.36	0.1416	0.5664	0.53	10000	10	18.92
14:31	5	130.00	2.2	10.1	2.36	0.1416	0.708	0.53	8000	8	15.14
14:36	5	135.00	2.3	14.9	3.54	0.2124	1.062	0.79	8000	8	10.09
14:41	3	140.00	2.3	20.1	4.73	0.2837	0.8511	1.06	8000	8	7.55
14:44	10	143.00	2.4	20.1	4.73	0.2838	2.838	1.06	6000	6	5.66
14:54	6	153.00	2.6	29.8	8.97	0.5382	3.2292	2.01	6000	6	2.99
15:00	10	159.00	2.7	40.2	12.21	0.7326	7.326	2.73	6000	6	2.19
15:10	11	169.00	2.8	40.2	12.21	0.7326	8.0586	2.73	5000	5	1.83
15:21	10	180.00	3.0	40.2	12.21	0.7326	7.326	2.73	5000	5	1.83
15:31	5	190.00	3.2	40.2	12.21	0.7326	3.663	2.73	5000	5	1.83
15:36		195.00	3.3								
					average		0.347	0.315	1.30	7.25	5.60

Air-to-fuel-ratio λ over the duration of experiment 2

Time	Time difference [min]	Minutes	Hours	Conveyor frequency	m [g/min]	m [kg/h]	m [kg/h]*t	A_min,f[N m ³ /h]	Air [NI/h]	Air [Nm ³ /h]	λ
11:13	10.00	0	20	5.35	0.321	3.21	1.55	4000	4	2.59	25.88
11:23	3	10.00	30	9.36	0.5616	1.6848	2.70	4000	4	1.48	4.44
11:26	3	13.00	30	9.36	0.5616	1.6848	2.70	5000	5	1.85	5.55
11:29	2	16.00	30	9.36	0.5616	1.1232	2.70	5000	5	1.85	3.70
11:31	10	18.00	30	9.36	0.5616	5.616	2.70	6000	6	2.22	22.19
11:41	2	28.00	30	9.36	0.5616	1.1232	2.70	6000	6	2.22	4.44
11:43	10	30.00	30	9.36	0.5616	5.616	2.70	6000	6	2.22	22.19
11:53	9	40.00	30	9.36	0.5616	5.0544	2.70	6000	6	2.22	19.97
12:04	1	49.00	30	9.36	0.5616	0.5616	2.70	6000	6	2.22	2.22
12:05	9	50.00	30	9.36	0.5616	5.0544	2.70	6000	6	2.22	19.97
12:14	10	59.00	30	9.36	0.5616	5.616	2.70	6000	6	2.22	22.19
12:24	10	69.00	30	9.36	0.5616	5.616	2.70	6000	6	2.22	22.19
12:34	13	79.00	30	9.36	0.5616	7.3008	2.70	6000	6	2.22	28.84
12:47	10	92.00	30	9.36	0.5616	5.616	2.70	6000	6	2.22	22.19

12:57	10	102.00	30	9.36	0.5616	5.616	2.70	6000	6	2.22	22.19
13:07	10	112.00	30	9.36	0.5616	5.616	2.70	6000	6	2.22	22.19
13:17	10	122.00	30	9.36	0.5616	5.616	2.70	6000	6	2.22	22.19
13:27	4	132.00	30	9.36	0.5616	2.2464	2.70	6000	6	2.22	8.87
13:31		136.00				0					
				average	0.5482	0.5439	2.64		5.667	2.15	2.22

Air-to-fuel-ratio λ over the duration of experiment 3

Time	Time difference [min]	Minutes	Conveyor frequency	m [g/min]	m [kg/h]	m [kg/h]*t	A _{min,f} [Nm ³ /h]	Air [NI/h]	Air [Nm ³ /h]	λ
10:25	20.00	0	20	4.23	0.254	5.08	1.10	4000	4	3.63
10:45	4	20.00	30	8.30	0.498	1.992	2.16	4000	4	1.85
10:49	5	24.00	30	8.30	0.498	2.49	2.16	5000	5	2.32
10:54	4	29.00	40	11.14	0.6685	2.674	2.90	5000	5	1.73
10:58	10	33.00	40	11.14	0.6685	6.685	2.90	6000	6	2.07
11:08	10	43.00	40	11.14	0.6685	6.685	2.90	6000	6	2.07
11:18	10	53.00	40	11.14	0.6685	6.685	2.90	6000	6	2.07
11:28	10	63.00	40	11.14	0.6685	6.685	2.90	6000	6	2.07
11:38	10	73.00	40	11.14	0.6685	6.685	2.90	6000	6	2.07
11:48	10	83.00	40	11.14	0.6685	6.685	2.90	6000	6	2.07
11:58	10	93.00	40	11.14	0.6685	6.685	2.90	6000	6	2.07
12:08	10	103.00	40	11.14	0.6685	6.685	2.90	6000	6	2.07
12:18	10	113.00	40	11.14	0.6685	6.685	2.90	6000	6	2.07
12:28		123.00	40	11.14	0.6685	0	2.90	6000	6	2.07
				average	0.6145	0.5886	2.66		5.571	2.09

Air-to-fuel-ratio λ over the duration of experiment 4

Time	Time difference	Minutes	Conveyor frequency [Hz]	m [g/min]	m [kg/h]	m [kg/h]*t	A _{min,f} [Nm ³ /h]	Air [NI/h]	N ₂ [NI/h]	Total fluidization [NI/h]	Air [Nm ³ /h]	λ
13:18	3.00	0	20	4.44	0.2665	0.7995	0.99	3500	750	4250	3.5	3.52
13:21	2	3.00	20	4.44	0.2665	0.533	0.99	3000	1000	4000	3	3.02
13:23	3	5.00	20	4.44	0.2665	0.7995	0.99	2500	1500	4000	2.5	2.51
13:25	4	8.00	30	8.76	0.52575	2.103	1.96	2500	1500	4000	2.5	1.27
13:29	4	12.00	30	8.76	0.52575	2.103	1.96	2000	2000	4000	2	1.02
13:33	11	16.00	30	8.76	0.52575	5.78325	1.96	1500	2500	4000	1.5	0.76
13:44	5	27.00	35	10.94	0.65625	3.28125	2.45	1500	2500	4000	1.5	0.61
13:49	1	32.00	35	14.29	0.85725	0.85725	3.20	1500	2500	4000	1.5	0.47
13:50	3	33.00	40	13.11	0.78675	2.36025	2.94	1500	3000	4500	1.5	0.51
13:53	1	36.00	40	13.11	0.78675	0.78675	2.94	1000	3000	4000	1	0.34
13:54	8	37.00	40	13.11	0.78675	6.294	2.94	1000	3000	4000	1	0.34
14:02	12	45.00	40	13.11	0.78675	9.441	2.94	1000	3000	4000	1	0.34
14:14	8	57.00	40	13.11	0.78675	6.294	2.94	1000	3000	4000	1	0.34
14:22	7	65.00	40	13.11	0.78675	5.50725	2.94	1000	3000	4000	1	0.34
14:29	20	72.00	40	13.11	0.78675	15.735	2.94	1000	3000	4000	1	0.34
14:49	11	92.00	40	13.11	0.78675	8.65425	2.94	1000	3000	4000	1	0.34
15:00		103.00	40	13.11	0.78675	0	2.94	1000	3000	4000	1	0.34
				average	0.6454	0.6925	2.41				1.618	0.67

Air-to-fuel-ratio λ over the duration of experiment 5

Time	Time difference	Minutes	Conveyor frequency [Hz]	m'[g/min]	m'[kg/h]	m'[kg/h]*t	A_min,f [Nm ³ /h]	Air [NI/h]	N ₂ [NI/h]	Total fluidization [NI/h]	Air [Nm ³ /h]	λ
10:37	5.00	0	30	9.36	0.5616	2.808	2.70	3000	1000	4000	3	1.11
10:42	5	5.00	30	9.36	0.5616	2.808	2.70	2500	1500	4000	2.5	0.92
10:47	5	10.00	30	9.36	0.5616	2.808	2.70	2500	2000	4500	2.5	0.92
10:52	5	15.00	30	9.36	0.5616	2.808	2.70	1500	2500	4000	1.5	0.55
10:57	5	20.00	30	9.36	0.5616	2.808	2.70	2000	2000	4000	2	0.74
11:02	5	25.00	30	9.36	0.5616	2.808	2.70	2000	2000	4000	2	0.74
11:07	6	30.00	30	9.36	0.5616	3.3696	2.70	1500	2500	4000	1.5	0.55
11:13	12	36.00	40	13.03	0.7818	9.3816	3.76	1500	2500	4000	1.5	0.40
11:25	2	48.00	40	13.03	0.7818	1.5636	3.76	1500	2500	4000	1.5	0.40
11:27	7	50.00	40	13.03	0.7818	5.4726	3.76	1500	2500	4000	1.5	0.40
11:34	5	57.00	40	13.03	0.7818	3.909	3.76	1500	2500	4000	1.5	0.40
11:49	2	62.00	40	13.03	0.7818	1.5636	3.76	1500	2500	4000	1.5	0.40
12:01	30	64.00	40	13.03	0.7818	23.454	3.76	1500	2500	4000	1.5	0.40
12:31	14	94.00	40	13.03	0.7818	10.9452	3.76	1500	2500	4000	1.5	0.40
12:45		108.00	40	13.03	0.7818		3.76	1500	2500	4000	1.5	0.40
				average	0.6790	0.7084	3.27				1.800	0.55

Air-to-fuel-ratio λ over the duration of experiment 6

Time	Time difference	Minutes	Conveyor frequency [Hz]	m'[g/min]	m'[kg/h]	m'[kg/h]*t	A_min,f [Nm ³ /h]	Air [NI/h]	N ₂ [NI/h]	Total fluidization [NI/h]	Air [Nm ³ /h]	λ
10:48	4	0	30	8.30	0.498	1.992	2.16	3000	1000	4000	3	1.39
10:52	2.00	4.00	30	8.30	0.498	0.996	2.16	2500	1500	4000	2.5	1.16
10:54	2	6.00	30	8.30	0.498	0.996	2.16	2000	2000	4000	2	0.93
10:56	4	8.00	40	11.14	0.6685	2.674	2.90	2000	2000	4000	2	0.69
11:00	5	12.00	40	11.14	0.6685	3.3425	2.90	2000	2000	4000	2	0.69
11:05	5	17.00	40	11.14	0.6685	3.3425	2.90	1500	2500	4000	1.5	0.52
11:10	5	22.00	40	11.14	0.6685	3.3425	2.90	1500	2500	4000	1.5	0.52
11:15	5	27.00	40	11.14	0.6685	3.3425	2.90	1000	3000	4000	1	0.35
11:20	5	32.00	40	11.14	0.6685	3.3425	2.90	1000	3000	4000	1	0.35
11:25	5	37.00	40	11.14	0.6685	3.3425	2.90	800	3200	4000	0.8	0.28
11:30	10	42.00	40	11.14	0.6685	6.685	2.90	800	3200	4000	0.8	0.28
11:40	8	52.00	40	11.14	0.6685	5.348	2.90	800	3200	4000	0.8	0.28
11:48	7	60.00	40	11.14	0.6685	4.6795	2.90	800	3200	4000	0.8	0.28
12:35	12	67.00	40	11.14	0.6685	8.022	2.90	800	3200	4000	0.8	0.28
12:47		79.00										
				average	0.6320	0.6512	2.74				1.464	0.53